FEDERAL UNIVERSITY OF SÃO CARLOS
CENTER OF EXACT SCIENCES AND TECHNOLOGY
GRADUATE PROGRAM IN MATERIALS SCIENCE AND ENGINEERING

REFILL FRICTION STIR SPOT WELDING OF AA6016-T4 ALUMINUM ALLOY: STUDY OF NEW LOAD-CONTROLLED PROCESS

Jéssica Bruna Ponsoni

São Carlos-SP
2020

FEDERAL UNIVERSITY OF SÃO CARLOS
CENTER OF EXACT SCIENCES AND TECHNOLOGY
GRADUATE PROGRAM IN MATERIALS SCIENCE AND ENGINEERING

REFILL FRICTION STIR SPOT WELDING OF AA6016-T4 ALUMINUM ALLOY: STUDY OF NEW LOAD-CONTROLLED PROCESS

Jéssica Bruna Ponsoni

Dissertation presented to Graduate Program in Materials Science and Engineering as partial requirement to obtain the MASTER DEGREE IN MATERIALS SCIENCE AND ENGINEERING

Supervisor: Prof. Dr. Nelson Guedes de Alcântara
Co-supervisor: Prof. Dr. Guilherme Zepon
Grant Agency: CNPq – Process no. 130500/2019-4

São Carlos-SP
2020

DEDICATION

To my parents, Jair and Elizabete, and my sister Karla, with all love.

VITAE

Bachelor degree in Materials Engineering (2018) from UFSCar

UNIVERSIDADE FEDERAL DE SÃO CARLOS

Centro de Ciências Exatas e de Tecnologia
Programa de Pós-Graduação em Ciência e Engenharia de Materiais

---

Folha de Aprovação

Defesa de Dissertação de Mestrado da candidata Jéssica Bruna Ponsoni, realizada em 29/06/2020.

Comissão Julgadora:

Prof. Dr. Nelson Guedes de Alcântara (UFSCar)

Prof. Dr. Piter Gargarella (UFSCar)

Prof. Dr. Athos Henrique Plâine (UDESC)

O presente trabalho foi realizado com apoio da Coordenação de Aperfeiçoamento de Pessoal de Nível Superior - Brasil (CAPES) - Código de Financiamento 001.

O Relatório de Defesa assinado pelos membros da Comissão Julgadora encontra-se arquivado junto ao Programa de Pós-Graduação em Ciência e Engenharia de Materiais.

ACKNOWLEDGMENTS

I thank God for my life, health, blessings, and light throughout this journey.

To Professor Nelson Guedes de Alcântara, for all the opportunities, suggestions, discussions, guidance, and constant encouragement.

To Professor Guilherme Zepon, for all the suggestions, discussions, guidance, and countless contributions that optimized this work.

To my supervisors at HZG, Dr. Jorge dos Santos and Dr. Uceu Suhuddin for the guidance and support during the work developed in Germany.

I thank my beloved family, especially my parents and my sister, my greatest examples. Thank you for your love, for supporting me unconditionally in every moment of my life and for your tireless prayers.

To Bruno, for all the love, attention, patience, and encouragement. Your lovely words made all the difference during this stage.

To all my colleagues at PPGCEM and HZG for making this trajectory lighter and unforgettable.

To my friends, for their countless conversations, laughs, and words of comfort and tenderness.

To PPGCEM, DEMa, CCDM, and HZG, for the excellent infrastructure and technical members, who contributed to the development of this work, and for the excellent reception and wonderful moments shared.

To the Conselho Nacional de Desenvolvimento Científico e Tecnológico-CNPq - Brasil (CNPq) - Process no. 130500 / 2019-4. This study was financed in part by the Coordenação de Aperfeiçoamento de Pessoal de Nível Superior - Brasil (CAPES) - Finance Code 001

ABSTRACT

Aiming at structural weight reduction and energy efficiency, aluminum alloys have been considered as potential materials for automobile manufacturing. The development of technologies able to join aluminum alloys more effectively contributes to increasing their application in this transport industry sector. AlMgSi alloys have a highlight in selecting light materials for vehicle assembly due to its properties such as low density, high strength-to-weight ratio, and good corrosion resistance. Refill friction stir spot welding (Refill FSSW) is a solid-state joining technology suitable for joining lightweight materials. This process consists of a few steps performed within seconds, with low energy consumption, and without consumables addition. Thus, it is being considered as the most promising technology to replace traditional joining techniques as resistance spot welding (RSW) and self-piercing riveting (SPR) processes. This work presents the innovative Refill FSSW robotic process controlled by load. This new process was used to produce welds of AA6016-T4 sheets. Results obtained through the conventional position-controlled Refill FSSW process was used for comparing and validating the effectiveness of the new welding control system. Process parameters optimization was carried out in order to obtain a process condition that maximizes the mechanical performance (lap shear strength) of the joint performed using the load-controlled Refill FSSW. Statistical methods, such as Box-Behnken design, were applied to optimize the process parameters. Microstructure analyses were performed to characterize the features of the joint. Hardness and thermal characterization helped to understand different weld regions, the mechanical properties, and the fracture behavior of the welds. Furthermore, the dynamic mechanical property was analyzed by fatigue tests for the condition of the highest lap shear strength and the L-N curve was drawn. The results indicated a satisfactory static and dynamic performance of the welds. Finally, failure mechanisms of static and dynamic tests seemed to be strongly related to microstructural regions.

Keywords: Refill Friction Stir Spot Welding; Refill FSSW; Load control; AA6016-T4; Box-Behnken Design; Lap Shear Strength; Fatigue behavior.

RESUMO

SOLDAGEM POR FRICÇÃO POR PONTO DA LIGA AA6016-T4: ESTUDO DO PROCESSO CONTROLADO POR FORÇA

Visando redução do peso estrutural e eficiência energética, as ligas de alumínio têm sido consideradas como materiais potenciais para a fabricação de automóveis. O desenvolvimento de tecnologias capazes de unir ligas de alumínio de modo eficaz contribui para o aumento da aplicação das mesmas no setor automotivo. Ligas do sistema AlMgSi se destacam na seleção de ligas leves devido suas propriedades como baixa densidade, elevada relação resistência-peso e boa resistência a corrosão. A soldagem por fricção por ponto (Refill FSSW) é uma tecnologia de união no estado sólido adequada para a soldagem de ligas leves. Esse processo é realizado em poucas etapas e curto tempo, com baixo consumo de energia e sem a utilização de consumíveis, sendo considerada uma tecnologia promissora como alternativa para técnicas tradicionais, como soldagem por ponto por resistência e rebitagem. Esse trabalho apresenta, como inovação, a robotização e o controle de soldagem por força do processo Refill FSSW, na liga AA6016-T4. Os resultados obtidos através do processo convencional foram utilizados para comparar e validar a eficácia do novo sistema de soldagem. A otimização dos parâmetros de processo foi realizada visando a obtenção de uma condição que maximizasse resistência ao cisalhamento das juntas obtidas pelo processo com controle de força. Método estatísticos como o Box-Behnken design, foram empregados no estudo de otimização dos parâmetros de processo. Análises microestruturais foram realizadas para identificar as características da junta. A dureza e a caracterização térmica ajudaram a entender as diferentes regiões, as propriedades mecânicas e o mecanismo de fratura das soldas. Além disso, foram realizados ensaios de fadiga para a condição de maior resistência ao cisalhamento e a curva L-N foi traçada. Os resultados indicaram um satisfatório desempenho estático e dinâmico das soldas. Finalmente, os mecanismos de falha, dos testes estáticos e dinâmicos, se mostraram fortemente relacionados às regiões microestruturais.

Palavras-chave: Soldagem por fricção por ponto; Refill FSSW; Controle de força; AA6016-T4; Box-Behnken Design; Resistência ao cisalhamento; Fadiga.

TABLE OF CONTENTS

APPROVAL SHEET i
ACKNOWLEDGMENTS iii
ABSTRACT v
RESUMO vii
TABLE OF CONTENTS ix
LIST OF TABLES xiii
LIST OF FIGURES xv
SYMBOLS AND ABBREVIATIONS xxi
1 INTRODUCTION AND MOTIVATION 1
2 OBJECTIVES 3
3 LITERATURE REVIEW 5
  3.1 ALUMINUM ALLOYS 5
    3.1.1 Aluminum Alloys for Automotive Applications 5
    3.1.2 AlMgSi Aluminum Alloys 8
    3.1.3 AlMgSi Aluminum Alloys Weldability 13
  3.2 REFILL FRICTION STIR SPOT WELDING 16
    3.2.1 Comparison Between by Load- and Position-controlled Refill FSSW process 19
    3.2.2 Microstructures Features of Refill FSSW Joints 21
    3.2.3 Mechanical Properties of Refill FSSW Joints 23
4 MATERIALS AND METHODS 33
  4.1 MATERIAL 33
  4.2 WELDING PROCESS 33
    4.2.1 Load-controlled process 33
    4.2.2 Position-controlled process 34
  4.3 PARAMETERS OPTIMIZATION FOR LOAD-CONTROLLED PROCESS 35

4.3.1 Processing Window 35

4.3.2 Design of Experiments 36

4.4 LAP SHEAR TESTS 37

4.5 CHARACTERIZATION OF THE OPTIMIZED WELD 38

4.5.1 Structural Characterization 38

4.5.1.1 Macro and Microstructural Analyzes 38
4.5.1.1.1 Stop Action Procedure 39

4.5.1.2 Microhardness Vickers 40
4.5.1.3 Temperature Measurements 40
4.5.1.3.1 Thermal Analysis 41

4.5.1.4 Bake Hardening Treatment 42
4.5.2 Dynamic Mechanical Properties 42

4.5.2.1 Fatigue Test 42
4.5.2.1.1 Weibull Distribution and L-N Curves 42

4.5.2.1.2 Fracture Analysis 44

5 RESULTS AND DISCUSSIONS 45
5.1 PARAMETER OPTIMIZATION FOR LOAD-CONTROLLED PROCESS 45

5.2 STRUCTURAL CHARACTERIZATION 51

5.2.1 Macro and Microstructural Analysis 51

5.2.2 Stop Action Procedure 56

5.3 Static Mechanical Properties 58

5.3.1 Microhardness Vickers 58

5.3.2 Fracture mode analysis 62

5.4 Thermal analysis 63

5.4.1 Temperature Measurements 63

5.4.2 Differential Scanning Calorimetry 65

5.4.3 Bake hardening treatment 68

5.5 Dynamic Mechanical properties ... 71

5.5.1 Fatigue Results ... 71

5.5.2 Weibull Distribution and L-N Curves ... 71

5.5.3 Fracture Analysis ... 76

6 CONCLUSIONS ... 83

7 SUGGESTIONS FOR FUTURE WORKS ... 85

8 REFERENCES ... 87

APPENDIX A ... 95

LIST OF TABLES

Table 3.1 – Alloying elements and AA designation of wrought aluminum and its alloys [13]. 8
Table 3.2 – Mechanical properties (yield strength (σ_y), tensile strength (σ_m) and elongation) of AA6016 according to two different heat treatments [22]. 12
Table 4.1 – Chemical composition (mass %) of AA6016 [62]. 33
Table 4.2 – Mechanical properties of AA6016-T4 [22]. 33
Table 4.3 – Process parameters of the position-controlled process. 35
Table 4.4 – Initial processing window. 36
Table 4.5 – Process parameters and values of variation levels for the BBD. ... 37
Table 4.6 – Process parameters combination according to BBD for process optimization. 37
Table 5.1 – Process parameters limits after additional tests. 45
Table 5.2 – Analysis of variance (ANOVA) for the lap shear strength model. .. 48
Table 5.3 – Welding parameters and lap shear strength of the load- and position-controlled process. 49
Table 5.4 – Load levels and results of fatigue tests for Refill FSSW specimens. 71
Table 5.5 – Weibull parameters and mean life for each load level. 73

LIST OF FIGURES

Figure 3.1 – North American net aluminum content in light vehicles since 1996 and forecasts from 2020 to 2028 (1 lb. = 0.453 kg) [10]. 6
Figure 3.2 – (a) Audi A8 space frame in aluminum: vacuum structural aluminum (red), extrusion profiles aluminum (light blue), sheet aluminum (green) and high-strength steel (dark blue) and (b) Mass percentage of metallic materials in Range Rover L405 structure: aluminum – 95 % (37% Al 6XXX and 37% Al 5XXX) and high-strength steels – 5 % [11]. 7
Figure 3.3 – Heating DSC curves at 0.1 K/s for AA6016 alloy for T4 (black line) and T6 (green line) initial condition [15]. 10
Figure 3.4 – True strain-stress curves for AA6014 alloy in different heat treatments: T4 - solution heat-treated and naturally aged, T6 - solution heat-treated and artificially aged, and T7 - solution heat-treated and stabilized (overaged) [18]. 11
Figure 3.5 – Strengthening mechanisms and their contribution to overall strength for an aluminum alloy [21]. 12
Figure 3.6 – Comparison of the costs associated with an installation of a plant with an annual production of 35,000 cars during ten years for SPR, RSW and FSSW techniques [4]. 15
Figure 3.7 – Superficial and cross-section features of the resulting welds performed with (a) FSSW and (b) Refill FSSW [6]. 17
Figure 3.8 – Schematic illustration of the toll components: probe, sleeve and clamping ring, and the attached tool in a concentric way. 18
.... 19
Figure 3.9 - Schematic illustration of SP variant of Refill FSSW process: Stage 1 – Pre-heating and specimen fixation; Stage 2 – Sleeve plunge and probe retraction; Stage 3 – Return of the tool to the starting position, and Stage 4 – Tool removal [Adapted from 38]. 19
Figure 3.10 – Schematic illustration of SP variant of Refill FSSW process controlled by the load with an additional stage (stage 3) [38]. 20
Figure 3.11 – Typical microstructural regions along the cross section of an AA 2198 specimen performed with Refill FSSW process: stir zone (SZ),

thermomechanically affected zone (TMAZ), heat affected zone (HAZ) and base material (BM) [adapted from 41]. 21
Figure 3.12 – Hook (A) and oxide line remnant (B) of a cross section of a spot weld performed by Refill FSSW process. 23
Figure 3.13 – Microhardness profile ($HV_{0.3}$) through the mid-thickness of the upper and lower sheet of the Refill FSSW joint of 7050-T76 aluminum alloy [45]. 24
Figure 3.14 – Microhardness profile ($HV_{0.1}$) through the RSW joint of 6082-T6 aluminum alloy performed with three different weld currents: 23.5, 26.4 and 28.7 kA (increasing weld current increases the nugget size or weld spot, also the width of the HAZ). The grey bar illustrates the hardness of the base material. [47]. 25
Figure 3.15 – Lap shear strength values of Refill FSSW joints of aluminum alloys with different sheets thicknesses (identified by colors and their values above the column) and the minimum lap shear strength in accordance with the specification of the American Welding Society – AWS D17.2/D17.2M:2013 Specification for Resistance Welding for Aerospace Applications, for three different sheet thicknesses (horizontal lines) [34, 36, 41, 42, 45, 48, 50-53]. ... 27
Figure 3.16 – The S–N curve obtained for the average fatigue life of AA7050-T76 similar Refill FSSW joints [45]. 29
Figure 3.17 – Comparison of fatigue strength between RSW and FSSW of AlMgSi similar joints characterized in terms of a maximum load [55]. 31
Figure 4.1 – (a) KHI Robot and (b) Tool components: probe, sleeve, and clamping ring with external diameters of 15 mm, 9 mm, and 5 mm, respectively. (c) The attached tool with all three concentric tools... 34
Figure 4.2 – (a) Harms & Wende RPS 100 machine and (b) Tool components: probe, sleeve, and clamping ring. (c) The attached tool with all three concentric tools.. 35
Figure 4.3 – Schematic illustration of the welded specimen for lap shear test and its dimensions in millimeters.. 38
Figure 4.4 – Schematic illustration of the cut region of a welded sample for macro and microstructural analyses (dimensions in millimeters)...................... 39

Figure 4.5 – Schematic illustration of the interruption position during the sleeve penetration in the welding process. 40
Figure 4.6 – Schematic illustration of the thermocouples approach (dimensions in millimeters). 41
Figure 5.1 – Response surfaces (a) PDxRF, (b) RSxPD, (c) RSxRF and contour plots, (d) PDxRF, (e) RSxPD, (f) RSxRF from the lap shear tests obtained by the Box Behnken design. 46
Figure 5.2 – Response surfaces (a) PDxRF, (b) RSxPD, (c) RSxRF and contour plots, (d) PDxRF, (e) RSxPD, (f) RSxRF from the lap shear tests obtained after additional tests. 47
Figure 5.3 – LSS *versus* displacement graph of lap shear test of a sample performed through the load-controlled Refill FSSW process. 49
Figure 5.4 – Welding force graph of the load-controlled Refill FSSW process during the optimized-parameter performance, with a load of 10 kN during the sleeve plunging stage and 9 kN in the sleeve retracting stage, and a sleeve plunge depth of 1.6 mm. 50
Figure 5.5 – Macrograph and details by optical microscopy of the cross-section of the welded joint performed by the load-controlled process. (A) Macrograph showing the different zones and features such as hook feature and bonding ligament; (B) microstructure of SZ; (C) microstructure of TMAZ and HAZ; (D) hook feature; (E) grain structure in the central top of SZ and (F) base material. 52
Figure 5.6 – Macrograph and details by optical microscopy of the cross-section of the welded joint performed by the position-controlled process. (A) Macrograph showing the different zones and features such as hook and bonding ligament; (B) detail of the hook and (C) detail of the grain structure in the center top of the SZ. 53
Figure 5.7 – Macrograph by optical microscopy of the cross-section of the defect-free welded joint performed by the load-controlled process. 54
Figure 5.8 – Backscattered electron mode (BSE) SEM images of the non-etched cross-section of the welded joint performed by the load-controlled

process using the optimized process parameters. (a) Detail of the center discontinuity and (b) Detail of the flat shape of the hook tip. 55
Figure 5.9 – Macrograph by optical microscopy of the cross-section of the samples obtained through the stop action procedure during the second stage of the (A) load-controlled; (B) position-controlled welding process with a sleeve plunge of 1.6 mm; (C) detail of the flat shape of the hook tip and (D) detail of hook tip points up. 57
Figure 5.10 – Microhardness profile measured in the mid-thickness of the upper (black square) and bottom sheet (gray circle) of the cross-section of load-controlled Refill FSSW joint. 59
Figure 5.11 – Hardness map measured in the entire cross-section of the load-controlled Refill FSSW joint. 60
Figure 5.12 – Microhardness profile measured in the mid-thickness of the upper (black square) and bottom sheet (gray circle) of the cross-section of position-controlled Refill FSSW joint. 61
Figure 5.13 - Macrograph by optical microscopy of the cross-section of a sample obtained by interrupting the shear test. The white arrows indicate the direction of the load application. 62
Figure 5.14 – Microstructure by optical microscopy of the cross-section of the welded joint performed by the load-controlled process (a) before and (b) after the lap shear test, illustrating the pull-out failure. 63
Figure 5.15 – Temperature measurement indicating thermal behavior in the SZ, and HAZ during the load-controlled Refill FSSW process. 64
Figure 5.16 – Al-Mg_2Si diagram phase [72]. 65
Figure 5.17 – DSC curves of the base material (AA6016-T4) – red line, and of base material after solution heat treatment and water quenching - black line. . 66
Figure 5.18 – DSC curves of (a) base material (AA6016-T4) – red line and SZ - blue line, and of (b) base material (AA6016-T4) – red line and HAZ - green line. 67
Figure 5.19 – (a) Microhardness profile measured in the mid-thickness of the upper (black square) and bottom sheet (gray circle) of the cross-section of load-controlled Refill FSSW joint after bake hardening treatment and comparison of

the hardness profile of the (a) top plate in bake hardened (black square) and as-welded (blue square) condition and of the (c) bottom plate in bake hardened (gray circle) and as-welded (blue circle) condition... 69

Figure 5.20 – LSS average of samples performed through the load-controlled Refill FSSW process tested in as-welded and bake hardened conditions. 70

Figure 5.21 – Weibull plots for the tested different load levels. 72

Figure 5.22 – L–N curve of Refill FSSW of AA6016-T4. 73

Figure 5.23 – Effect of the mean fatigue life on the coefficients of variation..... 74

Figure 5.24 – L–N curves for different reliability levels. 75

Figure 5.25 – L-N curves of samples performed with load- and position-controlled system. 76

Figure 5.26 – Failure modes identified during fatigue tests at the different loads level percentages: (a) pull-out at 50%, (b) pull-out at 25%, (c) eyebrow at 15%, (d) eyebrow at 12.5%, and no fracture at 10%. 77

Figure 5.27 – Macrograph of the (a) pull-out and (b) eyebrow fatigue fracture surfaces indicating cracks nucleation site (yellow arrows) and crack propagation directions (red arrows). 78

Figure 5.28 – SEM fatigue fracture surfaces: (a) presence of steps at the interface between the plates (fatigue crack nucleation points – yellow arrows and direction of crack propagation – red arrows) and (b) transition region between the weld periphery and the plate width.. 79

Figure 5.29 – Fracture surface investigation of the pull-out failure mode for low-cycle loading condition: (A) dimples and (B) cleavage and dimples indicating ductile fracture in the final fracture area; (C) fatigue striations in the center area; (D) dimples, (E) cleavage and (F) dimples in the deformed region. 80

Figure 5.30 – Fracture surface investigation of the eyebrow failure mode for high-cycle loading condition: (A) and (B) dimples indicating ductile fracture in the final fracture area; (C) fatigue striations in the center area; (D) and (E) fatigue striations in the transition region between the weld periphery and the plate width, and (F) fatigue striations in the base material. 81

SYMBOLS AND ABBREVIATIONS

AA	Aluminum Association
AWS	American Welding Society
ANOVA	Analysis of Variance
BBD	Box Behnken Design
CCDM	Center for Characterization and Development of Materials
CV	Coefficient of Variation
DEMa	Department of Materials Engineering
DOE	Design of Experiments
DSC	Differential Scanning Calorimetry
E	Elasticity Modulus
EDS	Energy Dispersive X-Ray Spectroscopy
F	Axial Force
FSSW	Friction Stir Spot Welding
FSpW	Friction Spot Welding
FSW	Friction Stir Welding
GP	Guinier Preston
HAZ	Heat-Affected Zone
HZG	Helmholtz-Zentrum Geesthacht
$HV_{0.2}$	Microhardness Vickers
KHI	Kawasaki Heavy Industries
LCE	Structural Characterization Laboratory
LSS	Lap Shear Strength
MTTF	Mean Time to Failure
OM	Optical Microscopy
PD	Penetration Depth
PDF	Probability Density Function
PF	Plunge Force
PP	Probe Plunge
PPGCEM	Programa de Pós-Graduação em Ciência e Engenharia de Materiais
PR	Plunge Rate

RF	Retracting Force
Refill FSSW	Refill Friction Stir Spot Welding
RS	Rotational Speed
RSM	Response Surface Methodology
RSW	Resistance Spot Welding
SD	Standard Deviation
SEM	Scanning Electron Microscopy
SP	Sleeve Plunge
SPR	Self-Piercing Riveting
SSSS	Supersaturated Solid Solution
SZ	Stir Zone
TEM	Transmission Electron Microscopy
TMAZ	Thermomechanically-Affected Zone
TWI	The Welding Institute
WMP	Solid State Joining Processes Department
WT	Welding Time
σ_m	Tensile Strength
σ_y	Yield Strength

1 INTRODUCTION AND MOTIVATION

In recent decades, the automotive industry has been facing important developments regarding the processes, components, and materials aiming at higher efficiency and safety. The metallic materials compose a large part of the automobile components and are present in greater quantities in comparison with the other classes of materials. Consequently, these materials are the most responsible for the car weight.

Since the beginning of the 21st century, this sector has also faced challenges to meet environmental and economic requirements such as greater energy efficiency, performance, and reduction of polluting gases emissions. The fuel consumption reduction is considered the main way to reach these requirements, being directly related to car weight reduction. In this way, aluminum alloys have been considered as potential material for automobile manufacturing, replacing heavier materials, as steel, due to its unique combination of properties such as low density, good corrosion resistance, high recyclability, and a good relation of mechanical strength and formability [1, 2].

However, the large-scale use of aluminum alloys implies a high final cost of the product due to numerous challenges, including the adaptation of the manufacturing methods used to ferrous alloys to aluminum alloys. A major challenge is the joining processes of the constituent components of the car during the assembly stage. Conventional join processes employed in aluminum alloys in the automotive industry are resistance spot welding (RSW) and self-piercing riveting (SPR). RSW process involves the melting of the material which, due to some inherent properties of aluminum, as high thermal and electrical conductivity, low melting point, the high solubility of hydrogen in the liquid state, oxide layer formation and high coefficient of thermal expansion, results in defects such as hot tears, solidification cracks, porosity and warpage that impair the mechanical properties of the joint. In addition, the high thermal and electrical conductivity, and the high melting point of the oxide layer require high energy consumption for melting the material, making the process energetically costly. SPR process produces the joining of sheets through the mechanical anchoring provided by a self-drilling steel rivet. Thus, this is a process of mechanical join that does not involve the melting and solidification of the material, but its main limitation is linked to the high cost of the rivets that makes the production in a large scale economically unviable, besides the increase of weight and the greater susceptibility to corrosion [2–4].

Friction welding processes provide a solid-state join of materials and are recent technologies that emerge as potential substitutes for conventional welding techniques since they decrease or overcome the limitations inherent for these techniques mentioned above. Refill friction stir spot welding (Refill FSSW) process is one of such technologies and has been improved and proving to be promising for the automotive industry. In comparison with RSW, some advantage as no defects related to melting and solidification of the material, and greater energy efficiency due to the low power consumption are observed. In comparison to the technique of SPR, no consumables are used, and the problems related to their cost, weight increment, and corrosion are absent [4–6].

The present work presents the application of Refill FSSW process with innovation in the welding control. The process used in this work is robotized, and the welding is controlled by the loading of the welding tool instead of its position as a conventional Refill FSSW process, which may result in a huge impact on the lifetime of the welding tools, which is an important industrial requirement. This new process variant was used for welding an AlMgSi alloy, more specifically AA6016-T4 alloy, which presents the required properties for automotive sheets such as good formability, high strength, and excellent corrosion resistance. In this project, an optimization of the process parameters for the load-controlled process was carried out. Microstructural characterization, static and dynamic mechanical characterization of the welds produced by the load-controlled process were evaluated. The results were compared with welds produced by the conventional position-controlled process with optimized process parameters.

This study was developed through a scientific and technological partnership between Federal University of São Carlos and the German research institute Helmholtz-Zentrum Geesthacht (HZG), which is a world reference in solid-state welding.

2 OBJECTIVES

This work aims at evaluating the structural and mechanical properties of AA6016-T4 aluminum alloy welds performed by refill friction stir spot welding (Refill FSSW) robotic process with load control.

The specific objectives of this work are:

- To obtain an optimized process parameter set that maximizes the mechanical performance of the welds performed with a load-controlled Refill FSSW process with anti-sticking coated tool;
- Finding the correlation between the control method (load and position), the tool design (thread and anti-sticking) with the microstructure and mechanical properties of the Refill FSSW joints;
- To compare the microstructure, static properties and dynamic properties of the welds produced by a conventional position-controlled Refill FSSW with thread tool and welds performed with a load-controlled Refill FSSW process with anti-sticking coated tool;
- Evaluating the effect of bake hardening treatment on the static mechanical properties of joints performed by Refill FSSW process with load control and anti-sticking coated tool.

3 LITERATURE REVIEW

3.1 ALUMINUM ALLOYS

3.1.1 Aluminum Alloys for Automotive Applications

Although the competition between materials is traditionally present in the automotive industry, steel has been the most used material in assembling vehicles since the 1920s. The determination on materials usage is complex and several factors should be considered. A significant influence factor on the determination of materials has been the increasing requirement to respond to environmental concerns such as fuel economy and greenhouse gas emissions. Automotive weight reduction is regarded as one of the most cost-effective means for reducing fuel consumption and gas emissions. This demand for weight reduction leads to an increasing interest in aluminum alloys to the automotive structure and exterior panels since the substitution of conventional steels by the aluminum can result in a weight reduction of up to 50%, and it has been estimated that each 10% reduction in a vehicle’s total weight decreases its fuel consumption by 7% to 10% [1, 2, 7, 8].

This particular interest in aluminum alloys for automotive applications has some reasons besides the low density, such as a strength-to-weight ratio improvement over steel on the order of 3:1, considerable corrosion resistance, good formability, and recycling potential [1, 9].

Thereby, the usage of aluminum alloy in vehicles is increasing exponentially in various automobile parts such as body-in-white, doors, hoods, motor, etc. In figure 3.1 presented in the last Ducker Worldwide Europe report, it is possible to see the significant increase of aluminum usage in North American vehicles in the last two decades, from 102 kg to 211 kg per vehicle and it forecast of 256 kg per vehicle in 2028 [10].

The most suitable aluminum alloys for automotive application are 5XXX and 6XXX series that are precipitation hardened and highly formable alloys. 5XXX series are hardened primarily by cold working, and the major alloying element is magnesium (2-5 %), and these alloys are applied where good corrosion resistance is required. 6XXX series are heat treatment strengthening alloys and contains additions of Mg (0.5-1 %) and Si (0.5-1.5 %), its application is performed where mechanical resistance is required [9].

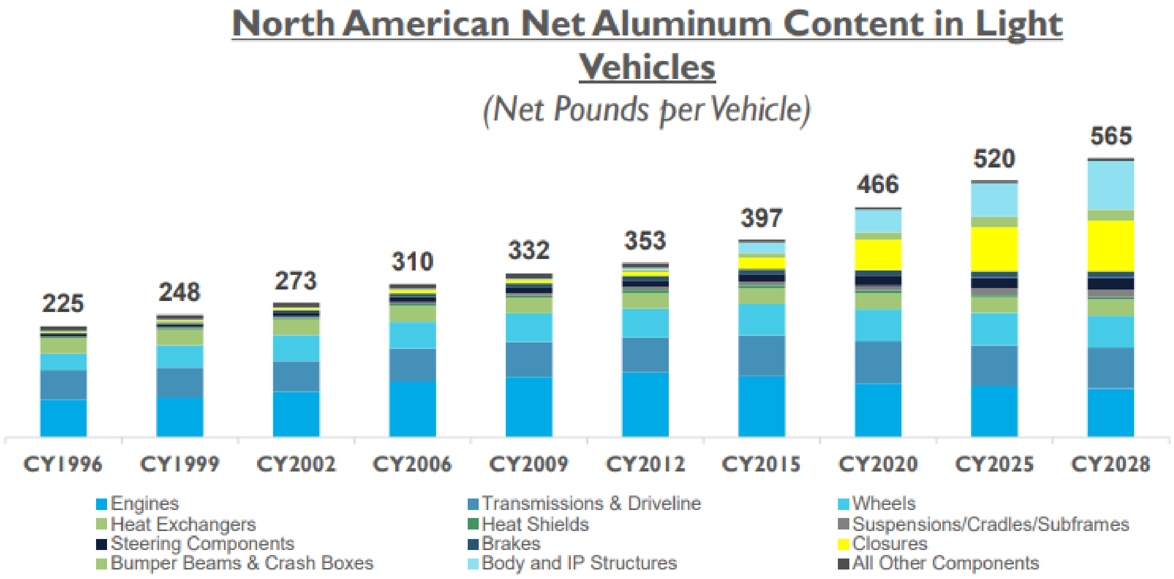

Figure 3.1 – North American net aluminum content in light vehicles since 1996 and forecasts from 2020 to 2028 (1 lb. = 0.453 kg) [10].

However, the large scale use of aluminum alloys implies a high final cost of the product due to numerous challenges such as price and adaptation of the manufacturing methods used for ferrous alloys to aluminum alloys due to the inherent properties of aluminum, as high thermal and electrical conductivity, low melting point, the high solubility of hydrogen in a liquid state, oxide layer formation and high coefficient of thermal expansion [2].

In this way, cars which are already using significant quantities of aluminum in their structures are from luxury automakers such as Audi, BMW, and Jaguar, which pass the high production costs to consumers, who are looking for a more powerful and economical car due to weight reduction, as well as the esthetics and brand value-added [11].

To illustrate some cars produced with significant quantities of aluminum, figure 3.2 shows an Audi A8 space frame consisting almost entirely of aluminum, and a mass percentage of metallic materials in Range Rover L405 structure, where the significant application of 5XXX and 6XXX series alloys can be observed.

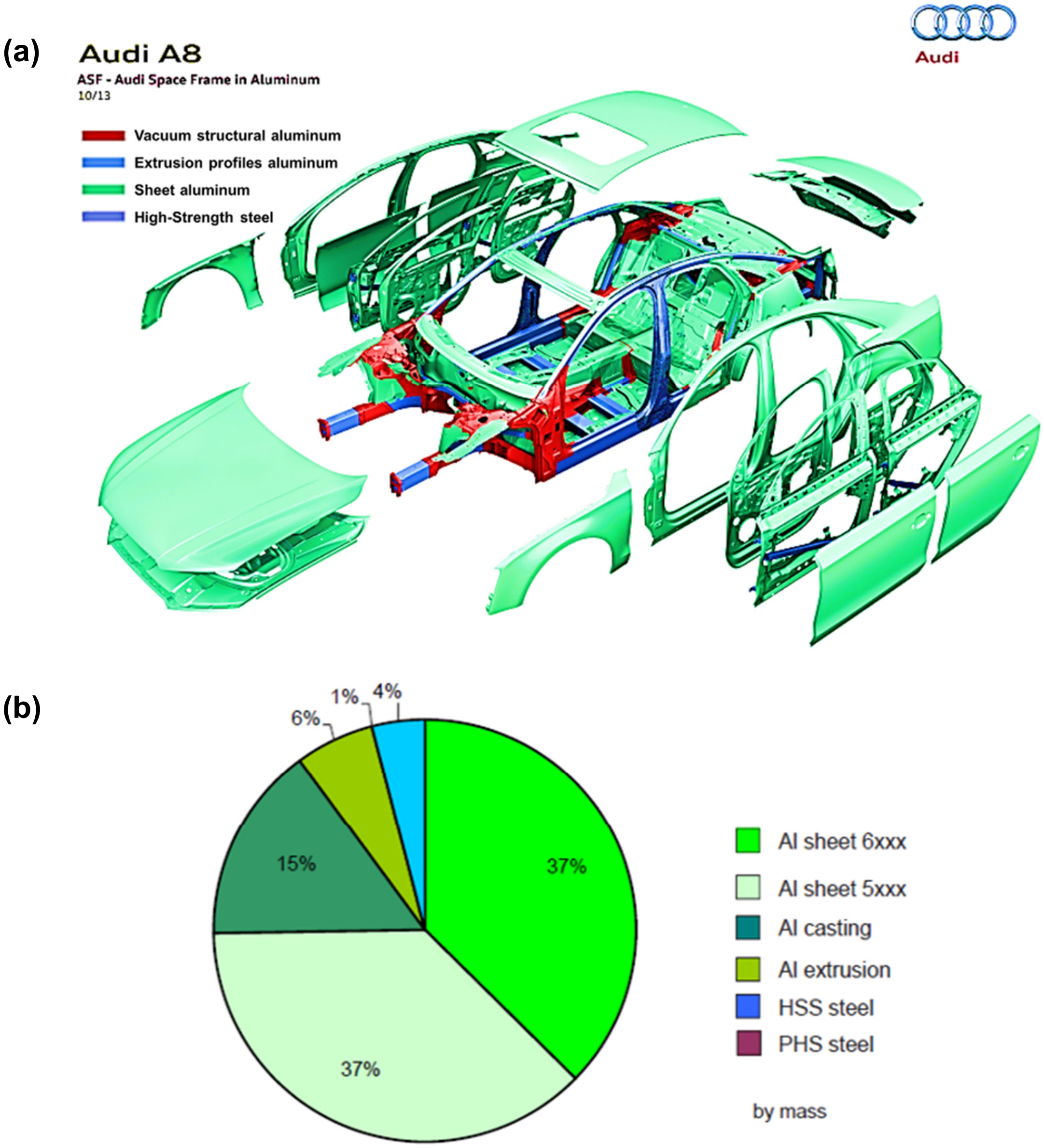

Figure 3.2 – (a) Audi A8 space frame in aluminum: vacuum structural aluminum (red), extrusion profiles aluminum (light blue), sheet aluminum (green) and high-strength steel (dark blue) and (b) Mass percentage of metallic materials in Range Rover L405 structure: aluminum – 95 % (37% Al 6XXX and 37% Al 5XXX) and high-strength steels – 5 % [11].

3.1.2 AlMgSi Aluminum Alloys

Aluminum provides weight reduction due to its low density, but its softness limits its application in engineering structures. Consequently, for the use of this material in automotive applications, strengthening is required. Therefore, aluminum is often alloyed to increase and display a good combination of properties such as strength and ductility. The alloying also affects other properties such as corrosion resistance, density, weldability, and conductivity. The main elements used to alloy aluminum are Cu, Mn, Si, Mg, Zn, and Li. It is normal to divide the aluminum alloys into two categories: wrought alloys and cast alloys. The nomenclatures have been developed by the Aluminum Association (AA), and their alloy designation system employs different nomenclatures for the two categories. For wrought alloy, a system of four digits is used according to the alloy elements, as shown in table 3.1, and according to their strengthening mechanism. The wrought aluminum alloys are divided in heat-treatable aluminum alloys, that include the 2XXX, 6XXX, 7XXX and 8XXX alloys and in non-heat-treatable aluminum alloys, including 1XXX, 3XXX, 4XXX, 5XXX and 8XXX alloys [12, 13].

Table 3.1 – Alloying elements and AA designation of wrought aluminum and its alloys [13].

Alloying elements	Designation
Pure aluminum	AA1XXX
Copper	AA2XXX
Manganese	AA3XXX
Silicon	AA4XXX
Magnesium	AA5XXX
Magnesium and silicon	AA6XXX
Zinc	AA7XXX
Lithium	AA8XXX

AlMgSi alloys are widely used in lightweight car's body outer panels due to their properties such as high strength-to-weight ratio, plasticity, good corrosion resistance, and formability. The current autobody sheets of this system are AA6009, AA6010, AA6111, and AA6016, being the latter one the most prominent alloy of this system for European car manufacturers [8, 14].

AlMgSi alloys or 6XXX alloys contain extra Si and Mg. The strengthening mechanism process consists of solution annealing, quenching, and aging, thereby precipitation and dissolution reactions occur, during which the strengthening phase is adjusted, affecting the mechanical properties and formability [12, 15].

The investigation of the precipitation and dissolution behavior during the ageing of AlMgSi alloy has been extensively studied in the last years through differential scanning calorimetry (DSC) associated with transmission electron microscopy (TEM), and energy-dispersive X-ray spectroscopy (EDS), in order to acquire information and optimizing heat treatment steps, providing a link between processing, microstructure and mechanical properties of these alloys [14–17]

It is well established the relationship between Mg_2Si precipitates and the mechanical properties of the AlMgSi alloys due to the strengthening mechanism. Coherent β” - Mg_2Si precipitates evolve from the solid solution during the heat treatment. In general, a simplified precipitation sequence from a supersaturated solid solution (ssss) for AlMgSi alloys is as follow ssss → cluster → Guinier Preston zones → β” → β’ → β (Mg_2Si). Even so, the initial alloy composition, microstructure, and initial heat treatment influences the precipitation sequence. Generally, the shape of Guinier Preston zones (GP) is considered as coherent spherical clusters, β” fine needle-shaped, β’ are rod-shaped precipitates, and β phase are usually Mg_2Si platelets [14–17].

Osten et al. [15] examined the heating behavior of some AlMgSi alloys, and the results demonstrate the complexity alternation of endothermic and exothermic reactions caused by the precipitation sequence. In figure 3.3, the heating DSC curves are shown for the 6016 alloy in the T4 (solution heat-treated and naturally aged) and T6 (solution heat-treated and artificially aged) initial conditions.

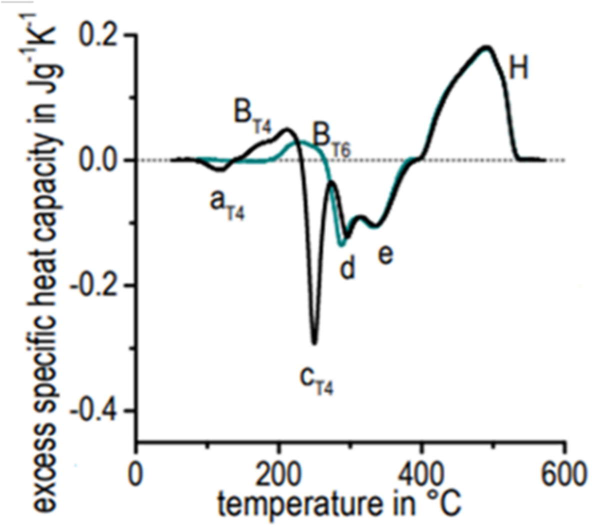

Figure 3.3 – Heating DSC curves at 0.1 K/s for AA6016 alloy for T4 (black line) and T6 (green line) initial condition [15].

For the T4 initial condition, Osten et al. [15] identify that the initial exothermic peak a_{T4}, at approximately 120 °C, is caused by the remaining potential for the formation of clusters. The endothermic reaction B_{T4}, at 220 °C, is interpreted as the dissolution of the cluster and as dissolution of GP zones; the two-step shoulder in this peak represents an overlapping dissolution reaction. The next three exothermic peaks c_{T4}, *d,* and *e* (approximately at 250 °C, 300 °C and 330 °C) are interpreted, respectively, as precipitation of β", β' and *B'*, which is established in combination with β' as well as being related to a high Si: Mg ratio.

The following endothermic peak *H* corresponds to the final dissolution of all remaining phases (β", β' and *B'*). For the T6 initial condition, Osten et al. [15] identify the similar sequence of reactions as T4 condition, but the specific differences are the non-existent peaks *a* and *c*, and the modified peak *B*, since GP zones and β" had been already precipitated in the T6 condition. The associated microstructures were evaluated by means of transmission electron microscopy (TEM) and X-ray microanalysis (EDS).

The mechanical properties of the aluminum alloys precipitation strengthening, as 2XXX, 6XXX and 7XXX alloys, vary greatly according to the heat treatment applied. In figure 3.4 is possible to see the improvement in the yield strength due to the heat treatment for the T4, T6 and T7 conditions for an AA 6014 alloy. This figure also illustrated that the improvement in the strength comes along with a reduction of ductility [18–20].

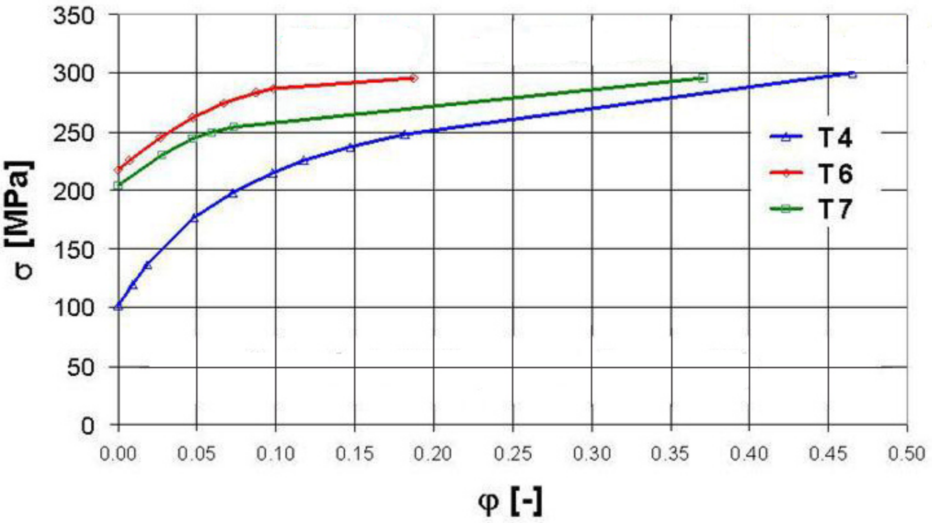

Figure 3.4 – True strain-stress curves for AA6014 alloy in different heat treatments: T4 - solution heat-treated and naturally aged, T6 - solution heat-treated and artificially aged, and T7 - solution heat-treated and stabilized (overaged) [18].

Precipitation hardening effect consists of the formation of a fine and uniform dispersion of semi-coherent precipitates that make difficult the movement of dislocations, in other words, it depends on the shape, size, and morphology of the precipitates formed during aging treatment. Four main strengthening mechanisms, as shown in figure 3.5, influence each strengthening stage of aluminum alloys. Number 1 represents a supersaturated solid solution condition, in which the strength is low since the main mechanism of strengthening involved is by a solid solution. The formation of coherent GP zones, number 2, generates strength fields around them, which makes it difficult to move the dislocations in these regions, increasing the resistance of the material compared to the condition of supersaturated solid solution. However, the dislocations are still able to overcome these shear barriers cutting them. The precipitation of coherent phases, such as the β” phase, illustrated by number 3, provides hardening through the increase in stress required to force a dislocation through a coherent zone. The maximum strength in aluminum alloys, is obtained through precipitates, such as the β” phase, which maintain high coherence with the matrix. At higher ageing times and/or temperatures, the precipitation of incoherent phases, such as the β’ phase, illustrated by number 4, precipitates become incoherent and dislocations are no longer able to cut through them [21].

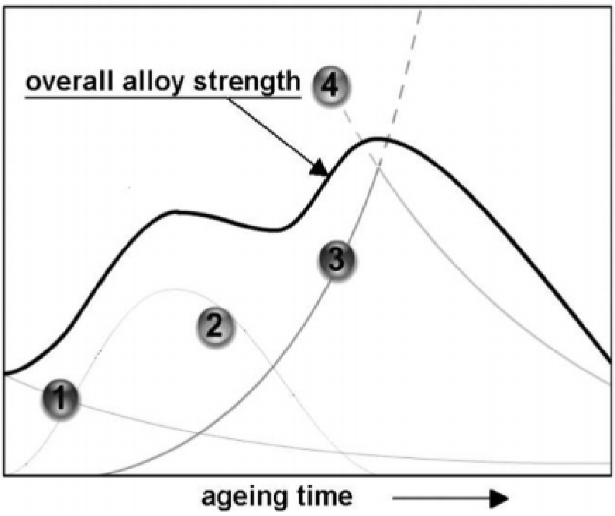

Figure 3.5 – Strengthening mechanisms and their contribution to overall strength for an aluminum alloy [21].

Table 3.2 shows the mechanical properties of AA6016 alloy subjected to different heat treatments, illustrating the versatility of this alloy.

Table 3.2 – Mechanical properties (yield strength (σ_y), tensile strength (σ_m) and elongation) of AA6016 according to two different heat treatments [22].

Heat treatment condition	σ_y (MPa)	σ_m (MPa)	Elongation (%)
T4	106	225	24
T6	210	280	11

This aluminum alloy, besides high strength-to-weight ratio, plasticity, good corrosion resistance, and good formability, has a good finish surface with no stretcher strain marks, which makes it ideal for car skin sheet applications.

Furthermore, the T4 heat treatment condition provides the two requirements: a relatively low initial strength to provide sufficient formability to make the part with complex forms and high accuracy; and high service strength after final painting treatment required during the vehicle assembling. Thus, the paint bake process provides both the curing of the paint and increasing in the hardness and strength of AlMgSi alloys due to precipitation hardening [23].

Hirth et al. [23] simulated the automotive manufacturing paint bake process through heat treatment of 30 minutes at approximately 180 °C on AA6016 alloy. The authors observed an increase in the strength with the heat treatment and that increasing Si in AA6016 alloys increases strength before and after the bake hardening. This was attributed to a complete removal of Mg from solid solution and consequently an increase in Mg-Si cluster hardening.

3.1.3 AlMgSi Aluminum Alloys Weldability

Despite the good properties of these aluminum alloys and versatility of mechanical properties values, the combination of some inherent properties of aluminum alloys makes the welding of these alloys during the vehicle manufacturing challenging. The traditional welding processes used in the automotive industry are based on the melting of the material, making the welding of aluminum alloys even challenger. Moreover, the experience obtained in welding of steels is not easily transferable to aluminum, mainly due to the physical and metallurgical differences between these materials. The low melting point, high thermal and electric conductivity, the high solubility of hydrogen, oxide formation and high solidification shrinkage produce defects during the welding of aluminum alloys, as solidification cracks, distortion, porosity and hot tears that reduce mechanical properties and fatigue strength compromising the structural integrity. Furthermore, high heat input is necessary during the welding due to the high thermal conductivity and difference of oxide melting temperature. Some of the consequences of using high heat input are possible property degradation because of elements evaporation and high energy consumption, making the process more costly [2, 4, 24, 25].

Trying to avoid liquid state welding processes, conventional mechanical joining methods that do not involve melting and solidification of the material using bolts, nuts, and rivets can be applied in automotive body assembly. Their main limitations are linked to the high cost of the mechanical fasteners that makes the production on a large scale economically unviable, the increase of weight, and the greater susceptibility to corrosion [4, 24].

Nowadays, the two main joining processes applied in aluminum alloys in the automotive industry are resistance spot welding (RSW) and self-piercing riveting (SPR). The first one is the most applied welding process for ferrous alloys in the automotive industry. The second one is a joining technique through mechanical anchoring provided by a self-drilling steel rivet. Thereby, cars with intense use of aluminum alloys still represent a challenge due to the limitation of joining technologies [2, 4, 24].

Resistance spot welding requirements of aluminum differ greatly from those of steel due to the limitations, discontinuities, and cost. Therefore, special equipment, such as high thermal and electrical conductivity and high hardness electrodes, and constant maintenance should be applied. Moreover, the surface condition is extremely important; thus the removal of the oxide layer and remnant lubricants or oils by mechanical or chemical means becomes necessary before the welding procedure, to improve the electrodes life [3, 9, 24].

Mechanical joining processes offer the possibility of assembly aluminum structures without thermal effects associated with welding. The most attractive mechanical joining process for the automotive industry is SPR, which uses a self-drilling steel rivet to join sheets. Some limitations of this process are related to the high cost of the rivets that makes the production on a large scale economically unviable. In addition, other limitations are the weight increment and the greater susceptibility to corrosion, which makes necessary the use of rivets with surface coating for corrosion protection [9, 24].

To minimize these limitations related to traditional joining processes, solid-state joining techniques have been developed and studied since the 1990s, such as friction stir welding (FSW), friction stir spot welding (FSSW), and refill friction stir spot welding (Refill FSSW). The main advantages associated with solid-state welding are the absence of problems related to thermal effects, such as porosity, distortion, and cracks, besides no consumables usage and low energy consumption [5, 24].

The International Automotive Research Centre from the University of Warwick in the United Kingdom published a study comparing three welding technologies, RSW, SPR and, FSSW (spot friction joining – SFJ, in figure 3.6), for aluminum automotive sheet, analyzing mechanical properties of the joints and the economic feasibility between these techniques. With an emphasis on the cost associated with each of these techniques, it was observed that to the installation of a plant with an annual production of 35,000 cars over 10 years, SPR technology will involve a higher consumable cost than RSW. Although RSW is economically profitable in the short term, this technique would have a cost with electric consumption that, in the long term, would make it less cost-effective than FSSW, which currently has a high cost in joining equipment and robots as shown in figure 3.6 [4].

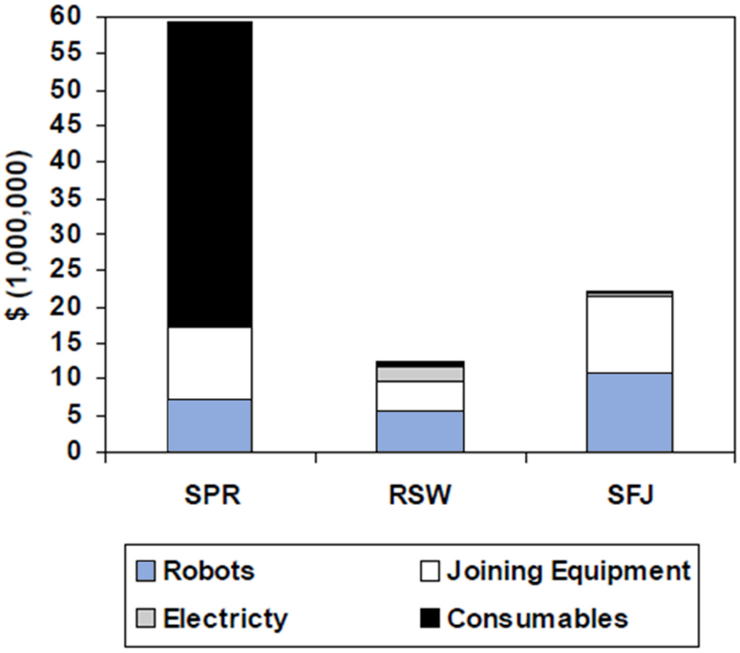

Figure 3.6 – Comparison of the costs associated with an installation of a plant with an annual production of 35,000 cars during ten years for SPR, RSW and FSSW techniques [4].

3.2 REFILL FRICTION STIR SPOT WELDING

Solid-state joining techniques have been developed and studied since the 1990s as an alternative to traditional welding processes to minimize its limitations, such as thermal effects, and increase of weight and susceptibility to corrosion. Friction stir welding (FSW) was developed in The Welding Institute (TWI), in the United Kingdom, in 1991 as a linear welding process based on intense plastic deformation and heat generation due to the friction between non-consumable tool and material. FSW has been employed to join similar and dissimilar materials such as aluminum, copper, magnesium, titanium, zinc, steel, etc., for aerospace, automotive, and marine industry [24, 26, 27].

However, spot welding processes are more demanding in the transportation industry; therefore solid-state spot welding processes such as friction stir spot welding (FSSW) and refill friction stir spot welding (Refill FSSW), also known as friction spot welding (FSpW), was developed based on the FSW, as an alternative to RSW and SPR. FSSW was developed in 2001 in Japan for Mazda Motor Corporation, and the main difference is the absence of the transversal tool movement since the non-consumable tool used is the same as the FSW process, composed by a shoulder and a prominent probe. Mazda applied this process in the RX-8 vehicle to assembly the rear doors and hood in aluminum, replacing the RSW. After, it was also used on the trunk lid of the MX-5 vehicle. Since the FSSW process does not require compressed air and high electric current, the power consumption is drastically reduced, which is required only for tool rotation and axial force application, besides the low investment in machinery. This power reduction is approximately 99% for aluminum alloys welding procedure [6, 24, 28]

Refill FSSW was originally developed and patented by GKSS Forschungszentrum Geesthacht GmbH (actual Helmholtz-Zentrum Geesthacht – HZG), in Germany [29]. This process has been suitable for the production of similar welds of aluminum and magnesium, and dissimilar welds such as Al/Mg, Al/Cu, Al/Ti, Al/Polymer and Al/Steel to structural applications [5, 6, 29–34].

Unlike FSSW, no keyhole is left on the surface after Refill FSSW procedure, which is an advantage, since the reminiscent superficial hole acts as a tension and corrosion concentrator, besides reducing the effective weld cross-section. Thus, it is being considered as the most promising technology to replace RSW and SPR. In figure 3.7 are shown the resulting welds of FSSW and Refill FSSW processes. The keyhole is related to the tool used in the FSSW process, and its absence improves the mechanical properties of the joint, as tensile and fatigue strength [6, 35, 36].

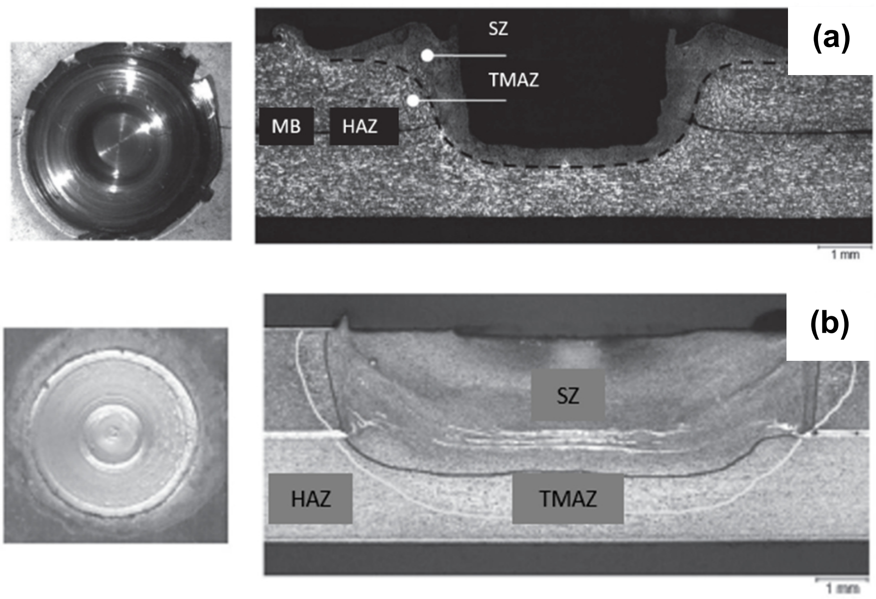

Figure 3.7 – Superficial and cross-section features of the resulting welds performed with (a) FSSW and (b) Refill FSSW [6].

The non-consumable Refill FSSW process tool consists of three concentric parts: probe, sleeve, and clamping ring, as shown in figure 3.8. The non-rotating part is a clamping ring, and its main function is keeping the sheets to be welded fixed and prevents the escape of plasticized material from the weld region. The rotating probe and sleeve can move up and down independently, and its main function is heat generation, to realize the stirring and the refilling of the plasticized material [36].

Refill FSSW process can be divided into two variants, probe plunge (PP) variant, and sleeve plunge (SP) variant. Although PP is more easily performed because it requires lower force and torque intensities due to the smaller probe diameter, which results in longer tool life, SP variant is the most commonly used because it produces a larger effective welded area due to the largest sleeve diameter relative to the probe, and consequently, better mechanical properties. SP variation of Refill FSSW process is schematically shown in figure 3.9 [6, 37].

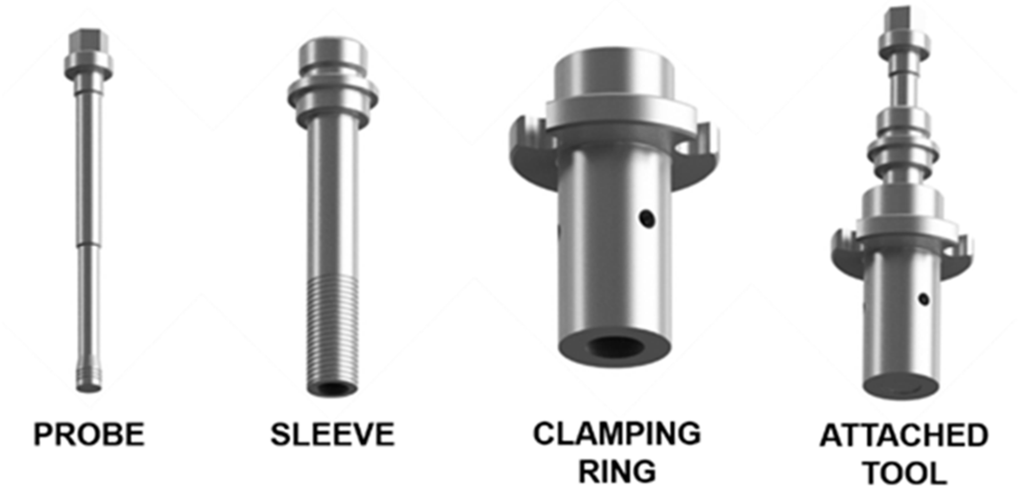

Figure 3.8 – Schematic illustration of the toll components: probe, sleeve and clamping ring, and the attached tool in a concentric way.

As shown in figure 3.9, the process is divided into four stages. First, the tool is put on the sheets with defined clamping force to keep the specimen fixed while the probe and sleeve rotate on the sheets with the same angular velocity and direction (stage 1). Second, the sleeve plunges into the material and plasticizes it at the same time as the probe is retracted and provides space for the plasticized material extruded by the sleeve movement (stage 2). Third, after reaching the specified plunge depth, the sleeve and the probe retract and move downward, respectively. Therefore, the plasticized material moves out of the sleeve cavity into space provides by the probe retraction in stage 2 can be refilled into the weld (stage 3). Fourth, both the probe and the sleeve are in the original position, and the tool is retracted from the weld surface, leaving a free-keyhole weld (stage 4) [6, 36].

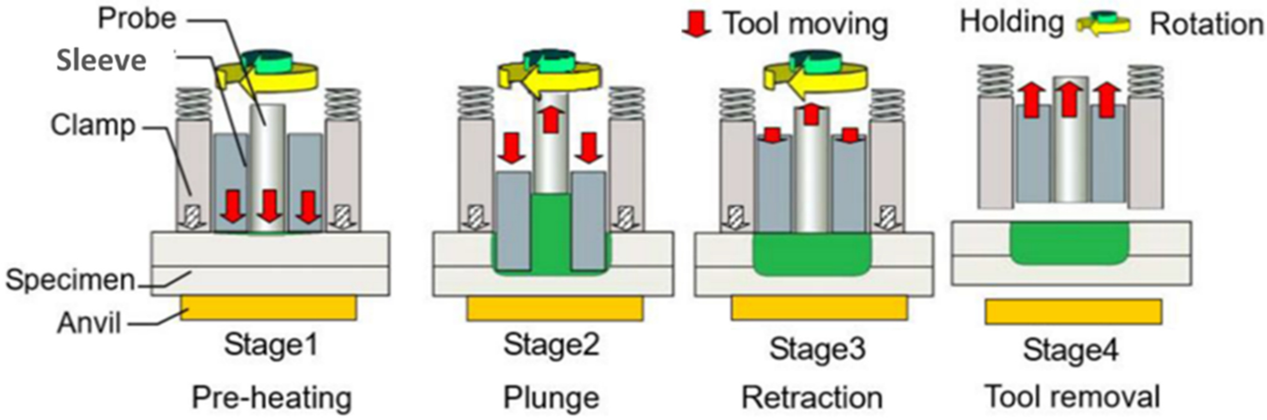

Figure 3.9 - Schematic illustration of SP variant of Refill FSSW process: Stage 1 – Pre-heating and specimen fixation; Stage 2 – Sleeve plunge and probe retraction; Stage 3 – Return of the tool to the starting position, and Stage 4 – Tool removal [Adapted from 38].

3.2.1 Comparison Between by Load- and Position-controlled Refill FSSW process

During the welding process, an axial force acts on the three tool components to enable the fixation of the sheets by the clamping ring, the sleeve penetration until specified plunge depth, and the refilling of the cavity by the downward movement of the probe to the original position after its retraction. Moreover, the total force acting in the sheets is called a welding force and is determined through a load cell in the anvil part (figure 3.9).

The main difference between the process controlled by load and position is related to the sleeve plunge and probe retraction (stage 2). In the position-controlled welding, the determined time of each stage (stages 1, 2, 3, and 4) are set on the machine and strictly followed, i.e., during stage 2, the sleeve will reach depth programmed within the set time (sleeve penetration rate). However, during the load-controlled process, rather than setting the times of each stage, the force in each tool component is set. Thus, during stage 2, the force acting on the sleeve does not change, and the penetration rate cannot be controlled, i.e. the penetration rate of the sleeve depends on the material flow stress, temperature of the tool and of the material, and the resultant imposed resistance. This is an important advantage in the matter of tool stress, but it implies an increase in the total welding process time.

Furthermore, the load-controlled process presents a clamping ring force constant, and the total force subtracted of the clamping ring force is equal to the probe force plus the sleeve force. In the position-controlled process, the total force is constant, and the forces in the three components are different throughout the process.

These differences also reflect the welding parameters that must be set during the process. The main welding parameters for the load control are clamping force, rotational speed (RS), plunge force (PF), and retracting force (RF) of both sleeve and probe, and sleeve plunge depth (PD) (based on these parameters the probe retraction is determined). However, for the position control, the main parameters are welding time (WT), axial force (F), RS of both sleeve and probe, and sleeve penetration rate (PR) and PD.

Another consequence of these differences is in the tool components. To intensify the flow of material during the process controlled by position, mainly during Stage 2, the sleeve has an externally threaded surface. In the load-controlled process, the tools have no threads, and have an anti-sticking coating, to ensure the material does not stick to tools compromising weld quality.

Finally, another characteristic of the load-controlled process is an additional stage with a shallow probe plunging in comparison with the position-controlled process, as shown in figure 3.10.

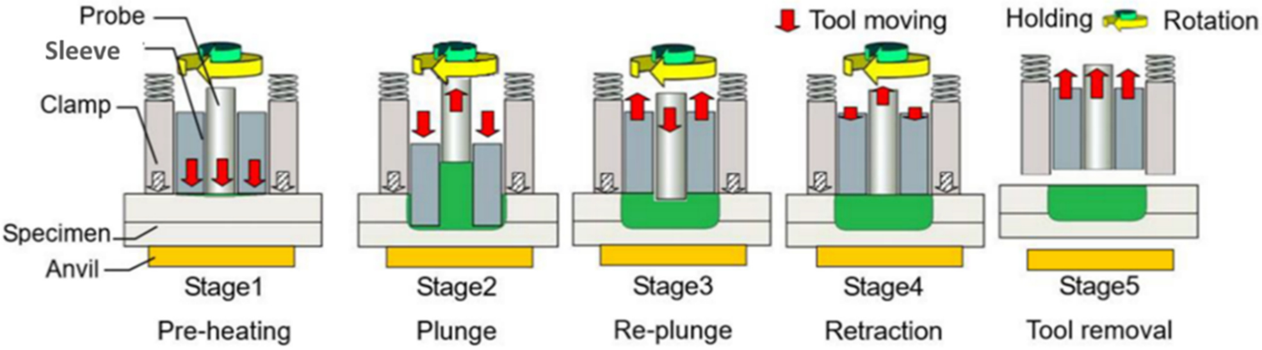

Figure 3.10 – Schematic illustration of SP variant of Refill FSSW process controlled by the load with an additional stage (stage 3) [38].

Stage 3, in this case, corresponds to the re-plunge performed by the probe and is indispensable for the process to avoid superficial defects in the welds, such as lack of refill and thickness reduction.

3.2.2 Microstructures Features of Refill FSSW Joints

During the solid-state welding process, the tool has important functions as heat generation and material flow to produce the weld spot. Welds produced by Refill FSSW show different microstructural regions along with the specimen due to a combination of heat and displacement rate associated with the tool movement and the base material microstructure. The typical four microstructural regions observed by optical microscopy (OM) in a typical joint performed by Refill FSSW are stir zone (SZ), thermomechanically affected zone (TMAZ), heat affected zone (HAZ) and base material (BM) as shown in figure 3.11 [36, 37, 39–41].

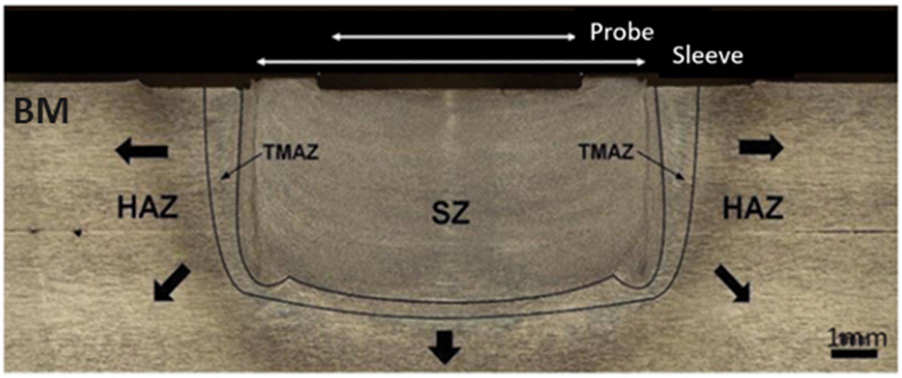

Figure 3.11 – Typical microstructural regions along the cross section of an AA 2198 specimen performed with Refill FSSW process: stir zone (SZ), thermomechanically affected zone (TMAZ), heat affected zone (HAZ) and base material (BM) [adapted from 41].

SZ corresponds to the center of the weld region and is the region where the material is under severe plastic deformation and high process temperature due to the tool stirring contact. These conditions lead to dynamic recrystallization resulting in very fine and equiaxed grains. No defects, such as voids, or thickness reduction is typically observed in this region [41].

The adjacent region is TMAZ that is in contact with the external surface of the sleeve during the welding process and lies between the SZ and HAZ. This region is subjected to moderate plastic deformation and temperature, which are not in sufficient levels to induce the dynamic recrystallization, resulting in fine deformed grains [41, 42].

HAZ corresponds to the region between TMAZ and BM that does not experience plastic deformation while it is affected by moderate temperature due to the alloy's thermal conductivity. It is common for the HAZ to be identified by hardness measurement. Finally, BM is the region not affected by the process [42].

Some features such as hook and oxide line remnant were also observed in a typical weld cross-section, as shown in figure 3.12. The hook, figure 3.12 (A), is formed at the transition between SZ and TMAZ regions, more specifically between the unwelded and the metallurgically bonded region of the plates. There are different propositions about the hook formation. Badarinarayan et al. [44] and Rosendo et al. [34] determined the hook formation due to the upward bending of the interface of the sheets caused by the tool penetration in the bottom plate. Besides, Rosendo et al. [34] pointed out that the hook formation is controlled by the heat input during the welding, and it is inherent to the process. Shen et al. [43] attributed it to the tool penetration in the bottom plate, and to the lack of mixing of the plates due to the poor flowability of materials. The oxide line remnant, figure 3.12 (B), which is a remaining line of oxides from the original interface of BM, is in the interface region between the upper and the lower sheets, and demonstrates the flow behavior in the interface of the sheets, which is symmetric about the weld center, and has an arc-shape in the center and zigzag in the edge. However, this layer results in a good adhesion interface between plates with satisfactory strength [34, 36, 40].

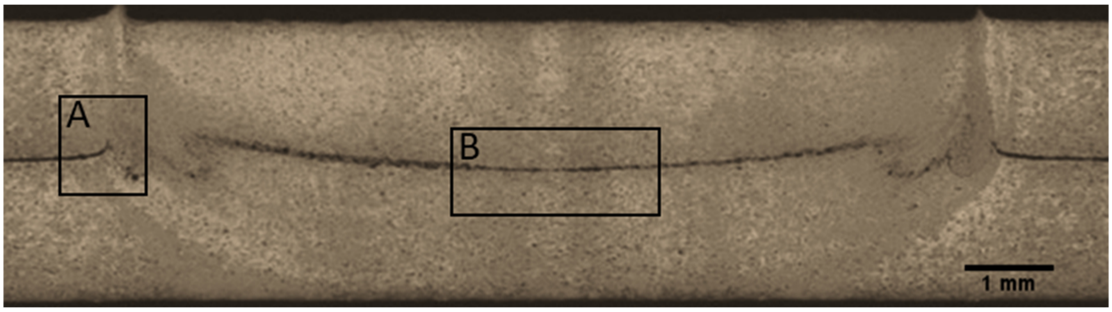

Figure 3.12 – Hook (A) and oxide line remnant (B) of a cross section of a spot weld performed by Refill FSSW process.

3.2.3 Mechanical Properties of Refill FSSW Joints

The different microstructural zones along with the specimen due to a combination of heat and displacement rate associated with the tool movement, mentioned above, can also be observed by hardness measurements since these thermal and mechanical inputs affect the original state and distribution of the precipitates. In a precipitation hardening aluminum alloy, the changes observed in the precipitates during and after welding procedure will be the most important phenomena influencing the hardness and strength results of the different weld zones, since these mechanical properties are more influenced by the size, volume fraction and distribution of the precipitates [34, 43].

Vickers microhardness profile through the mid-thickness of the upper and lower sheet of the Refill FSSW joint of AA7050-T76, a precipitation hardening aluminum alloy, is shown in figure 3.13. The Vickers microhardness profile is symmetric with respect to the center-line of the weld and exhibits a W-shape appearance and lower hardness value in the transition between TMAZ and HAZ. In the SZ, the intense plastic deformation and high temperature cause dynamic recrystallization, and the main reason for the hardness increasing of this zone is related with the solubilization of the precipitates due to the high temperature during the welding, and their re-precipitation during the cooling stage, after the welding procedure. In the TMAZ, the precipitation coarsening is the predominant phenomenon acting due to the moderate plastic deformation and temperature. These deformation and temperature levels imposed by the tool can also produce some strain hardening in this region, but it is not enough to suppress the softening caused by the precipitation coarsening. The hardness in the HAZ has associated mainly with the recovery of BM microstructure due to the not so high temperature reached in this region during the welding procedure [34, 43, 45, 46].

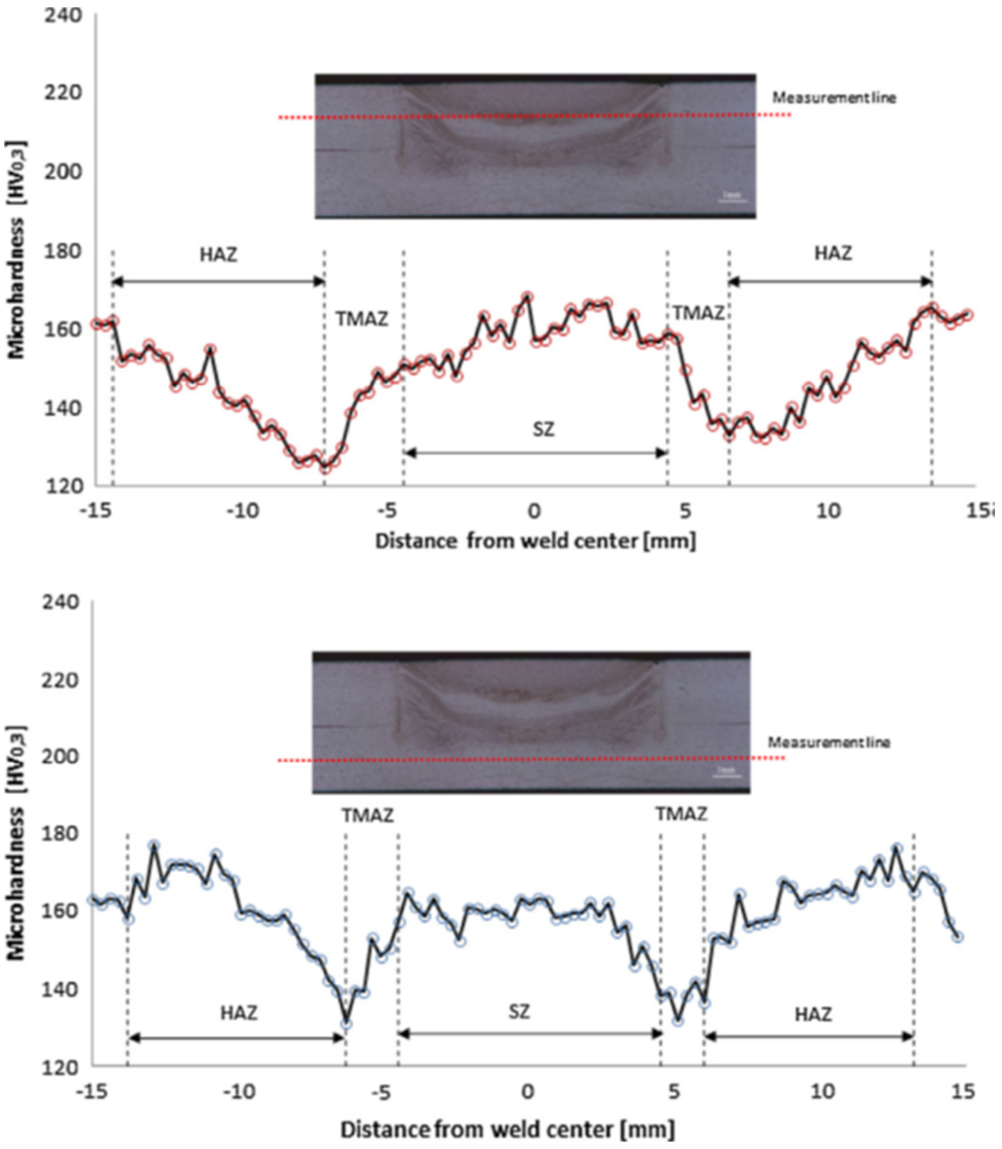

Figure 3.13 – Microhardness profile ($HV_{0.3}$) through the mid-thickness of the upper and lower sheet of the Refill FSSW joint of 7050-T76 aluminum alloy [45].

In order to compare the effect of the welding process in the hardness profile across the welding region, in figure 3.14 is shown a hardness profile of RSW joint, also of precipitation-hardened aluminum alloy, AA6082-T6, in which is observed a significant decrease in hardness in the weld spot. This phenomenon is attributed to the total dissolution of strengthening precipitates, in heat treatable aluminum alloys, since this welding process causes a local fusion of the materials. Besides, the softening of the HAZ is mainly related to the coarsening of precipitates [47].

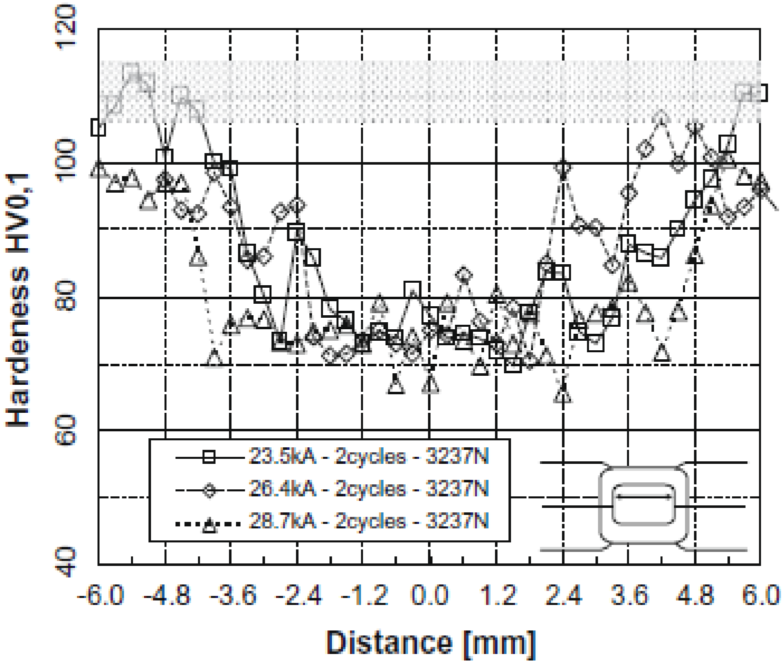

Figure 3.14 – Microhardness profile ($HV_{0.1}$) through the RSW joint of 6082-T6 aluminum alloy performed with three different weld currents: 23.5, 26.4 and 28.7 kA (increasing weld current increases the nugget size or weld spot, also the width of the HAZ). The grey bar illustrates the hardness of the base material. [47].

The weld strength behavior during shear loading is most driven by the hook features and the width of the welded area. However, the different microstructure zones, oxide line remnant, presence of voids, lack of refill, and lack of mixing must also have some effects in lap shear strength (LSS). The hook feature works as a crack nucleation site, and its shape, as sharpness and height, have influence in the crack initiation and propagation. Studies reported by Cao et al. [39] and Barros et al. [49] regarding the Refill FSSW of AA6061-T6 2 mm-thicker and AA2198-T8 1.6 mm-thicker, respectively, associate a better strength behavior to welds with lower hook height values, since a higher hook height results in a smaller effective resistive area above the hook tip. Concerning the width of the welded area, higher mechanical resistance of the weld is associated with the larger welded area. About the oxide line remnant, its effectiveness is important not only for the satisfactory resistance but also fracture behavior of the weld. The different microstructures zones, as mentioned above, have different hardness along to the cross-section, which can also contribute to the fracture behavior. Finally, the other features such as voids, lack of refill, and lack of mixing are critical factors for the mechanical properties since they can act as crack nucleation sites [34, 37, 40, 48, 50].

Several studies were reported in the literature pointing out two typical fracture modes that cause the failure during lap shear loads in aluminum sheets joints performed by Refill FSSW, which are through-the-weld and pull-out. Through-the-weld failure mode, also reported as shear fracture, is related to the nucleation of the crack in the hook feature and its propagation through the weld interface across the SZ. Pull-out failure mode, also referenced as plug fracture, is associated with the circumferential crack around the spot weld, a region characterized by a drastic change of hardness, as shown in figure 3.13. Complete separation of the spot weld from the upper sheet occurs, leaving a circular hole on it [40, 43, 51].

Some studies of Refill FSSW have shown excellent lap shear strength for welds of similar aluminum alloys with different thicknesses, as shown in figure 3.15. All the lap shear strength values are above that required by the specification of the American Welding Society for aerospace applications [34, 36, 41, 42, 45, 48, 50-53].

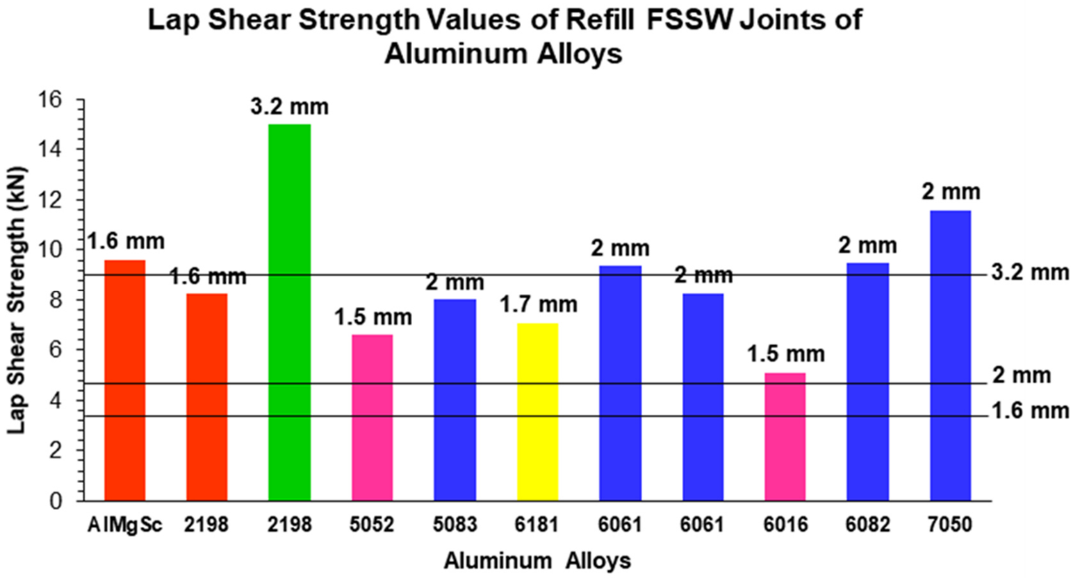

Figure 3.15 – Lap shear strength values of Refill FSSW joints of aluminum alloys with different sheets thicknesses (identified by colors and their values above the column) and the minimum lap shear strength in accordance with the specification of the American Welding Society – AWS D17.2/D17.2M:2013 Specification for Resistance Welding for Aerospace Applications, for three different sheet thicknesses (horizontal lines) [34, 36, 41, 42, 45, 48, 50-53].

As reported in several studies, there is a wide variation in LSS for different aluminum alloys, thickness, and welding processes used to joint it. For 2 mm-thick AlMgSi alloys, for example, Uematsu and Tokaji [54] reported an LSS equal 5.241 kN and 2.948 kN for joints performed by RSW and FSSW, respectively, Yuan et al. [55] on their study obtained an LSS equal 4.310 kN for joints performed by SPR, and Cao et al. [50] obtained for Refill FSSW joints an LSS equal 9.093 kN. These LSS values are illustrated in figure 3.16.

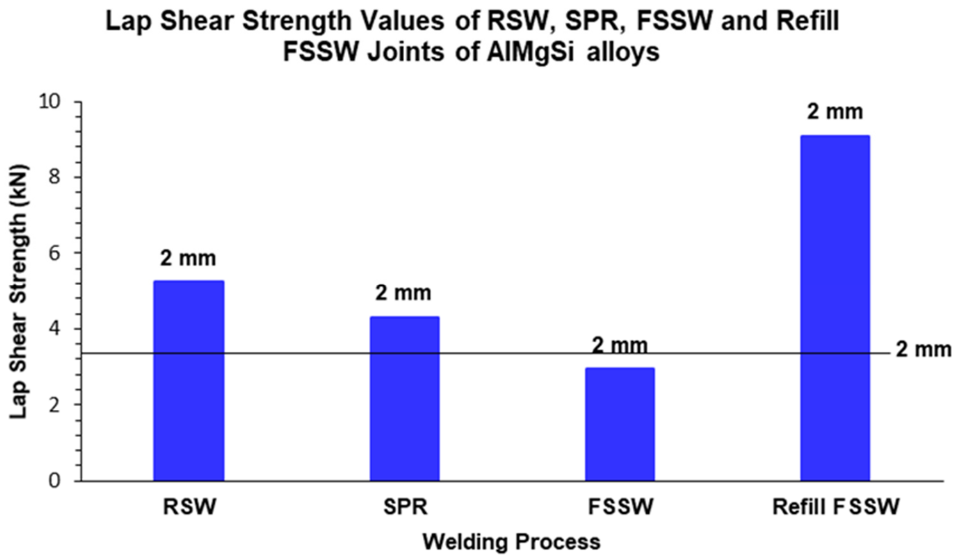

Figure 3.16 – Lap shear strength values of joints obtained by different techniques – RSW, SPR, FSSW, and Refill FSSW – in 2 mm-thick plates. The horizontal line represents the minimum lap shear strength in accordance with the specification of the American Welding Society – AWS D17.2/D17.2M:2013 Specification for Resistance Welding for Aerospace Applications [50, 53-55].

Results about the welding behavior under cyclic loads, i.e., dynamic properties of joints performed by Refill FSSW, are rarely found in the literature. Studies reported by Plaine et al. [56] regarding the fatigue behavior of Refill FSSW dissimilar welds of AA5754 and Ti6Al4V alloys, Effertz et al. [45] in their work with similar welds of AA7050-T76, as shown in figure 3.17, and Lage et al. [48] on their with AlMgSc alloy, present high fatigue life (>10^6 cycles) only for lower stress level (high-cycle loading). In their reports, a fatigue limit of 15%, 10% and 9% of LSS (static load) was obtained, respectively. Besides, Brzostek et al. [57], in their study with similar welds of AA2024-T3, reported a fatigue limit (> 10^7 cycles) of 15% of LSS.

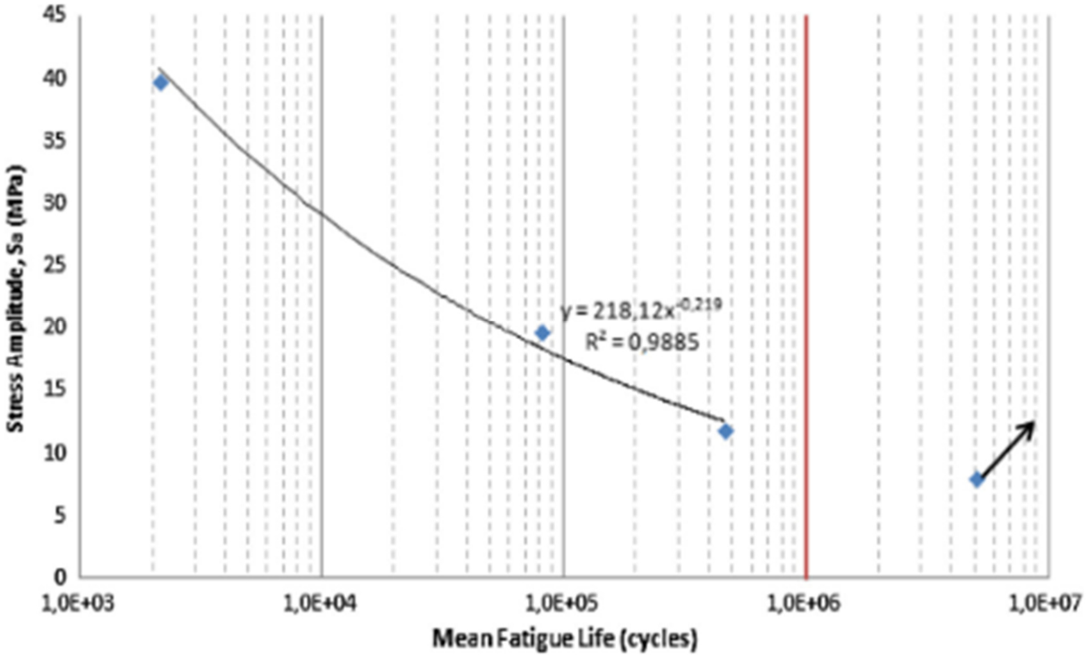

Figure 3.17 – The S–N curve obtained for the average fatigue life of AA7050-T76 similar Refill FSSW joints [45].

Plaine et al. [56] and Effertz et al. [45] found two distinct failure modes resulted from fatigue tests depending on the stress level applied. Plaine et al. [56] reported that under low-cycle loading conditions, the through-the-weld failure was the final fracture mode, and under high-cycle, the fatigue cracks initiate at the notch tip (in dissimilar Refill FSSW joints are not observed a hook feature) of the interface of the upper and bottom sheets and propagate through the thickness of the upper sheet (eyebrow failure mode). Effertz et al. [45] reported two fracture modes, under low-cycle loading conditions, the pull-out failure mode was reported, and under high-cycle loading, the failure propagation through the thickness sheet has seemed. Lage et al. [48] observed that the fracture initiate in the hook feature and propagate through the region between the TMAZ and SZ, then fractures through the thickness of the upper sheet and bottom sheets were reported. Brzostek et al. [57] found three different fracture modes, under low-cycle loading conditions, the pull-out failure mode was reported, and under high-cycle loading conditions fractures through the thickness of the upper sheet and bottom sheets were observed, as reported by Lage et al. [48].

In comparison with fatigue results obtained by resistance spot welding (RSW), self-piercing riveting (SPR), and friction stir spot welding (FSSW) processes reported in the literature, a high fatigue limit is also correlate with low-stress loading. Fu and Mallick [58] evaluated the fatigue behavior of SPR joints in 1 mm-thick AA6111-T4 sheets and observed a fatigue life of 1.067 kN (40% of the static strength or LSS). Similar results were obtained by Huang et al [59].

A comparative study of the SPR and RSW joints in 2 mm-thick AA5754 sheets performance conducted by Krause and Chernenkoff [60] shows that at 10^6 cycles the fatigue strength of SPR joints is twice that of RSW. However, under static loading RSW joints are stronger than SPR joints. Booth et al. [61] also conducted a comparative study about fatigue behavior between SPR and RSW joints in 1.2 mm-thick AA5754 sheets and observed the same result, the fatigue strength of SPR joints after 10^6 cycles was twice that of RSW joints.

Uematsu and Tokaji [54] conducted a comparison study of fatigue behavior between RSW and FSSW in 2 mm-thick AlMgSi alloy sheets and observed that when normalized by the welded area, FSSW joints have higher fatigue strength than RSW joints. Without normalization, under 0.8 kN the RSW joints achieve 10^7 cycles, while FSSW joints achieve the same number of cycles under 0.5 kN loading, as shown in figure 3.18. Finally, Effertz et al. [45] observed a fatigue limit at $5x10^6$ cycles under 1.13 kN for Refill FSSW joints of 2 mm-thick AA7050 sheets.

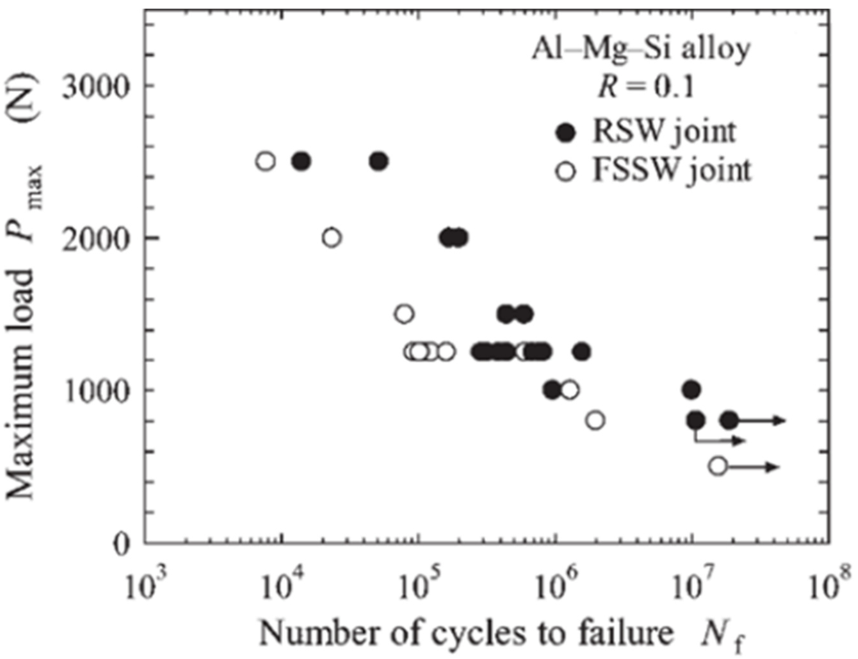

Figure 3.18 – Comparison of fatigue strength between RSW and FSSW of AlMgSi similar joints characterized in terms of a maximum load [55].

However, the Refill FSSW fatigue data, and the others mechanical properties values, presented above is related to position welding control. There are no reported data of fatigue tests of welds produced by Refill FSSW with load control. Then, this work intends to fill part of this gap evaluating static and dynamic mechanical properties, after a welding parameters optimization study, as well as the microstructural characteristics of welds produced by load-controlled Refill FSSW.

4 MATERIALS AND METHODS

4.1 MATERIAL

The material used in this project is AA6016-T4, an AlMgSi alloy under T4 condition (solution heat-treated, and naturally aged), in which nominal chemical composition is presented in table 4.1. The specimens' dimensions are 100 mm x 25.4 mm x 1.5 mm, in the shape of sheets. Table 4.2 presents the mechanical properties, such as elasticity modulus (E), yield strength (σ_y), tensile strength (σ_m), elongation, and Vickers microhardness ($HV_{0.2}$).

Table 4.1 – Chemical composition (mass %) of AA6016 [62].

Material	**Si (%)**	**Mg (%)**	**Fe (%)**	**Mn (%)**	**Zn (%)**	**Cu (%)**	**Ti (%)**	**Cr (%)**	**Al (%)**
AA6016	1.0-1.5	0.25-0.6	0.5	0.2	0.2	0.2	0.15	0.1	bal.

Table 4.2 – Mechanical properties of AA6016-T4 [22].

Material	**E (GPa)**	**σ_y (MPa)**	**σ_m (MPa)**	**Elong. (%)**	**Microhardness ($HV_{0.2}$)**
AA6016-T4	69	106	225	24	60

4.2 WELDING PROCESS

4.2.1 Load-controlled process

The spot welds for this study were performed using a Kawasaki Heavy Industries (KHI) robot with load control welding and a sleeve plunge variation that is in Solid State Joining Processes Department (WMP) in Institute of Materials Research / Material Mechanics in the German research institute Helmholtz-Zentrum Geesthacht (HZG). The KHI robot has an interface software that allows the programming of the welding parameters, as rotational speed (RS, in rpm), plunge force (PF, in kN), retracting force (RF, in kN) and plunge depth (PD, in mm). The software interface also allows to monitor the welding time, force, and position of each tool component during welding.

The tool used to perform the spot welds is made of hard metal and consists of three concentric parts, two rotating parts, probe and sleeve, and a non-rotating part, clamping ring, with external diameters of 15 mm, 9 mm and 5 mm, respectively. These tools have an anti-sticking coating and have no threads. To ensure correct adjustment and positioning of the sheets at the welding time, a fixation device was used. Figure 4.1 illustrates the KHI robot and the tool.

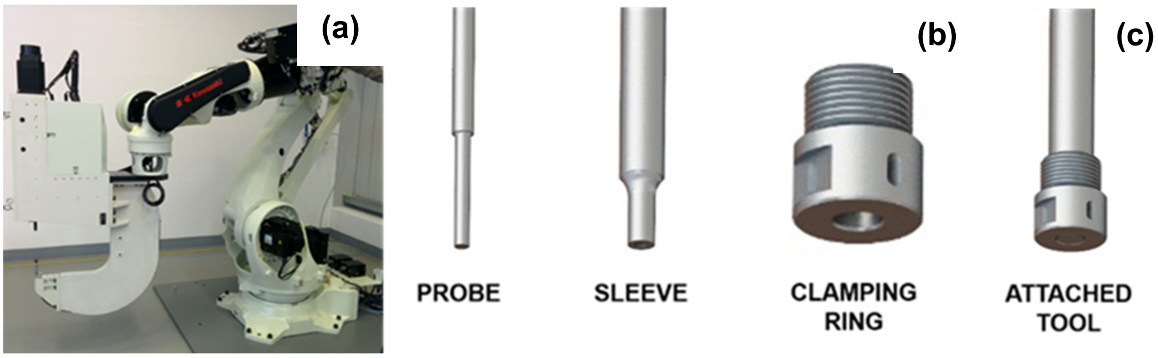

Figure 4.1 – (a) KHI Robot and (b) Tool components: probe, sleeve, and clamping ring with external diameters of 15 mm, 9 mm, and 5 mm, respectively. (c) The attached tool with all three concentric tools.

To obtain reproducible and uniform welds, the aluminum alloy sheets were cleaned with ethanol immediately before the welding process to eliminate residues, such as greases and oils, that could modify the quality of the process. Another procedure was to maintain the alignment between the probe and the sleeve at the same level on sheets to be welded.

4.2.2 Position-controlled process

In order to compare the results obtained by the load-controlled process, some spot welds were performed using the Harms-Wende RPS100 machine, which has position control welding and a sleeve penetration variant also located at HZG institute. The machine has an interface software that allows control of process parameters, such as RS (rpm), PD (mm), penetration rate (PR, in mm/s), welding time (WT, in s) and axial force (F, in kN), besides monitoring the position of the probe and sleeve during the whole process.

The tool is composed of the same three concentric elements, clamping ring, sleeve and probe with external diameters of 17 mm, 9 mm and 6 mm, respectively. The tool is made of hotvar steel (high-performance molybdenum-vanadium alloyed hot-work tool steel). The sleeve has an externally threaded surface to intensify the flow of material during the process. The welding machine and the tool are shown in figure 4.2.

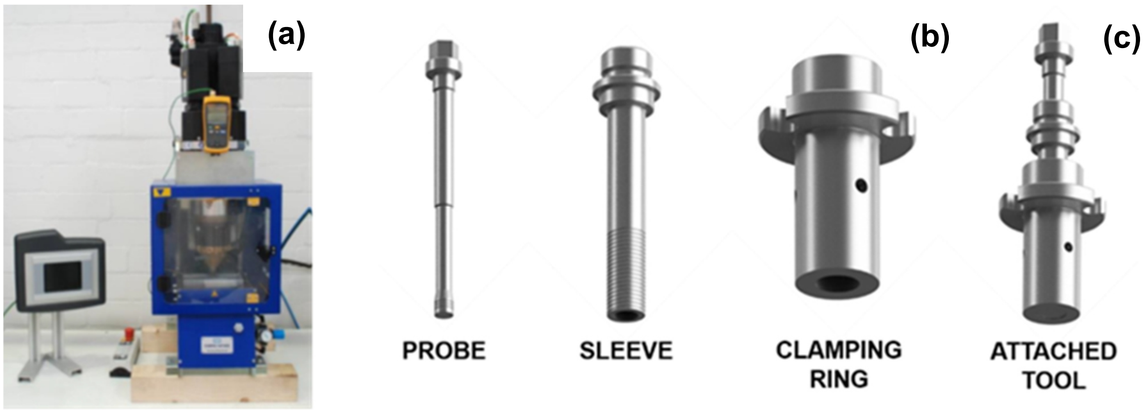

Figure 4.2 – (a) Harms & Wende RPS 100 machine and (b) Tool components: probe, sleeve, and clamping ring. (c) The attached tool with all three concentric tools.

The process parameters used for the welding of these samples were determined in a previous study of the research group that aimed the parameters optimization for the same aluminum alloy with the shortest possible welding time. These parameters are present in table 4.3.

Table 4.3 – Process parameters of the position-controlled process.

	RS (rpm)	**PD (mm)**	**F**
Optimized	2100	1.6	10.5 kN

4.3 PARAMETERS OPTIMIZATION FOR LOAD-CONTROLLED PROCESS

4.3.1 Processing Window

The initial processing window was determined based on previous experiments of the research group in HZG performed in Harms & Wende RPS100 machine for a position-controlled process since the present study using a load-controlled process was the first one carried out by this research group and has only one study reported in the literature [63]. Thereby, the initial stage of this study consisted of welding by load-controlled Refill FSSW in the KHI robot, to confirm the efficiency of the initial window of process parameters in terms of weld production with the absence of defects, such as porosity and lack of refill. The initial processing window is shown in table 4.4.

Table 4.4 – Initial processing window.

	RS (rpm)	**PD (mm)**	**RF (kN)**
Minimum	1500	1.4	7
Maximum	2100	1.8	9

The process parameters varied in this study were RS, PD, and RF, being the latter parameter exclusive of the load-controlled Refill FSSW process. The PF, another exclusive parameter, was kept constant and equal 10 kN during the whole welding process in all combinations of RS, PD, and RF.

4.3.2 Design of Experiments

After the definition of the process parameters the Box-Behnken design (BBD) - design of experiments (DOE) - was applied, as well as statistical analyses such as Response Surface Methodology (RSM) and Analysis of Variance (ANOVA), in order to determine the combination of optimized process parameters. These statistical methodologies are widely used for the optimization of welding processes since the BBD reduces the number of experiments necessary, compared to methodologies that use full factorials. RSM establishes mathematical models to evaluate the effects of the process parameters in the welded joint property chosen as a response, and ANOVA verifies the adequacy of the developed mathematical model. Statistical analyses were performed using Minitab software [33, 36, 37].

For the analyses, the parameters determined as control variables were: RS, PD, and RF, each one in three levels of values. The fracture load obtained from the lap shear test was determined as the response variable. These control variables and the values of each determined level are shown in table 4.5. Finally, the fifteen parameter combinations resulting from the BBD are represented in table 4.6.

Table 4.5 – Process parameters and values of variation levels for the BBD.

Process Parameters	Values		
	Level -1	**Level 0**	**Level +1**
RS (rpm)	1500	1800	2100
PD (mm)	1.4	1.6	1.8
RF (kN)	7	8	9

Table 4.6 – Process parameters combination according to BBD for process optimization.

Sample	RS (rpm)	PD (mm)	RF (kN)
126	1800	1.6	8
127	1800	1.6	8
128	2100	1.6	7
129	1800	1.8	7
130	2100	1.6	9
131	1500	1.6	7
132	1500	1.8	8
134	1800	1.4	9
135	2100	1.8	8
136	1800	1.4	7
137	1800	1.8	9
138	1500	1.6	9
139	1800	1.6	8
140	1500	1.4	8
141	2100	1.4	8

4.4 LAP SHEAR TESTS

The mechanical behavior of all-welded joints was initially characterized by lap shear tests. Lap shear test will take place in the current work in order to determine the lap shear strength (LSS) of the joints and evaluate the application of the technology in structures, along with microstructural analysis of the shear failure mode. Lap shear tests were carried out in a screw-driven Zwick-Roell 1478 universal tensile machine with a load capacity of 100 kN, at room temperature and with a displacement rate of 2 mm/min. The specimens shown in figure 4.3 are composed of two overlapping sheets with 25.4 mm of overlap length, following the specification of the American Welding Society – AWS

D17.2/D17.2M:2013 Specification for Resistance Welding for Aerospace Applications [53], since there is no specific standard for lap shear testing of refill friction spot welds.

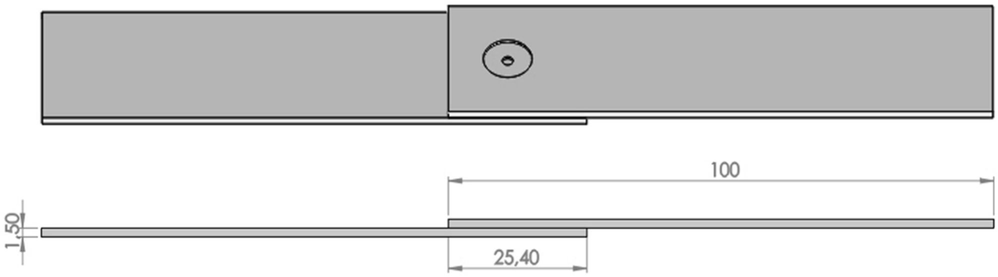

Figure 4.3 – Schematic illustration of the welded specimen for lap shear test and its dimensions in millimeters.

To ensure that the load was applied in the same direction as the center line of the weld spot, an offset of 3 mm between the clamps was applied due to the natural asymmetry of the specimen. The clamping area of the specimen was 25.4 mm x 25.4 mm, resulting in a grip separation of 124 mm approximately.

For the analyses of the shear failure mode of the joint by optical microscopy (OM), the mechanical test was stopped after the maximum force was reached, and a sample was carefully removed and prepared.

4.5 CHARACTERIZATION OF THE OPTIMIZED WELD

4.5.1 Structural Characterization

4.5.1.1 Macro and Microstructural Analyzes

Macro and microstructural analysis were carried out in the cross-section of welded joints in order to evaluate and compare the features of the Refill FSSW process reported in the literature, such as the weld regions: stir zone (SZ), thermomechanically affected zone (TMAZ), heat affected zone (HAZ) and the inherent features of the process, such as the remaining oxide line, hook, lack of refill and porosity [37, 40].

For the OM analyses, the samples were cut, as illustrated in figure 4.4, using a cutting machine Struers Secotom-50. Then, the samples were embedded in a cold-cure transparent resin under pressure Demotec 20 and subsequently subjected to conventional procedures of sample preparation using a Struers Tegramin equipment: grinding with sandpaper disc of 320 mesh with water and polishing on 9 μm and 3 μm diamond suspensions and 0.04 μm silica suspension. The electrolytic etching was carried out with a Barker etchant in a Struers LectroPol-5 using a voltage of 25 V during 170 seconds.

Finally, the macro and micrography were obtained using an optical microscope Leica DM IRM equipped with polarized light and paired with the Leica Application Suite 3.5 software.

For scanning electron microscopy (SEM) analyses, the Philip XL-30 FEG (Field Emission Gun) equipment was used, and the samples were prepared as previously described.

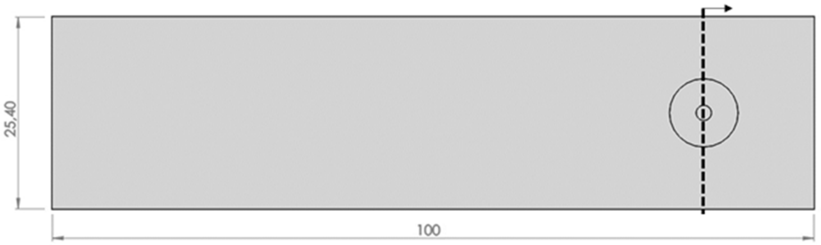

Figure 4.4 – Schematic illustration of the cut region of a welded sample for macro and microstructural analyses (dimensions in millimeters).

4.5.1.1.1 Stop Action Procedure

In order to understand microstructures features formation of the welded region, a stop action procedure was carried out in some samples during the plunging and retracting stages. This procedure consists of stopping the welding procedure in the middle of the process and quenching the sample to enable microstructure analyzes in that determined stage. KHI robot allows the interruption of the process only in the plunging stage at 1.6 mm, as shown in figure 4.5. The preparation and analysis of the samples were done as described above.

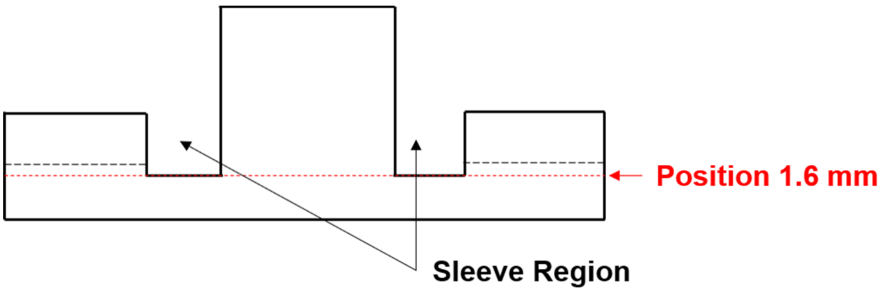

Figure 4.5 – Schematic illustration of the interruption position during the sleeve penetration in the welding process.

4.5.1.2 Microhardness Vickers

Microhardness measurements are useful for the understanding of mechanical and microstructural properties changes along the cross-section of the weld. Thus, a microhardness profile and a microhardness map, a technique that provides a map of colors proportional to the measure microhardness on each point, resulting in an overview of the microhardness variation along the entire cross-section of the weld, were obtained. For the microhardness profile, the indentations were performed in two lines: at a half thickness of the upper and bottom sheets. For the microhardness mapping, the indentations were performed in ten lines. These measurements were performed in a precisely determined area of the cross-section of the samples based on the set of intervals of indentations along the X and Y axis. These microhardness measurements were performed using a Struers DuraScan linked to Ecos Workflow software, the load test applied was 0.2 Kg (200 gf) with an indentation time of 10 seconds, and a distance of 0.25 mm between each.

4.5.1.3 Temperature Measurements

To characterize thermal effects on mechanical properties of the different areas of the weld, temperature measurement was performed to evaluate the maximum temperature reached during the welding procedure in each weld region.

Temperature measurements during the welding process were carried out using three 0.5 mm diameter K-type thermocouples connected to a National

Instruments SCXI data collection system, and to a computer in which the temperature values were recorded at a frequency of 100 Hz through Labview software.

The thermocouples were inserted at the interface of the two sheets through holes in the bottom sheet. The holes were 0.6 mm in diameter and were carefully made at 0, 5 and 7 mm from the center of the weld, positions corresponding to the regions of SZ, TMAZ, and HAZ, respectively. Figure 4.6 shows the schematic illustration of the position of the thermocouples relative to the tool.

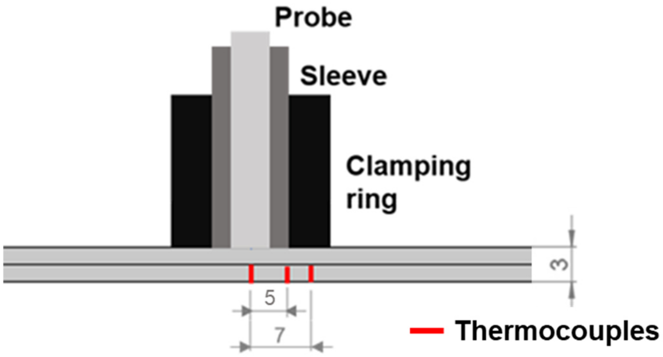

Figure 4.6 – Schematic illustration of the thermocouples approach (dimensions in millimeters).

4.5.1.3.1 Thermal Analysis

To characterize the different precipitation and dissolution reactions in different regions of the welds, differential scanning calorimetry (DSC) analysis were employed with a heat rate of 10°C/s and a maximum temperature of 550°C in a Netzsch Maia DSC200. During the DSC measurement, protective nitrogen gas was used flowing inside the furnace.

The analyzed samples were carefully removed from two regions of the weld and the base material in the as-welded condition. For the greater reproducibility and comparability of the analyzes, all samples had the same geometry: 5 mm diameter and 1 mm thick discs with a weight of 52 mg. Aluminum reference samples with 99.999% purity by the same geometry and weight were used to obtain the baseline correction for each measurement.

Samples were put inside a crucible with a lid before it was taken into the DSC equipment. One sample after solubilization treatment at 540 °C for 1 hour and quenching in water was also analyzed.

In addition, all DSC analyses were immediately performed after preparing the samples, thus avoiding the effect of the aging of the alloy.

4.5.1.4 Bake Hardening Treatment

This project is based on the requirements for the automotive industry. During the automotive assembly, there is a paint bake process, which enables the cure of the painting and increases the strength of AlMgSi alloys due to precipitation hardening. Therefore, bake hardening treatment was carried out to evaluate its influence on the static mechanical behavior of the welds.

The bake hardening consisted of heat treatment at 180 degrees for 30 minutes and was carried out in some samples soon after the welding process in a furnace Nabertherm.

4.5.2 Dynamic Mechanical Properties

4.5.2.1 Fatigue Test

Fatigue behavior was only analyzed for the optimized process condition, which presented the highest values of shear loads. The fatigue tests were performed at room temperature, the equipment used was the hydraulic servo fatigue machine, Schenck Instron. The test specimens used were similar to those shown in Figure 4.3. The load ratio (F_{min}/F_{max}) of R = 0.1 and the frequency of 20 Hz was kept constant for five load conditions: 50, 25, 15, 12.5, and 10% of the maximum load obtained in lap shear tests. In addition, for each level, three replications were performed to have a static analysis. For the samples that did not fail, a stopping criterion of 5×10^6 cycles was used.

4.5.2.1.1 Weibull Distribution and L-N Curves

Fatigue data were statistically analyzed, and L-N curves were obtained using the two-parameter Weibull distribution for each load level. Weibull is the distribution that best describes fatigue behavior, including in low-stress levels, close to the fatigue limit [45, 54].

The probability density function (PDF) for two-parameter Weibull distribution is defined by equation 4.1:

$$f(x) = \frac{\beta}{\alpha}(\frac{x}{\alpha})^{\beta-1} \ e^{-\left(\frac{x}{\alpha}\right)^{\beta}}, \alpha>0, \beta>0 \tag{4.1}$$

where α and β are the characteristic life and Weibull slope, also known as Weibull exponent.

Integrating equation 4.1, the cumulative probability function is obtained, which represents the probability that an element of the population will assume a value less than or equal to a given x, as shown in equation 4.2:

$$F_f(x) = 1 - \ e^{-\left(\frac{x}{\alpha}\right)^{\beta}} \tag{4.2}$$

Since this equation is hardly experimentally determined by not testing the entire population, Bernard`s Median Rank empirical estimator is used and given by equation 4.3:

$$MR = \frac{i-0.3}{n+0.4} \tag{4.3}$$

where i is the experiment number in ascending order and n is the total number of experiments.

The determination of the Weibull parameters α and β is possible by applying the logarithm function twice in equation 4.1, resulting in equation 4.4:

$$lnln\left[\frac{1}{1-f(x)}\right] = \beta \ lnx - \ \beta \ ln\alpha \tag{4.4}$$

Plotting graphs $lnln\left[\frac{1}{1-f(x)}\right]$ x lnx determines β, which is equal to the angular coefficient and α since the linear coefficient is equal to -β $\ln{(\alpha)}$.

Thus, is possible to determine the Mean Time To Failure (MTTF) by equation 4.5:

$$MTTF = \ \alpha\Gamma \ \left(1 + \frac{1}{\beta}\right) \tag{4.5}$$

where Γ is the gamma function.

To evaluate the dispersion between the sets of the load values, the coefficient of variation (CV) is applied using equation 4.6. It represents the ratio between the standard deviation (SD) (equation 4.7) and the MTTF (equation 4.5):

$$CV = \frac{SD}{MTTF} \tag{4.6}$$

where

$$SD = \alpha\sqrt{\Gamma\left(1+\frac{2}{\beta}\right) - \Gamma^2(1+\frac{1}{\beta})} \tag{4.7}$$

To provide the possibility of prediction of fatigue life according to the level needed by the engineering project, L-N plots will be drawn for three different reliability levels such as 10%, 50%, and 99%. The equation 4.8 will be used to obtain the values of life (N) for different reliability levels.

$$N_{Rx} = \alpha(-\ln(Rx))^{-1/\beta} \tag{4.8}$$

in which N_{Rx} is the value of fatigue life of the welded samples for a reliability level of Rx% [45, 55].

4.5.2.1.2 Fracture Analysis

The fracture surface of fatigue samples was evaluated by SEM using an XL30 FEG Phillips microscope available at the Laboratory of Structural Characterization (LCE) of DEMa/UFSCar. Samples under low-cycle and high-cycle load were analyzed.

5 RESULTS AND DISCUSSIONS

5.1 PARAMETER OPTIMIZATION FOR LOAD-CONTROLLED PROCESS

The fifteen resultants welding parameters (rotational speed (RS), plunge depth (PD), and retracting force (RF)) combinations given by Minitab software, shown in table 4.6, are produced using the load-controlled Refill FSSW system. After the results from lap shear tests (Table A of the appendix) was possible to obtain in Minitab software using polynomial regression, the lap shear strength (LSS) model, given by equation 5.1. This model presented good reliability in fitting experimental results since $R^2 = 83.9\%$.

$$\mathbf{LSS\ (kN) =} -67.2 + 0.0096*\mathbf{RS} + 13.92*\mathbf{RF} + 7.7*\mathbf{PD} - 0.000002*\mathbf{RS}*\mathbf{RS} - 0.943*\mathbf{RF}*\mathbf{RF} - 2.96*\mathbf{PD}*\mathbf{PD} + 0.000283*\mathbf{RS}*\mathbf{RF} - 0.00333*\mathbf{RS}*\mathbf{PD} + 0.80*\mathbf{RF}*\mathbf{PD} \qquad (5.1)$$

Through response surface analyses and contour plots, figure 5.1, obtained by equation 5.1, it was observed that the optimized process parameters values could be in regions out of the initial experimental range. According to these results, additional experiments were performed, and the maximum LSS would have been reached in parameters combinations with lower tool RS. To reach the optimized process parameters values, the initial processing window was expanded, as shown in table 5.1, and further experiments were performed (complete data in Table B of the appendix). Therefore, a new regression model was determined, as shown in equation 5.2.

Table 5.1 – Process parameters limits after additional tests.

Process Parameters	**Values**	
	Min	**Max**
RS (rpm)	750	2100
PD (mm)	1.2	1.8
RF (kN)	7	10

$$\mathbf{LSS\ (kN) =} -94{,}4 + 0{,}01687*\mathbf{RS} + 16{,}60*\mathbf{RF} + 18{,}58*\mathbf{PD} - 0{,}000001*\mathbf{RS}*\mathbf{RS} - 0{,}757*\mathbf{RF}*\mathbf{RF} - 1{,}24*\mathbf{PD}*\mathbf{PD} - 0{,}001053*\mathbf{RS}*\mathbf{RF} - 0{,}00371*\mathbf{RS}*\mathbf{PD} - 1{,}099*\mathbf{RF}*\mathbf{PD} \qquad (5.2)$$

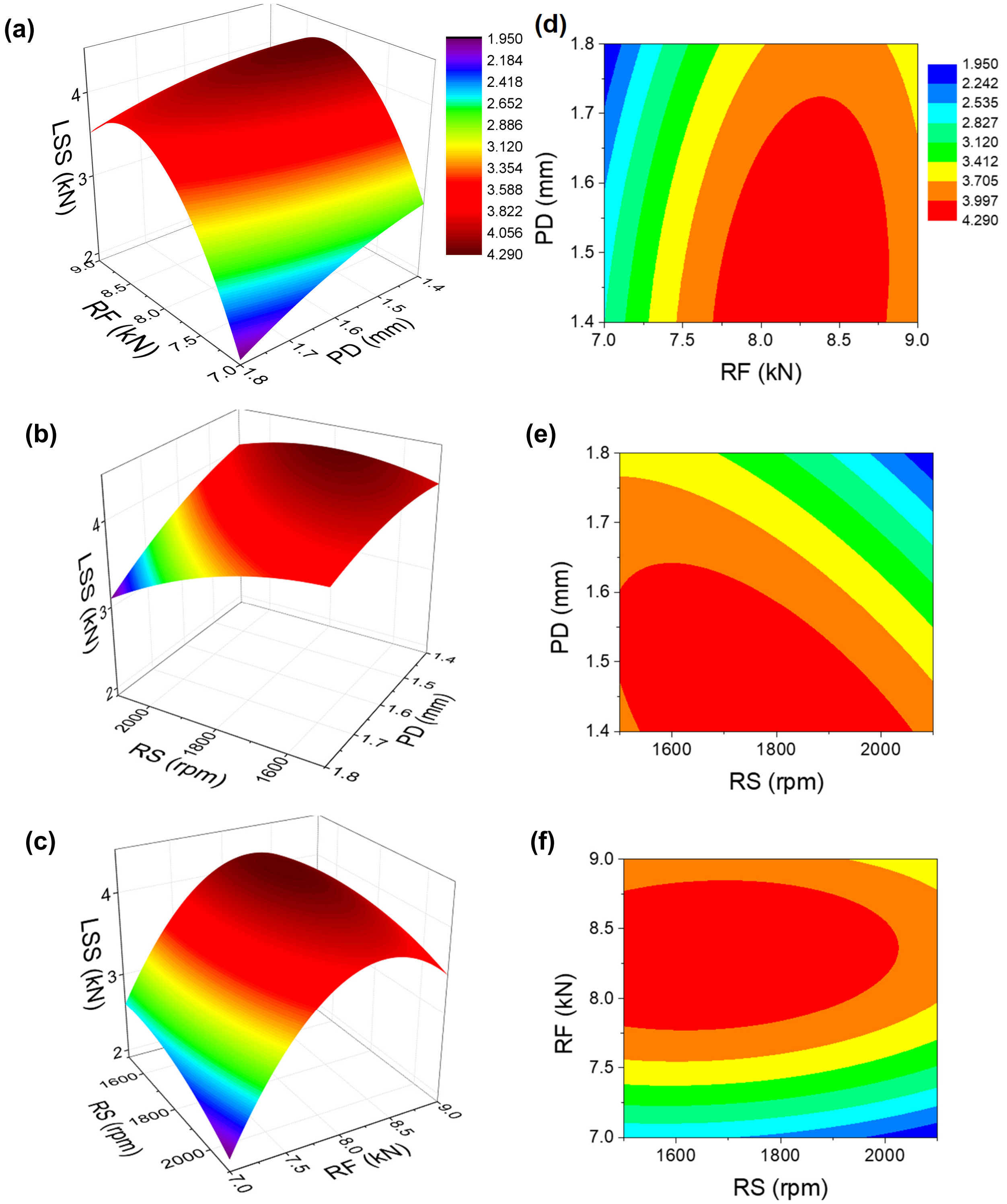

Figure 5.1 – Response surfaces (a) PDxRF, (b) RSxPD, (c) RSxRF and contour plots, (d) PDxRF, (e) RSxPD, (f) RSxRF from the lap shear tests obtained by the Box Behnken design.

According to equation 5.2 new response surfaces were obtained, as shown in figure 5.2.

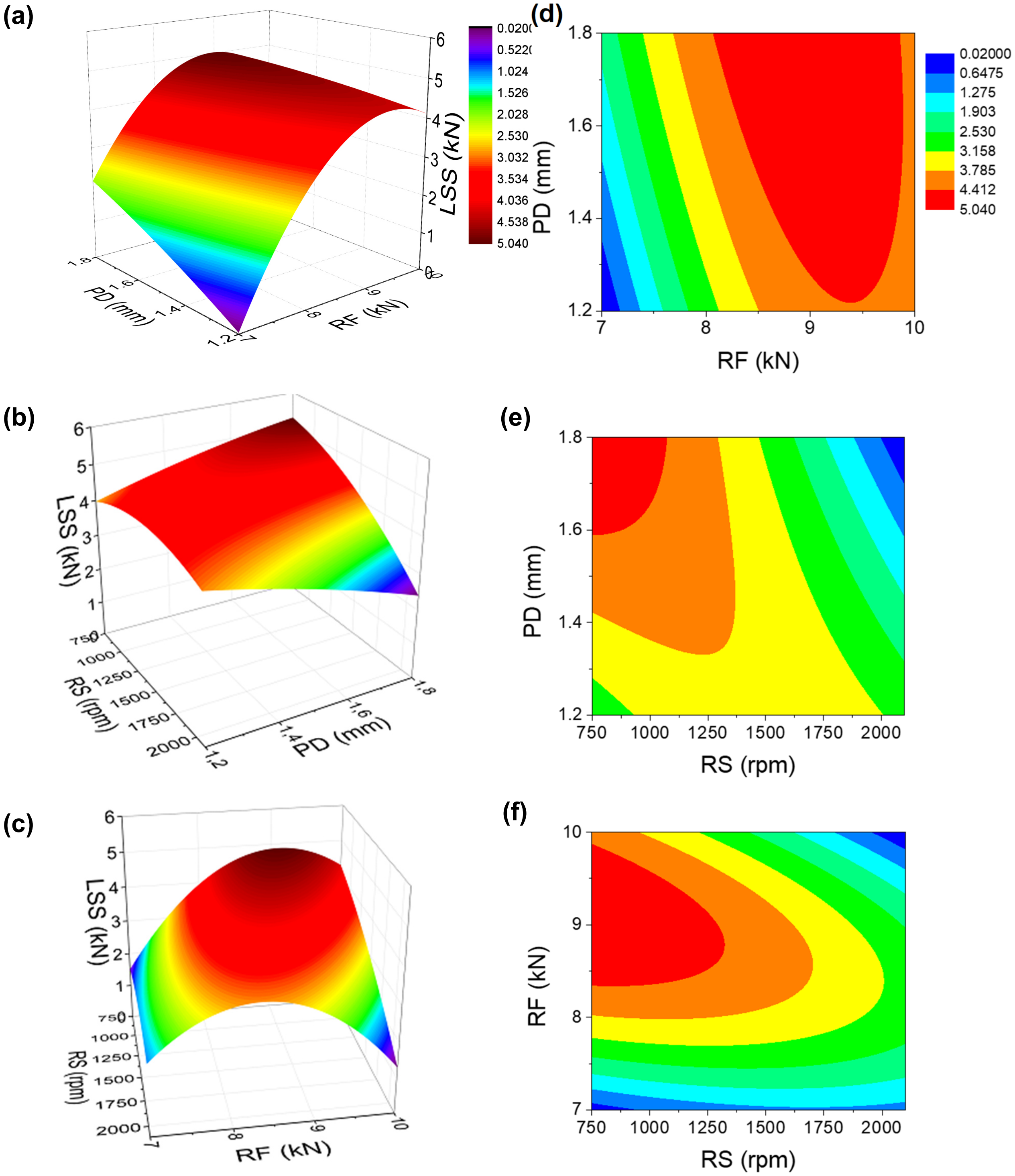

Figure 5.2 – Response surfaces (a) PDxRF, (b) RSxPD, (c) RSxRF and contour plots, (d) PDxRF, (e) RSxPD, (f) RSxRF from the lap shear tests obtained after additional tests.

The shear strength model reliability was increased to $R^2 = 87.5\%$ and all process parameters presented an optimized value. The maximum shear strength average obtained was 4.84 ± 0.06 kN and was achieved by applying the following process parameters set: RS = 1000 rpm, PD = 1.6 mm, and RF = 9 kN.

Combinations of process parameters involving values above 1.8 mm for PD and below 750 rpm for RS, as suggested by the new contour plots (figure 5.2 (d), (e) and (f)), were evaluated. However, those combinations produced defective welds. Thus, these parameters values were not considered in the optimization of the process parameters.

Analysis of variance (ANOVA) of factors – RS, RF, and PD – indicates the effect of individual parameters on the LSS performance of the welds. Table 5.2 indicates the outputs of the analysis with the influence of each parameter on LSS value. These results point to terms of RF and RS being the ultimate influence factors on LSS, considering a confidence level of 95% ($p\text{-value} \leq 0.05$).

Table 5.2 – Analysis of variance (ANOVA) for the lap shear strength model.

Source	**Degrees of Freedom**	**Sum of squares**	**Mean square**	**F-value**	**P-value**
MODEL	9	40.73	4.53	33.47	0.000
RS	1	1.45	1.45	10.75	0.002
RF	1	7.02	7.02	51.89	0.000
PD	1	0.03	0.03	0.25	0.623
RS^2	1	0.63	0.63	4.68	0.036
RF^2	1	7.23	7.24	53.52	0.000
PD^2	1	0.07	0.07	0.53	0.471
RSxRF	1	1.66	1.66	12.25	0.001
RSxPD	1	1.72	1.71	12.69	0.001
RFxPD	1	0.64	0.64	4.71	0.036
Error	43	5.81	0.13		

The LSS average results for the optimized process parameters set, equal to 4.84 ± 0.06 kN, is higher than the shear load requirements for spot weld, since the AWS D17.2/D17.2M:2013 [53], the standard used as a reference, establishes an LSS minimum average equal to 3.4 kN for this aluminum alloy and sheet thickness, as observed in figure 5.3, which presents the force *versus* displacement curve from the lap shear test of a weld produced by the load-controlled method.

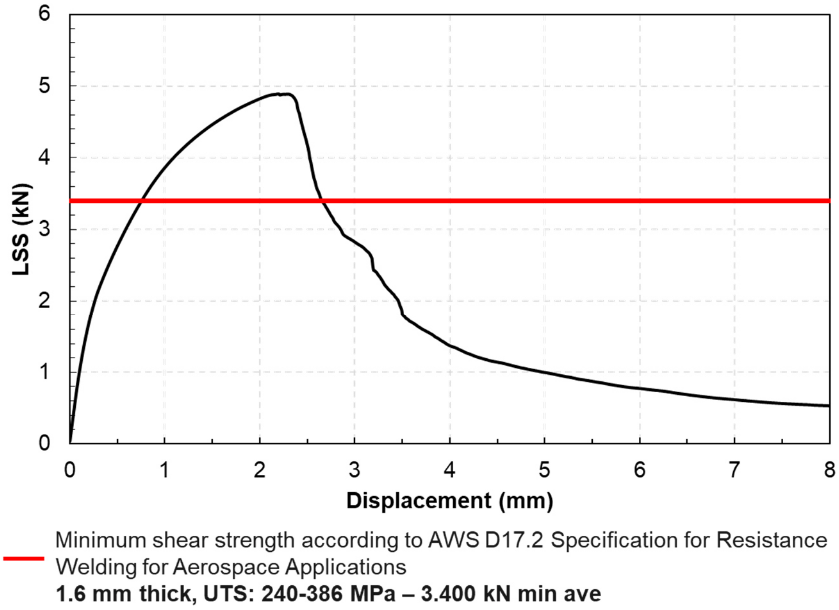

Figure 5.3 – LSS *versus* displacement graph of lap shear test of a sample performed through the load-controlled Refill FSSW process.

Furthermore, in comparison with the LSS observed in the samples performed using the optimized process parameters defined in a previous study (table 4.3), by the traditional position-controlled system, the values could be considered statistically identical since it was on average equal to 4.82 ± 0.22 kN. Table 5.3 summarizes the welding parameters and the LSS acquired for the load- and position-controlled process.

Table 5.3 – Welding parameters and LSS of the load- and position-controlled process.

	Load control	**Position control**
Rotational speed (rpm)	1000	2100
Plunge depth (mm)	1.6	1.6
Lap shear strength (kN)	4.84 ± 0.06	4.82 ± 0.22

To produce the highest LSS in both systems, the position-controlled machine required a higher tool rotational speed (2100 rpm) within the established welding time (1.1 s). The higher rotational speed produces higher stirring of the material facilitating the sleeve to reach the plunge depth in the defined welding time. On the other hand, the load-controlled process required a lower tool rotational speed (1000 rpm) to generate heat and plasticize the material, enabling the sleeve plunge until the defined plunge depth. In this case, once the load applied in the tool is defined instead of the welding time, a longer welding time (2.3 s) was need to produce the weld.

To illustrate the load control in the process performed by the KHI robot, figure 5.4 shows the measured forces recorded during the welding process.

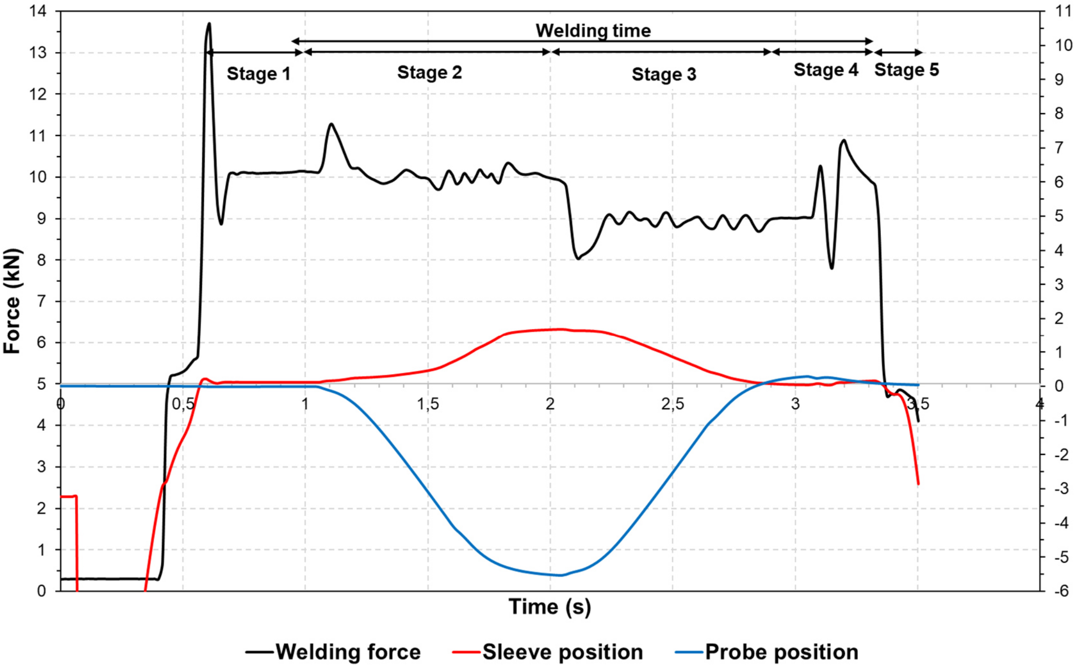

Figure 5.4 – Welding force graph of the load-controlled Refill FSSW process during the optimized-parameter performance, with a load of 10 kN during the sleeve plunging stage and 9 kN in the sleeve retracting stage, and a sleeve plunge depth of 1.6 mm.

The defined load does not change throughout the load-controlled welding process stages, and the defined load limit (in this optimized case defined as 10 kN to the sleeve plunging stage and 9kN to the sleeve retracting stage) is not overpassed. During the sleeve plunging stage, and probe retraction (second stage of the process) the plunge load acting in the tool is constant and equal to 10 kN, and in the sleeve retracting, and probe plunging (third stage of the process), this load is constant and equal to 9 kN.

5.2 STRUCTURAL CHARACTERIZATION

5.2.1 Macro and Microstructural Analysis

The typical cross-section macrograph of the welded joint performed by the load-controlled process under the optimized process parameters is shown in figure 5.5 (A).

No defects associated with the material flow, such as lack of refill, lack of mixing, or thickness reduction, were observed in the weld area. The load-controlled weld of the AA6016-T4 produces welds with the same typical regions (or zones) found in welds produced by position-controlled Refill FSSW process i.e., Stir Zone (SZ), Thermo-mechanically Affected Zone (TMAZ) and Heat Affected Zone (HAZ), in addition to the Base Material (BM) [34, 36, 40].

The SZ, located in the center of the weld, composes material subjected to high strain rates and high temperatures due to the tool stirring contact. This region presents a dynamic recrystallized structure composed of fine and equiaxial grains, with an average diameter of 10 µm, estimated by the intercept method [64], as presented in figure 5.5 (B).

The TMAZ showed in figure 5.5 (C) undergoes moderate strain rates and temperatures, leading to elongated and deformed grains. This region does not experience dynamic recrystallization since the strain rate is not enough to induce this phenomenon. HAZ corresponds to the region between TMAZ and BM, which does not experience plastic deformation while is affected by the thermal cycle. In this case, the grain size of the HAZ is the same as the unaffected BM, as is shown in figure 5.5 (C) and 5.5 (F). The HAZ extension is commonly identified through hardness measurement due to the alteration in the mechanical properties. Finally, BM is not affected by the welding process.

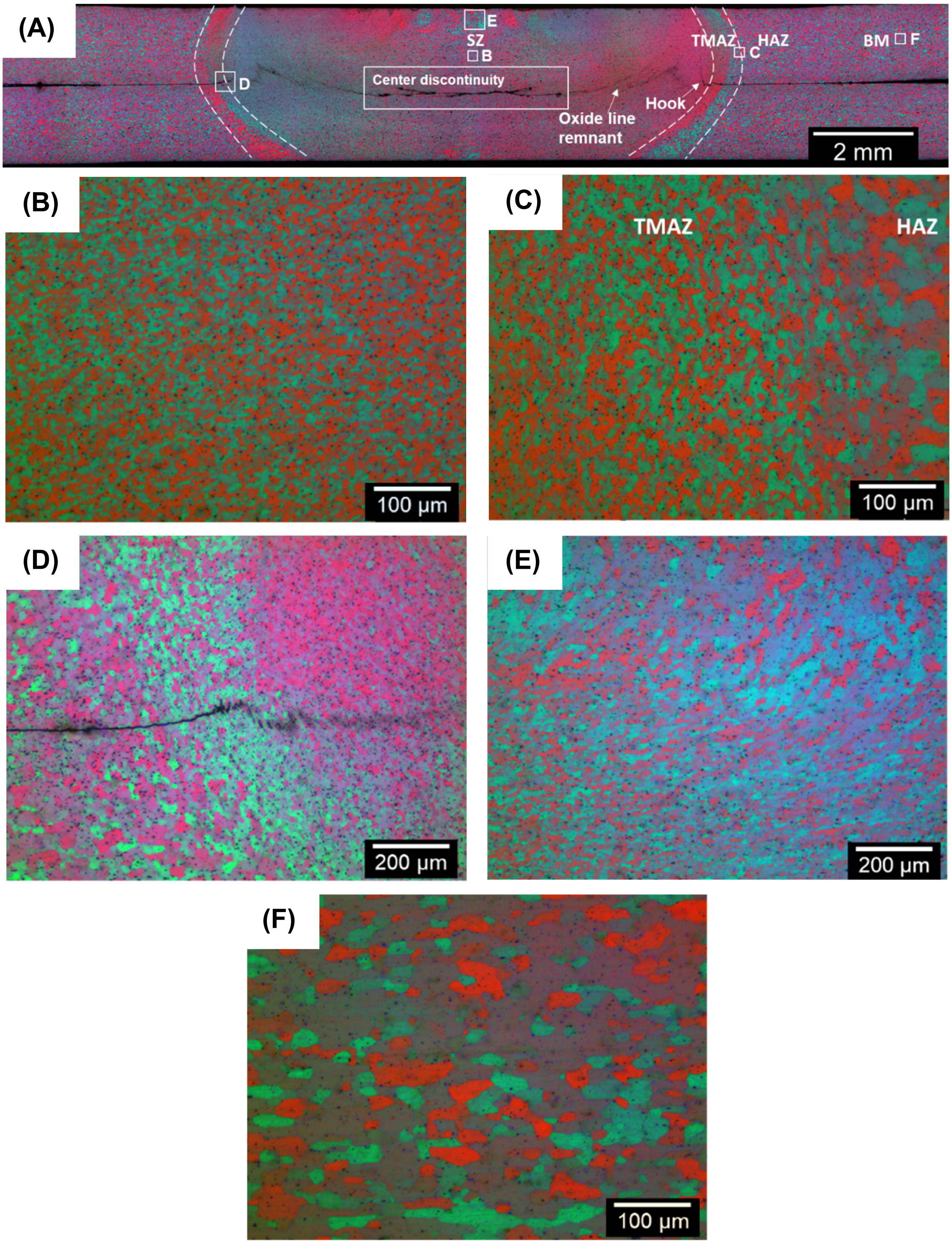
(A)
E
SZ
B
TMAZ
HAZ
C
BM
F
D
Center discontinuity
Oxide line remnant
Hook
2 mm
(B)
100 µm
(C)
TMAZ
HAZ
100 µm
(D)
200 µm
(E)
200 µm
(F)
100 µm

Figure 5.5 – Macrograph and details by optical microscopy of the cross-section of the welded joint performed by the load-controlled process. (A) Macrograph showing the different zones and features such as hook feature and bonding ligament; (B) microstructure of SZ; (C) microstructure of TMAZ and HAZ; (D) hook feature; (E) grain structure in the central top of SZ and (F) base material.

Geometrical and metallurgical features such as hook and oxide line remnant were observed in cross-section of the weld produced by the load-controlled process, as identified in figure 5.5 (A). Figure 5.5 (D) shows the hook feature in high magnification. It is formed at the transition region between the unwelded and the fully welded region in the joint and is inherent to the process.

By observing the oxide line remnant, it is possible to infer material flow in the interface between the sheets, which is symmetric about the weld center and has an arc-shape in the center and zigzag in the edge in agreement to Rosendo et al. [34], as discussed in section 3.2.2.

The microstructural features resulted from the load-controlled Refill FSSW process can be compared to the cross-section macrograph of the weld produced by the position-controlled process using the optimized welding parameters (figure 5.6).

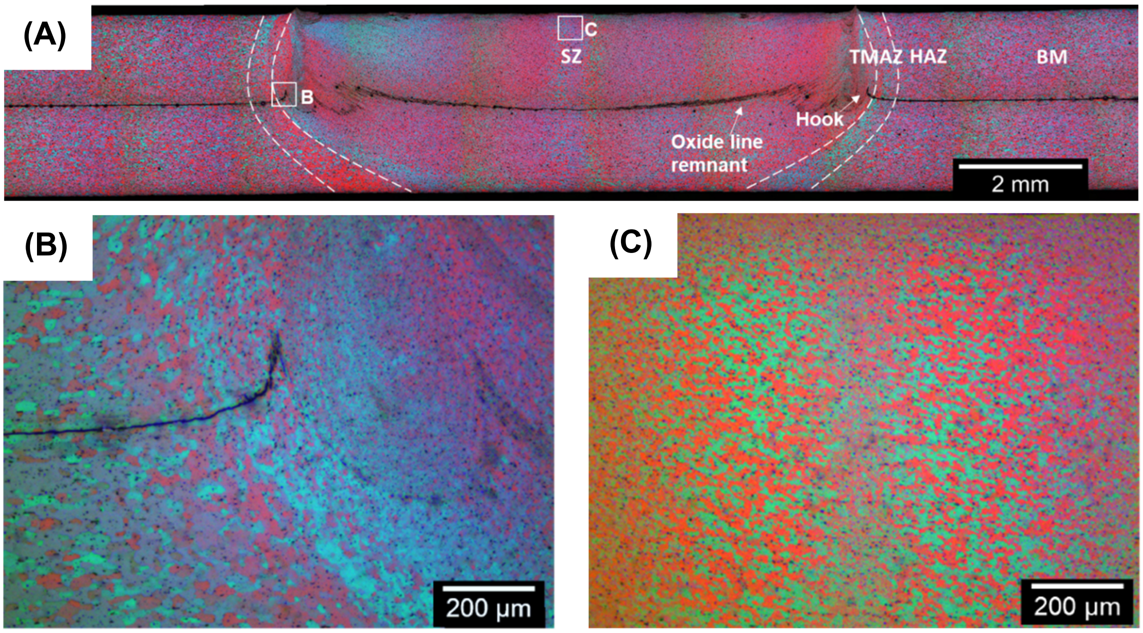

Figure 5.6 – Macrograph and details by optical microscopy of the cross-section of the welded joint performed by the position-controlled process. (A) Macrograph showing the different zones and features such as hook and bonding ligament; (B) detail of the hook and (C) detail of the grain structure in the center top of the SZ.

Figure 5.6 (A) shows the macrostructural of the joint in which the typical weld regions (SZ, TMAZ, and HAZ) are observed, in addition to the BM. The hook tip points up, as shown in high magnification in figure 5.6 (B), and the oxide line remnant was also revealed, and no defects were observed in the weld area.

Thus, in terms of microstructural features, the main differences of the welds produced by the load-controlled process when compared to those produced by the position-controlled process are the presence of a central discontinuity in the oxide line remnant (figure 5.5 (A)) and the flat shape of the hook tip, common to all joints performed by the load-controlled process. It is worth noting that it is possible to produce this hook tip flat shape using the position-controlled process through welding parameter adjustment, as reported by Silva et al. [62] on their work with similar AA6082-T6 Refill FSSW joints.

In addition, it is also worth mentioning that it is possible to produce defect-free welds (without central discontinuity) through the load-controlled process, as presented in figure 5.7. For that, another process parameter set should be applied, for example: RS = 1800 rpm, PF= 10 kN, RF = 9 kN, and PD = 1.4 mm. However, such a welded joint did not lead to an optimized LSS value. Thus, no further analyses were carried out in this defect-free joint. Instead, this work focused on analyzing the welds with optimized LSS values regardless of the presence of the central discontinuity.

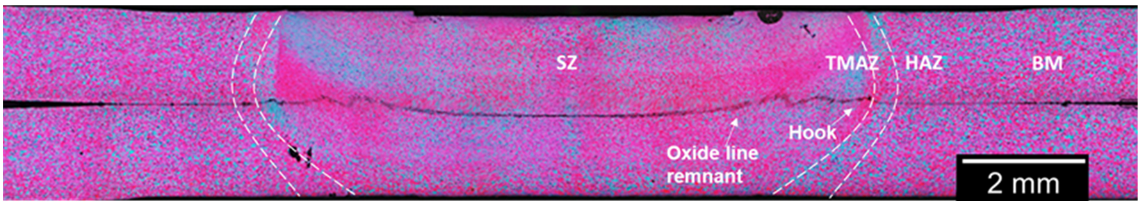

Figure 5.7 – Macrograph by optical microscopy of the cross-section of the defect-free welded joint performed by the load-controlled process.

Figure 5.8 presents SEM images of the un-etched cross-section of the optimized welded joint performed by the load-controlled process.

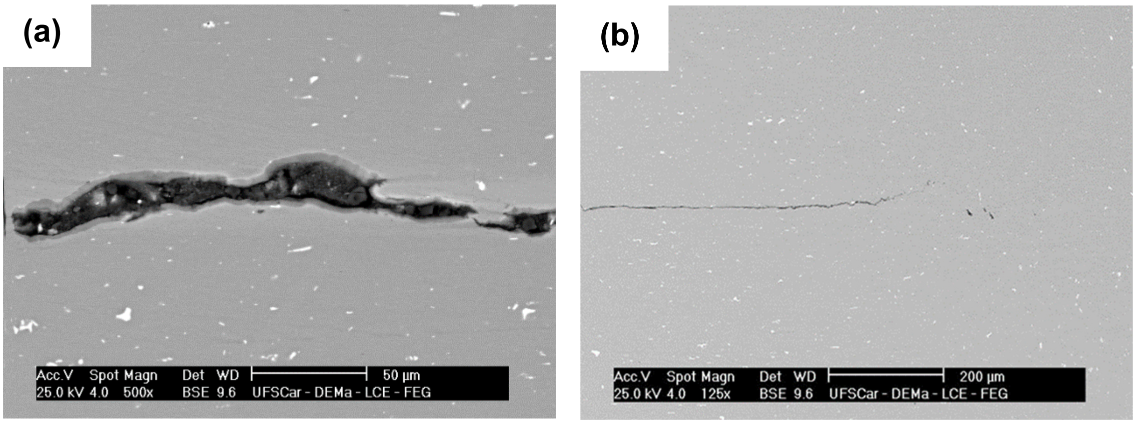
(a)
Acc.V Spot Magn Det WD 50 µm
25.0 kV 4.0 500x BSE 9.6 UFSCar - DEMa - LCE - FEG
(b)
Acc.V Spot Magn Det WD 200 µm
25.0 kV 4.0 125x BSE 9.6 UFSCar - DEMa - LCE - FEG

Figure 5.8 – Backscattered electron mode (BSE) SEM images of the non-etched cross-section of the welded joint performed by the load-controlled process using the optimized process parameters. (a) Detail of the center discontinuity and (b) Detail of the flat shape of the hook tip.

It is possible to observe the main differences mentioned above, such as details of the center discontinuity (figure 5.8 (a)), and the flat shape of the hook tip (figure 5.8 (b)). Besides, another difference between the weld produced by the two systems is related to the grain uniformity in the SZ. The welds performed through the position-controlled process has an SZ composed of uniform fine and equiaxial grains, see figure 5.6 (C), while the welds performed through the load-controlled process presents a non-uniform grain structure in the top region of the SZ, in which the grains are larger, deformed and elongated (see figure 5.5 (E)).

These differences in the microstructures of the SZ might be related to the tool characteristics used in the load- and position-controlled systems. The anti-sticking coating of the tool used in the load-controlled process should be the major influent factor since it provides a different contact and flow between the tool and the softened metal. Another factor that may cause such structural differences is the thread of the tool used in the position-controlled machine. The thread causes a high mix of material and a different material flow providing uniform grains in the entire SZ, as well as a sound central region. The hook, as mentioned before, refers to the partially metallurgical bonded region, a transitional zone between the completely welded regions and unwelded ones.

The differences in their tip shape should be related to the process parameters as well as the material flow from each welding system in accordance with Cao et al. [50], who reported that the hook shape or appearance is affected by the welding parameters such as rotational speed, welding time and plunge depth, and it is also a result of material flow during the second and third stages. Furthermore, Silva et al. [65] reported that the plunge depth of the sleeve determines the hook tip shape through material flow around the sleeve.

5.2.2 Stop Action Procedure

In this work, the microstructure features formation was studied by a stop-action procedure, which was applied for the second stage of the process from both welding control systems, as presented in figure 5.9 (A) and figure 5.9 (B). These macrographs provide insights into the material flow during the second stage of the welding process performed under the optimized process parameters. It is possible to observe that the hook profile was already defined in the second stage, with a flat tip for the load-controlled process (figure 5.9 (C)), and with a tip points up for the position-controlled one (figure 5.9 (D)). These different shapes might be strongly related to the tool designs used in each process system since they provide different material flow. The threaded sleeve used in the position-controlled system plays an important role in the hook tip shape pointing up due to the high mix of material and the different contact with the softened metal when compared with those provided by the anti-sticking coating tool used in the load-controlled process. Silva et al. [65] reported that during the plunging stage, the material flow around the threaded sleeve bends the interface between the sheets in the upward direction. Their study was performed for plunge depth at 0.1 mm below the interface between the two aluminum sheets as in the present work.

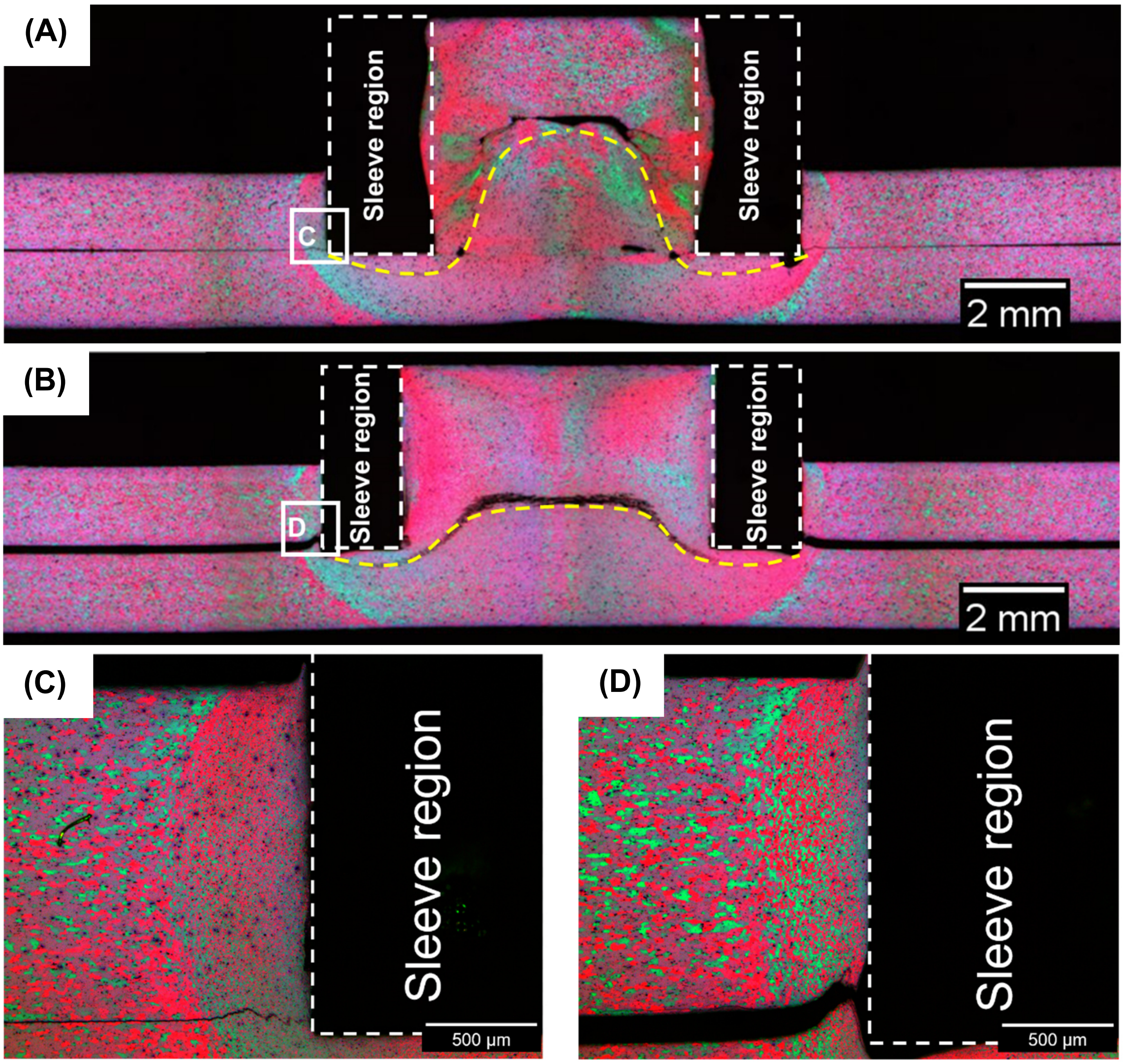
(A)
Sleeve region
Sleeve region
C
2 mm
(B)
Sleeve region
Sleeve region
D
2 mm
(C)
Sleeve region
500 µm
(D)
Sleeve region
500 µm

Figure 5.9 – Macrograph by optical microscopy of the cross-section of the samples obtained through the stop action procedure during the second stage of the (A) load-controlled; (B) position-controlled welding process with a sleeve plunge of 1.6 mm; (C) detail of the flat shape of the hook tip and (D) detail of hook tip points up.

During the second stage, the plasticized material from the bottom sheet was extruded into the top plate, and the original interface gets an inverted “V” shape in the weld, see yellow dashes in figure 5.9. The distinctive "V" shape observed in the samples performed by the load- and position-controlled systems are due to the different probe sizes used to perform the welds in the two machines. As the probe used in the load-controlled system is smaller than the one used in the position-controlled system, the space provided by the probe retraction to admit the volume of material displaced by the sleeve is different. Thus, the interface goes higher within the space provided by the retracted probe in the load-controlled process. Cao et al. [50] who studied hook formation of Refill FSSW in alloy 6061-T6 reported that the edges of the inverted “V” shaped interface was pushed sideways and upward whereas its center was pushed downward by the probe, thereby forming a kind of hook profile point up.

Meanwhile, the central discontinuity and the non-uniform grains can already be observed in the second stage of the load-controlled process. In this stage, the probe is retracted slightly higher than the position to create constant volume produced by sleeve and probe during sleeve plunging to avoid disturbance of the load acting in the sleeve. The volume of the cavity left by the probe retraction is slightly larger than the extruded material squeezed by the sleeve plunges. It means there is no intense contact between the probe tips with the extruded material leading to an empty place in the center of the weld. The flat surface of the extruded material, observed in the probe area in figure 5.9 (A), as well as the bulging appearance, is due to the removal process of the extruded material from inside the sleeve by pushing the probe against the extruded material after the spot action procedure. The last stage of the process is not able to close completely the central discontinuity, and non-uniformity of the grains remains in the top center of the SZ, as previously observed.

On the other hand, the position-controlled process provides a uniform grain structure and no voids since the beginning of the process. In the position-controlled process, a constant volume is maintained during probe and sleeve axial movement, meaning the probe tip has contact with the plasticized material throughout the entire welding process.

5.3 STATIC MECHANICAL PROPERTIES

5.3.1 Microhardness Vickers

Figure 5.10 shows a typical microhardness distribution of the mid-thickness of the upper and lower sheets of the cross-section of a sample performed by the load-controlled Refill FSSW process. Overall, the hardness profile across the top plate presets a “W” shaped appearance with a noted decrease in the hardness value in the TMAZ until a minimum in the HAZ. The SZ shows a relatively constant hardness of 62 $HV_{0.2}$ on average, and in the TMAZ the hardness values decrease until a minimum of 51 $HV_{0.2}$ at the HAZ. The HAZ ends at approximately 9.5 mm from the weld center, where the hardness value reaches the average of the BM hardness value (61 $HV_{0.2}$). The hardness profile of the bottom plate presents a relatively constant hardness of 58 $HV_{0.2}$ on average, which could be related to the non-existence of all the welding zones characteristic in the bottom plate since there has been no significant increase or decrease in local properties.

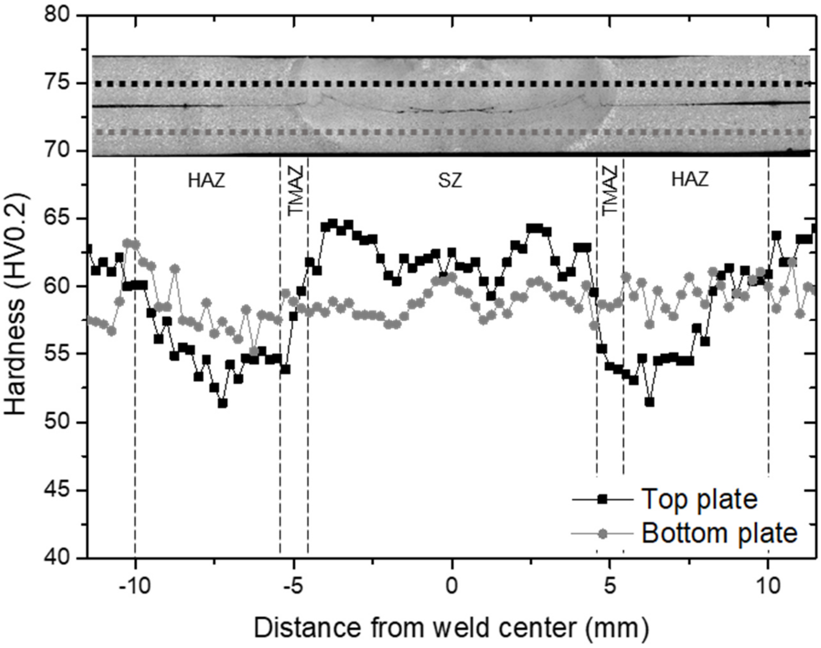

Figure 5.10 – Microhardness profile measured in the mid-thickness of the upper (black square) and bottom sheet (gray circle) of the cross-section of load-controlled Refill FSSW joint.

The different microstructural zones along with the specimen due to a combination of heat and strain rate related to the tool movement can also be inferred by hardness measurements since these thermal and mechanical inputs affect the original state and distribution of the precipitates.

As a precipitation-hardenable aluminum alloy, AA6016-T4 has its mechanical properties mainly determined by the volume fraction, size, and distribution of strengthening precipitates [43, 66, 67]. Accordingly, the low hardness value in HAZ can be attributed to the precipitate coarsening at the intermediate temperature (312°C) reached during the welding process [50]. In the TMAZ and SZ, the strengthening precipitates can be subjected to coarsening and solubilization since these zones are undergo severe plastic deformation and higher temperatures (431°C and 447°C, respectively). The coarsening has shown to be the predominant phenomenon responsible for the hardness changes in the TMAZ. The main reason for the hardness increases in SZ must be related to the solubilization of precipitates and their re-precipitation due to the dynamic recrystallization observed in this zone. Moreover, the grain size reduction contributes favorably to the strengthening of the material in this zone [34]. Through the hardness map shown in figure 5.11 is possible to observe the hardness variation over the entire weld cross-section. It is shown that the hardness increases in the SZ and decreases in the TMAZ and HAZ.

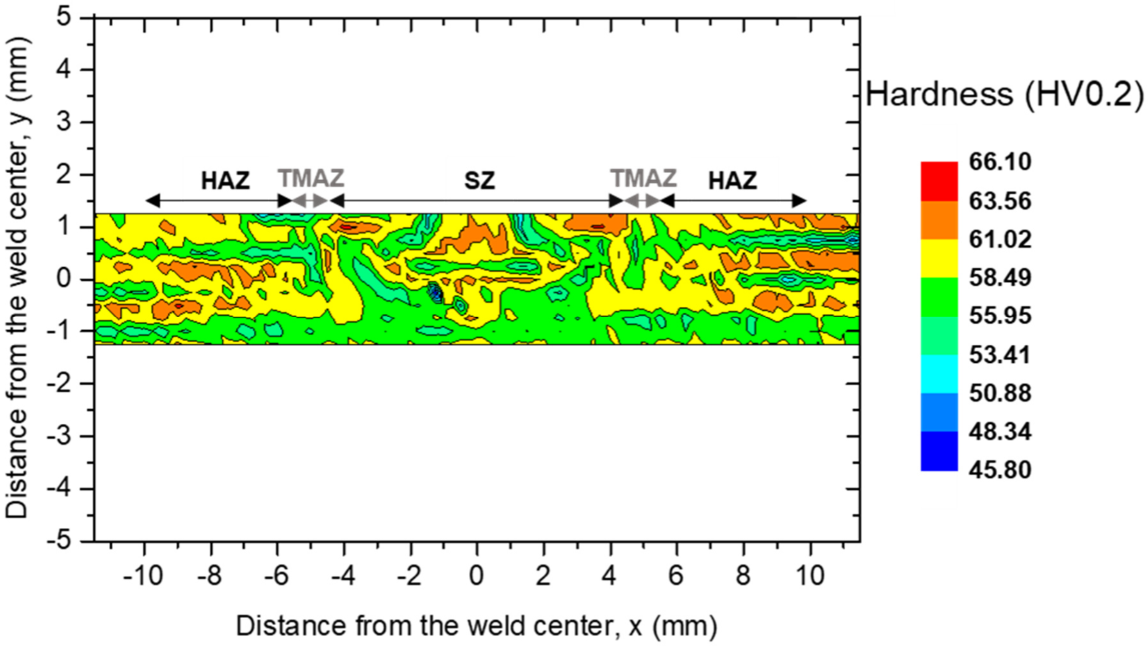

Figure 5.11 – Hardness map measured in the entire cross-section of the load-controlled Refill FSSW joint.

In comparison to the weld produced by the position-controlled system (figure 5.12), the microhardness profile shows a similar behavior, despite the higher hardness values in the HAZ for the top plate. The SZ shows a relatively constant hardness of 64 $HV_{0.2}$. In the TMAZ, the hardness decreases to a minimum equal to 59 $HV_{0.2}$ at the interface between TMAZ and HAZ. Finally, as observed for the sample performed by the load-controlled process (figure 5.10), the HAZ ends at approximately 9.5 mm from the weld center, where the hardness value reaches the average of the BM hardness value. The bottom plate shows a relatively constant hardness of 58 $HV_{0.2}$ on average.

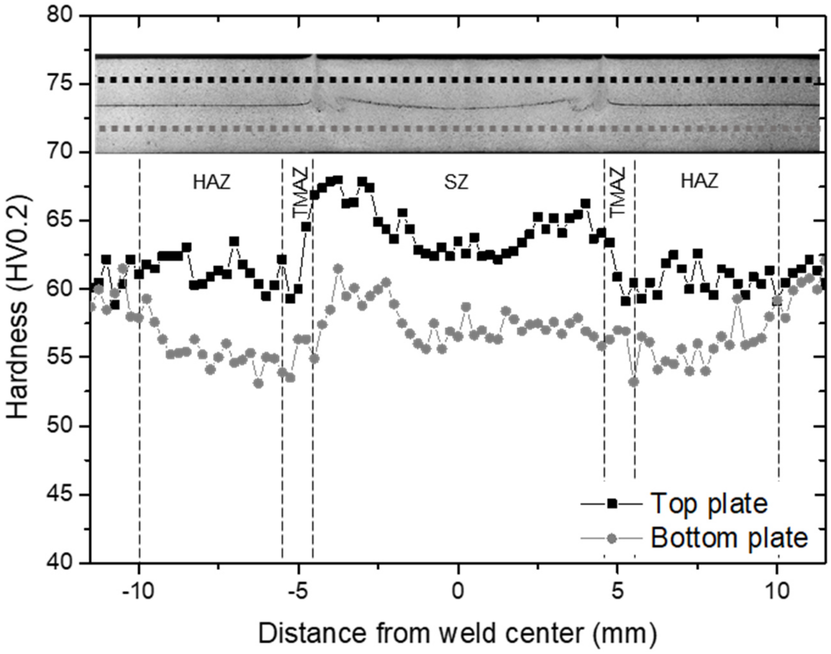

Figure 5.12 – Microhardness profile measured in the mid-thickness of the upper (black square) and bottom sheet (gray circle) of the cross-section of position-controlled Refill FSSW joint.

The difference in the TMAZ hardness values from both systems can be attributed to the difference in the material flow caused by the threads in the tool used in the position-controlled system. The threads lead to a high deformation level in the TMAZ, producing a high strain hardening in this region, which is not suppressed equally by the softening caused by the precipitation coarsening. In addition, the peak temperatures measured during the position-controlled Refill

FSSW process were lower of about 405 °C, 334 °C and 283 °C at the SZ, TMAZ and HAZ, respectively. Lower peak temperature in the measured positions lead to different precipitate evolution, accordingly, influencing the hardness measurements as well. Further investigation needs to be carried out to understand the difference of the peak temperature and their influences in both controls.

5.3.2 Fracture mode analysis

Figure 5.13 shows a Backer-etched cross-section of a weld sample produced by the load-controlled process after an interrupted shear test. The fracture mode observed were pull-out, which was observed in all samples tested in this study. This fracture mode is one of the two typical fracture modes observed during lap shear loads in aluminum sheets joints performed by Refill FSSW, in addition to the through the welding mode, as reported by de Castro et al. [40].

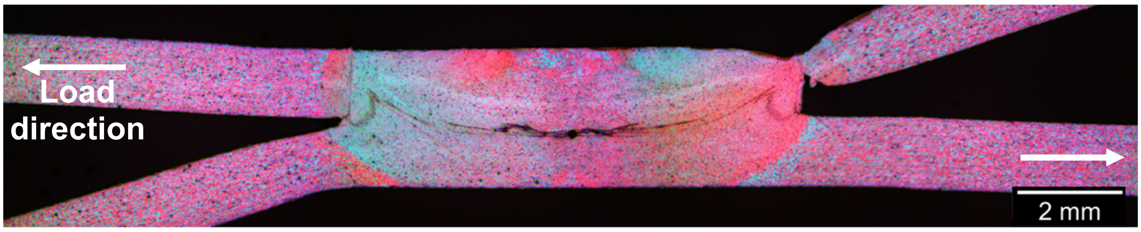

Figure 5.13 - Macrograph by optical microscopy of the cross-section of a sample obtained by interrupting the shear test.

The pull-out failure is associated with the circumferential crack around the spot weld, a region characterized by a change of hardness as observed in the hardness map (figure 5.11), more specifically in the TMAZ [51]. Complete separation of the spot weld from the upper sheet occurs, leaving a circular hole on it. The same behavior is noticed in the welds produced by the position-controlled process, which has a similar hardness profile as the ones produced by the load-controlled process. In figure 5.14 are shown in high magnification the weld region in which the fracture propagation occurs, before (figure 5.14 (a)) and after the lap shear test (figure 5.14 (b)).

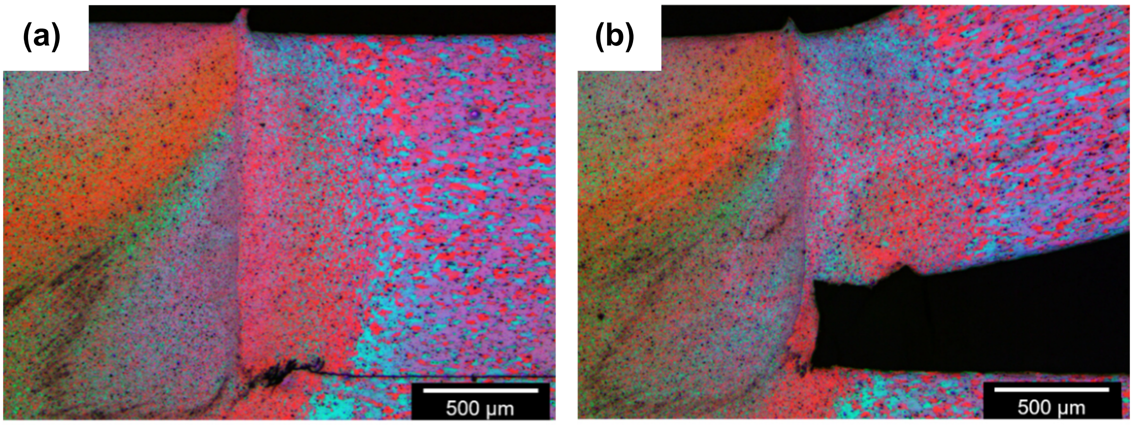

Figure 5.14 – Microstructure by optical microscopy of the cross-section of the welded joint performed by the load-controlled process (a) before and (b) after the lap shear test, illustrating the pull-out failure.

Therefore, it is possible to affirm that the mechanical strength of the joints under shear load is controlled by the softer region of the weld in the TMAZ region, which is the same regardless of the process used. The microstructural features such as hook and discontinuities in the bonding ligament, which are the main differences between both welding control modes, seems to not affect the mechanical properties of the welds. Thus, the load-controlled Refill FSSW welding process is a suitable technique to produce spot welds in aluminum sheets with the advantage of subjecting the welding tools to controlled loads. This may have a huge impact on the lifetime of the welding tools, which is one of the main challenges that must be overcome for implantation of Refill FSSW in vehicle production lines [68].

5.4 THERMAL ANALYSIS

5.4.1 Temperature Measurements

During the welding process, deformation and frictional heat produce microstructural changes regarding the original state, amount, and distribution of the precipitates present in the material. Considering the AA6016 alloy, the fraction of GP zones, β’’, β’ and β phases can be altered. In the case of the AA6016-T4 alloy, the volume of GP zones must be higher than the other precipitated phases because of the T4 heat treatment [15, 69, 70]. The volume of β” precipitate in the AlMgSi alloys is responsible for the maximum peak of hardness. These precipitates are formed during artificial aging as the T6 heat treatment [71].

Therefore, it is expected that thermal and mechanical inputs during the welding process will cause the GP zones to transform into the β” phase, precipitates coarsening or complete precipitates dissolution [43]. The characterization of the thermal profile in the welded regions is the first step to identify which precipitation and dissolution process occurs during the welding process.

Thus, figure 5.15 shows the temperature measurements in the SZ and HAZ. The maximum temperature of the SZ region was approximately 450 ºC. It is worth remembering that the SZ is subjected to high strain levels, which also contribute to the dissolution process in this region. The maximum temperature reached in the HAZ region was approximately 310 °C, which might have resulted in precipitate coarsening [43, 45].

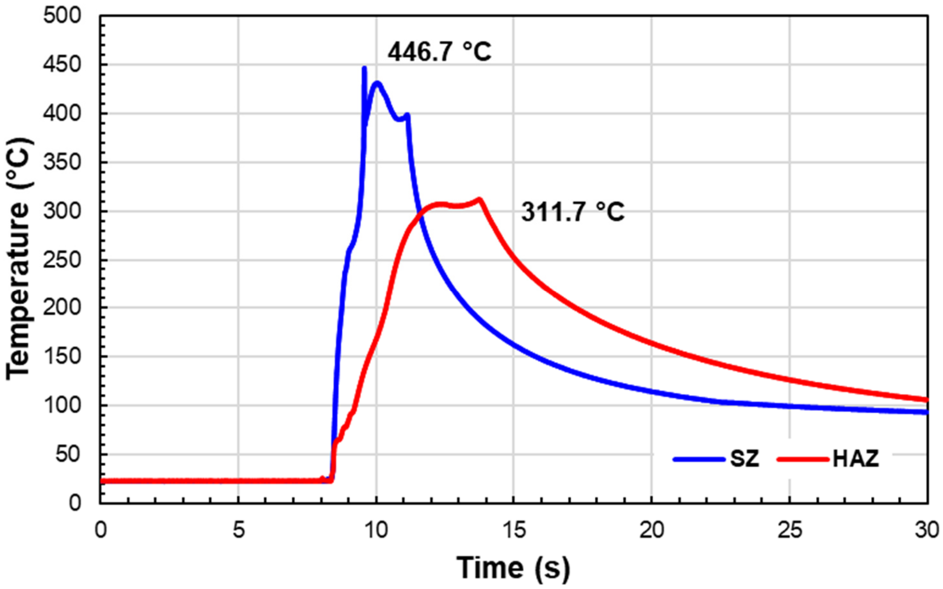

Figure 5.15 – Temperature measurement indicating thermal behavior in the SZ, and HAZ during the load-controlled Refill FSSW process.

Figure 5.16 shows the Al-Mg_2Si diagram phase (an isopleth of the Al-Mg-Si ternary diagram). It is possible to observe how the temperatures reached during the welding process affects the stability of the AA6016 alloy precipitates [72].

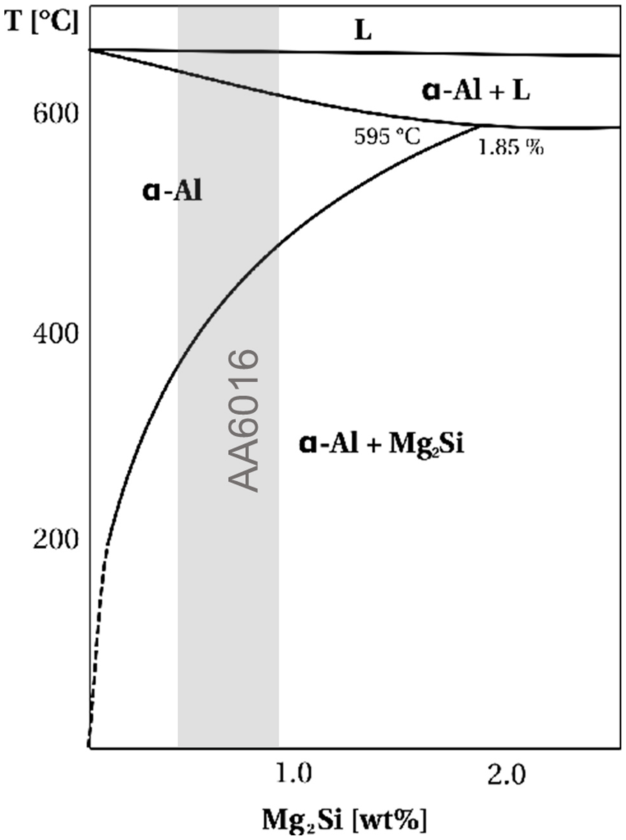

Figure 5.16 – Al-Mg_2Si diagram phase [72].

The data presented of the variation of hardness across the welded joint (figure 5.10, 5.11 and 5.12) corroborate with the expected to the coalescence and dissolution of the precipitates. The SZ was subjected to 450˚C and presented high hardness values resulted from precipitates dissolution, dynamic recrystallization, and re-precipitation, and the HAZ under temperatures close to 300˚C showed lower hardness values due to the precipitate coarsening.

5.4.2 Differential Scanning Calorimetry

To study the precipitation behavior in the weld and confirm the hypothesis of the dissolution process in SZ and coarsening process in HAZ, based on hardness and temperature measurements, the DSC analysis of samples from the SZ and HAZ in as-welded condition and the BM were carried out. The area under the peak indicated that the intensity of the precipitation or dissolution and the temperature at which it occurred was related to the thermal stability of that phase [73]. The thermal behavior of these three regions was compared with the DSC signal reported by Osten et al. [15] for the AA6016.

Figure 5.17 shows the DSC curves of the BM in red color, and of BM after solution heat treatment and water-quenching in black color. The first signal, labeled as A, found in the BM solution heat-treated sample was the exothermic peak associated with the precipitation of GP zones. The second signal, labeled as B, is an endothermic signal, associated with GP zones dissolution. The next exothermic peak is associated with the precipitation of β'' (peak C), mainly responsible for the maximum peak of hardness for AlMgSi aluminum alloys. The last two signals found are associated with overaging conditions, the fourth signal is related to the precipitation of β' (peak D), and the fifth signal was the endothermic peak related to the dissolution of all remaining phases, predominantly β(Mg2Si) [15].

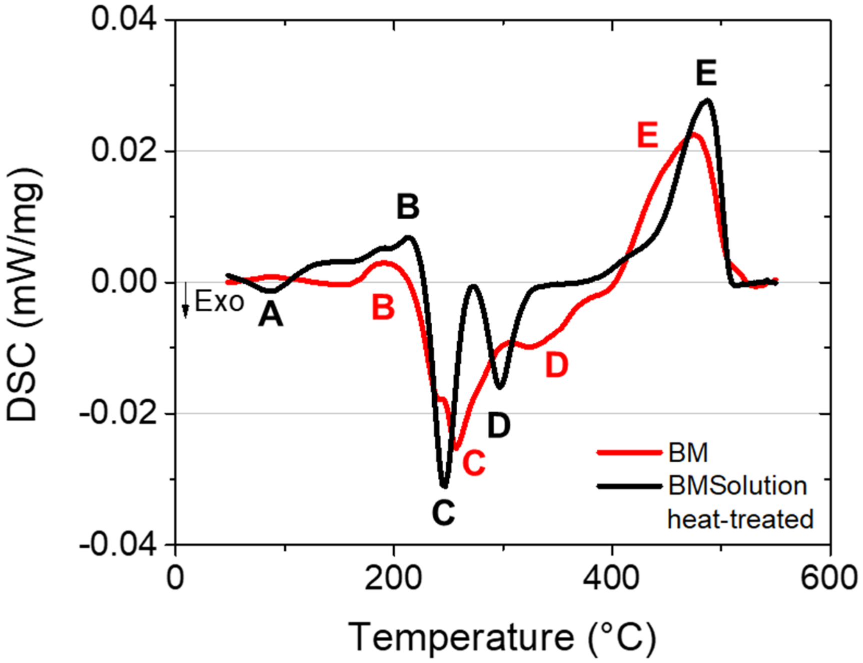

Figure 5.17 – DSC curves of the base material (AA6016-T4) – red line, and of base material after solution heat treatment and water quenching - black line.

On the other hand, for the BM in the T4 condition, the first signal obtained was peak B. Since in T4 condition, the GP zones are the main phase precipitated [70]. The non-existence of peak A indicates that there is no remaining potential for GP zones formation. Peak C, with a different shape, due to a possible overlap of two peaks, represents the precipitation of β”. This signal is a weak exothermic precipitation signal compared to the solution heat-treated sample. Since the BM is in the T4 condition, some volume of β” could be already precipitated, and only a remaining precipitation process is observed in the DSC curve. The fourth signal (peak D) is dislocated to higher temperatures compared with the solution heat-treated sample. It represents the precipitation of β’. Finally, peak E was the endothermic peak related to the dissolution of all remaining phases, predominantly β(Mg2Si), as mentioned for the solution heat-treated BM.

Figure 5.18 shows the DSC curves of SZ (figure 5.18 (a)) and HAZ (figure 5.18 (b)), both in comparison with the DSC curve of BM.

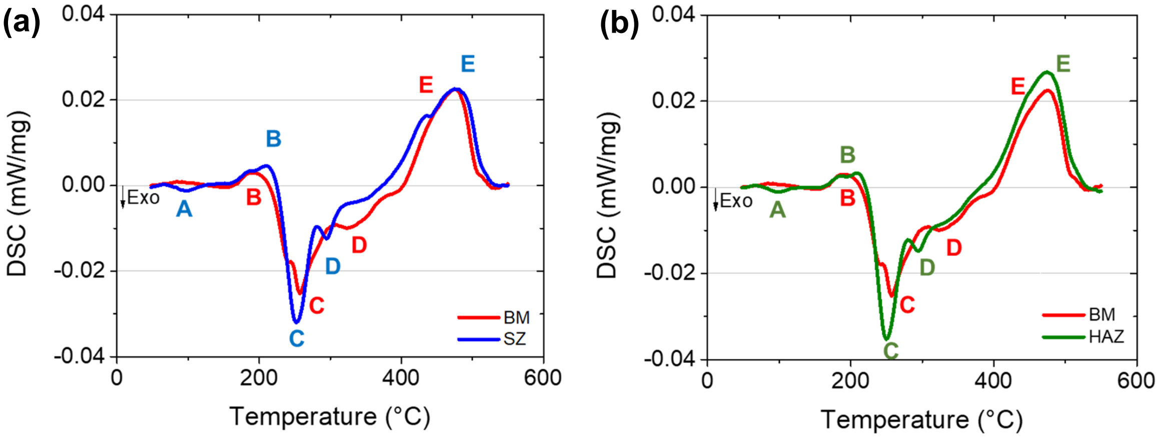

Figure 5.18 – DSC curves of (a) base material (AA6016-T4) – red line and SZ - blue line, and of (b) base material (AA6016-T4) – red line and HAZ - green line.

Regarding the SZ and HAZ, the most important difference between the weld zones and the BM is associated with the exothermic signal related to the GP zones precipitation (peak A). Since this peak is observed in both weld zones, the hypothesis of precipitates dissolution can be confirmed. Regarding the HAZ, the main effect present should be precipitates coarsening, although the dissolution has occurred in part. Thus, the hardness reduction is associated both by the coarsening and the dissolution without complete re-precipitation. Differently of the SZ, under high strain energy, which can increase the driving force for partial re-precipitation, presents high hardness values due to this phenomenon.

5.4.3 Bake hardening treatment

After the bake hardening treatment, all the weld regions present an increase in the hardness values both for the top and bottom plates of the joint, as shown in the hardness profile in figure 5.19.

An increase around 20-30 $HV_{0.2}$ was observed in the total hardness profile of the top plate. The BM in the as-welded condition has a hardness average of 61 $HV_{0.2}$, whereas the bake hardened condition has an average of 85 $HV_{0.2}$. In the SZ was observed an increase from 62 $HV_{0.2}$ to 85 $HV_{0.2}$, on average. And as in the as-welded condition, for the bake hardened condition, the hardness values start to decrease in the TMAZ until a minimum of 71 $HV_{0.2}$ at the HAZ, 20 $HV_{0.2}$ more than the as-welded value. Differently of the as-welded condition, the bake hardened sample did not show a relatively constant hardness, but a hardness values variation from approximately 67 $HV_{0.2}$ to 84 $HV_{0.2}$ in the SZ. However, in the other regions, a relatively constant hardness equal to 70 $HV_{0.2}$ can be observed. The hardness increment for all the weld regions might be related to the precipitation and re-precipitation of β” phase and precipitation of β’ phase caused by bake hardening treatment [70].

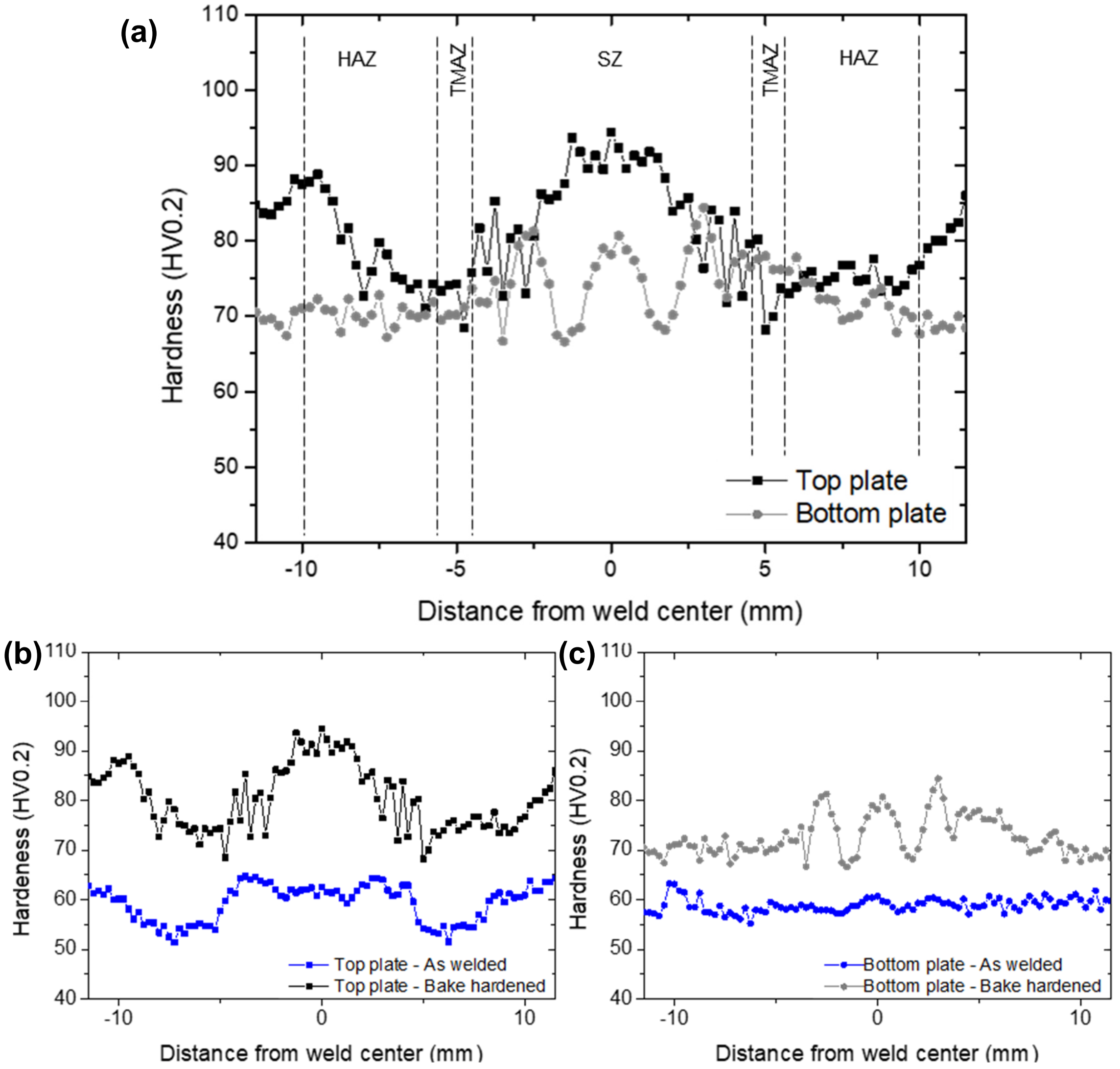

Figure 5.19 – (a) Microhardness profile measured in the mid-thickness of the upper (black square) and bottom sheet (gray circle) of the cross-section of load-controlled Refill FSSW joint after bake hardening treatment and comparison of the hardness profile of the (a) top plate in bake hardened (black square) and as-welded (blue square) condition and of the (c) bottom plate in bake hardened (gray circle) and as-welded (blue circle) condition.

The effect of bake hardening treatment in shear strength for the samples is shown in figure 5.20. A slight improvement in the shear strength was observed. The samples produced with the optimized process parameters when tested in the as-welded condition present an LSS equal to 4.84 ± 0.06 kN whereas when subjected to the bake hardening treatment the LSS was 5.25 ± 0.19 kN.

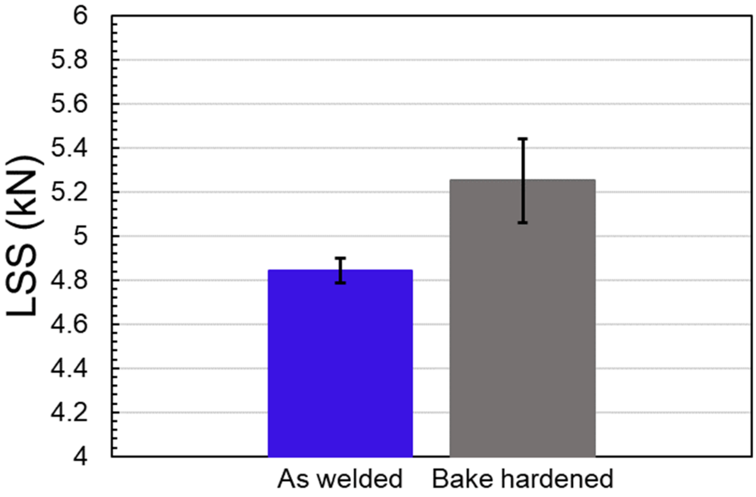

Figure 5.20 – LSS average of samples performed through the load-controlled Refill FSSW process tested in as-welded and bake hardened conditions.

As observed in the as-welded samples, the pull-out failure mode was also observed in the samples subjected to bake hardening treatment. The pull-out failure is the main failure mode even with the heat treatment condition since the bake hardening treatment provided an increase in hardness evenly along the welded joint. The HAZ continued to be the region with the lowest hardness and SZ the one with the highest, which favors the pull-out failure and avoids through-the-weld failure mode.

Although the results of increased hardness and strength have been achieved, the paint-bake treatment is too short to fully exploit the age-hardening potential of these AlMgSi alloys. Hence, the microstructure in the conventional T4 temper must be modified by creating clusters that grow and readily transform into coherent precipitates upon bake hardening. A pre-aging treatment between 140 °C and 180 °C for around 10 minutes is claimed to be optimum the AA6016 sheet as it results in an effective bake hardening response in terms of hardness increasing without impairing the stampability and the shape accuracy during the manufacturing of the body panel at the automotive sector [70, 74, 75].

5.5 DYNAMIC MECHANICAL PROPERTIES

5.5.1 Fatigue Results

Fatigue tests were performed for the optimized condition obtained through Box-Behnken design with a lap shear strength of 4.84 kN, which is above the requirements of AWS D17.2/D17.2M [53], as previously presented.

Table 5.4 displays the conditions of the tests such as the different loads level percentages (50%, 25%, 15%, 12.5%, and 10%) of the maximum lap shear strength (4.84 kN) and their corresponding loads, as well as the number of cycles until fracture and the failure mode obtained in each test. A stopping criterion of 5.0 x 10^6 cycles was applied; thus, some tests were terminated manually as their cycles were beyond this limit.

Table 5.4 – Load levels and results of fatigue tests for Refill FSSW specimens.

Load level (%)	Max load (N)	Min load (N)	$\Delta L/2$ (N)	R	Cycles (N_f)	Failure mode
50	2420	242	1089	0.1	5174	Pull-out
					5437	Pull-out
					5535	Pull-out
25	1210	121	544.5	0.1	117944	Pull-out
					126728	Pull-out
					135021	Pull-out
15	726	73	326.5	0.1	1189887	Eyebrow
					953983	Eyebrow
					1017422	Eyebrow
12.5	605	61	272	0.1	2115907	Eyebrow
					1865680	Eyebrow
					1493510	Eyebrow
10	484	49	217.5	0.1	>5000000	-
					>5000000	-
					>5000000	-

5.5.2 Weibull Distribution and L-N Curves

With the data in Table 5.4, and using equations (4.2) to (4.4) described in section 4.5.2.1.1, it is possible to obtain the Weibull plots for the different load conditions as shown in figure 5.21. However, since none of the samples tested for 10% of the maximum load failed, these data have not been used in further analysis.

Recurring to the plots, it is possible to obtain the Weibull slope (β) and characteristic life (α) values by linear regression since the slope is given by β and the linear coefficient –βln (α). The values of α and β for each load condition, as well as the Weibull mean life (MTTF) obtained from equation 4.5., are described in table 5.5.

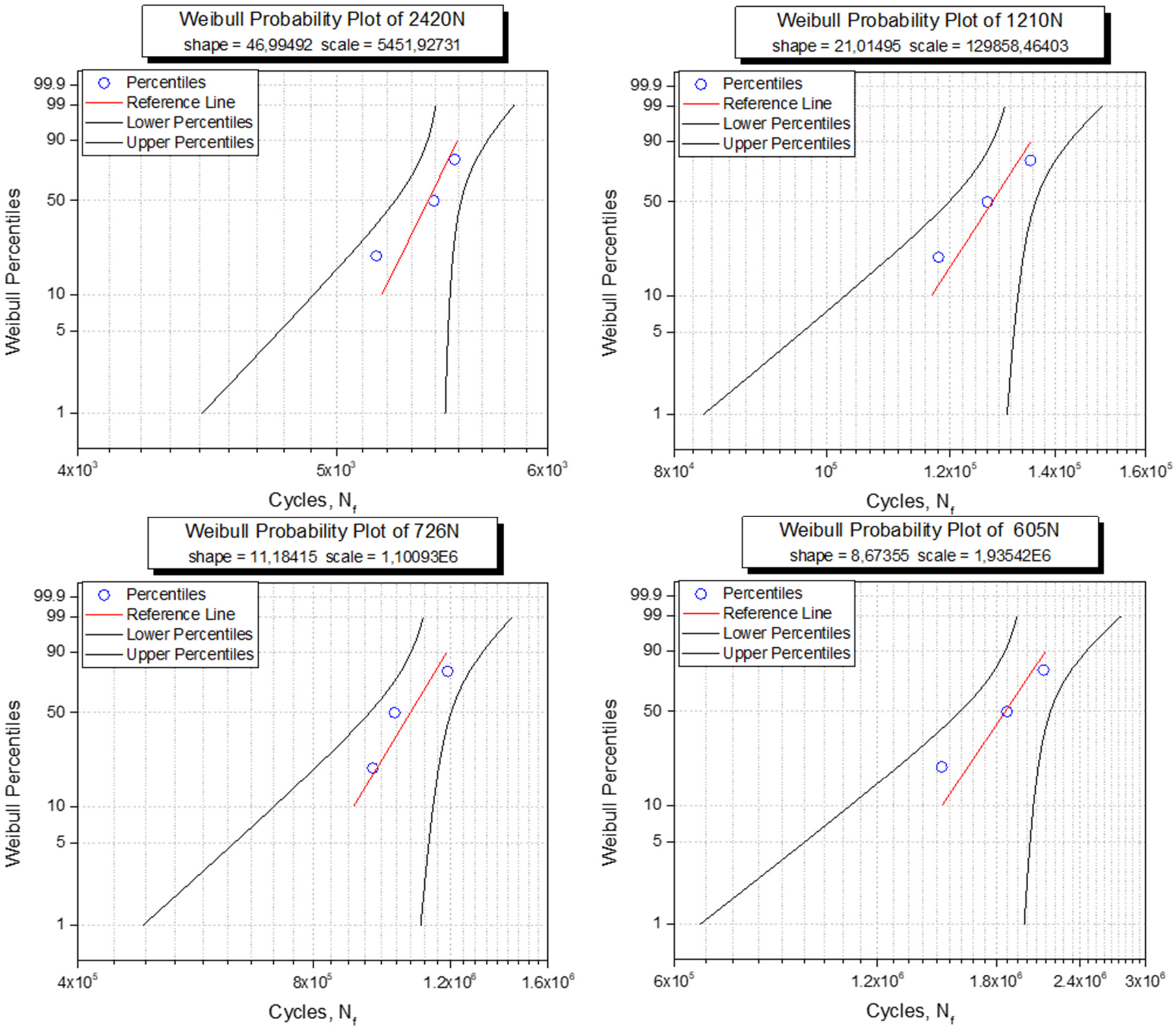

Figure 5.21 – Weibull plots for the tested different load levels.

Table 5.5 – Weibull parameters and mean life for each load level.

Load (N)	Scale parameter (α)	Shape parameter (β)	MTTF (cycles)
2420	5451.92731	46.99492	5387.35892
1210	129858.46403	21.01495	126570.40691
726	1.10093E6	11.18415	1.05217E6
605	1.93542E6	8.67355	1.82967E6

With these results, it is possible to construct the L-N curve for these welds as shown in figure 5.22, in which the power function used for the evaluation of the fatigue test data and the resulting regression curve are also presented, being equation 5.3 the equation of this curve. The high correlation coefficient $R^2 = 0.9989$ obtained by adjusting the data to the regression curve indicates that regression is an adequate fit for the Weibull data and suitable for reliable prediction of the fatigue life of the samples.

$$L = 17371.2(N_f)^{-0.229} \tag{5.3}$$

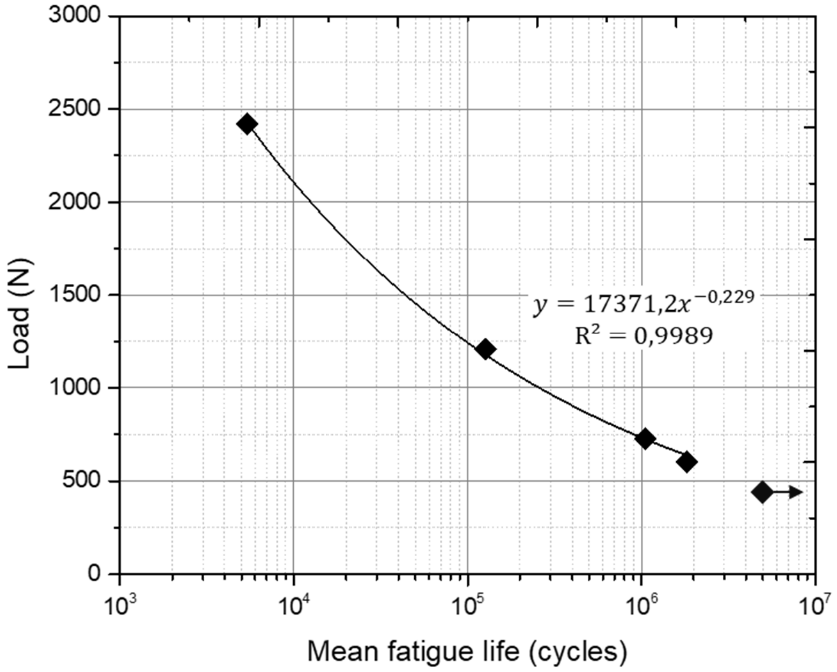

Figure 5.22 – L–N curve of Refill FSSW of AA6016-T4.

From the experimental data, the fatigue life at 5 x 10^6 cycles is 484 N in terms of load, being estimated as 508 N by the power function. This load value represents approximately 10% of the static lap shear strength and is close to those reported in the literature for joints performed through position-controlled Refill FSSW, as mentioned in section 3.2.3. Effertz et al. [45], evaluated the fatigue behavior of similar refill friction stir spot welds of AA7050-T76 and obtained a fatigue life corresponding to 10% of the maximum lap shear load, Lage et al. [48] reported a fatigue life of 9% of the static shear strength for refill friction stir spot welded AlMgSc alloy, and Brzostek et al. [57] on their study with similar refill friction stir spot welds of AA2024-T3 reported a fatigue life of 15% of the maximum lap shear load.

The relative coefficients of variation for each mean life were computed using equation 4.6, to evaluate the relative dispersion of the data, which is particularly useful for designers for purposes of data accuracy and repeatability. According to these results, scatter in fatigue life values are low even for high cycles, as shown in figure 5.23.

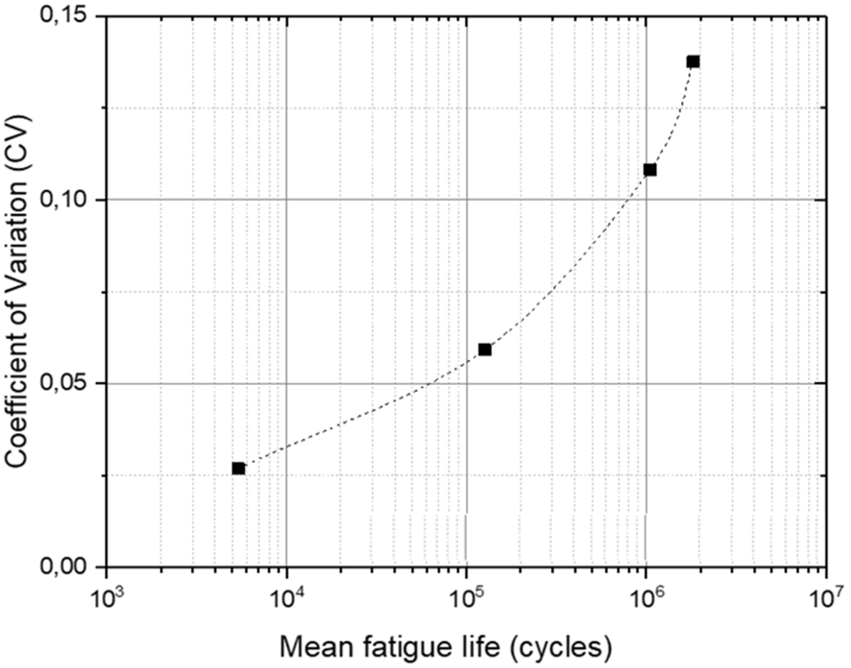

Figure 5.23 – Effect of the mean fatigue life on the coefficients of variation.

Finally, figure 5.24 shows the L-N curves associated with three different reliability levels (R), which have been drawn by using equation 4.8.

These curves are important to predict fatigue life to be achieved according to the level of reliability, which may vary according to the project, such as automotive, aerospace, or other transportation industries. Projects that require greater reliability, as the case of aeronautical projects, high levels of reliability, and safety are required, since they guarantee greater chances of joints survival. This is because the higher the level of reliability, the shorter the fatigue life for a given load, ensuring a greater probability of survival of the welds.

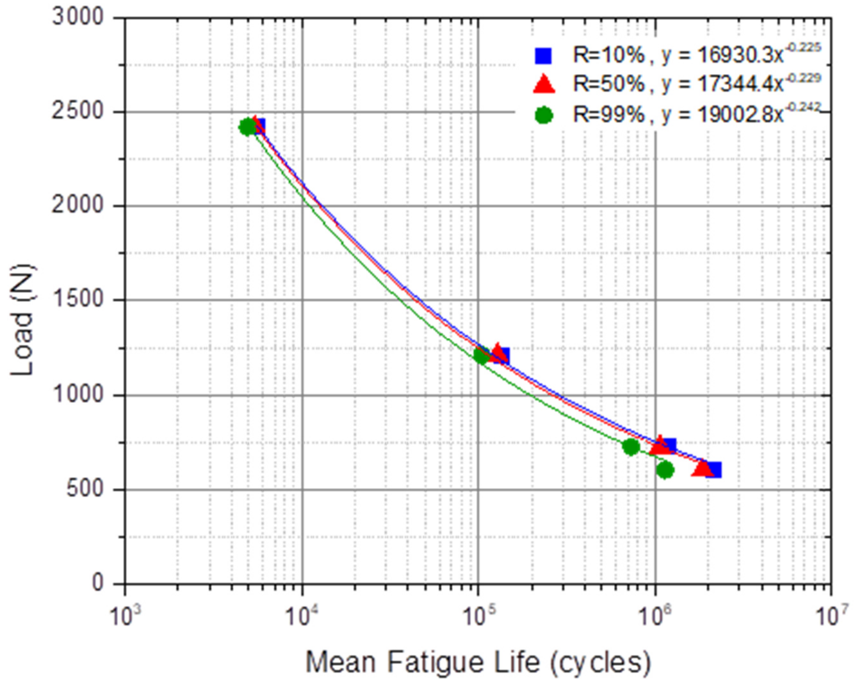

Figure 5.24 – L–N curves for different reliability levels.

Furthermore, comparing the welds produced through the load- and position-controlled systems, similar fatigue behavior was observed. Under a level load corresponding to 15% of the maximum LSS value, obtained during the static mechanical test of the samples performed through load- and position-controlled systems, which are statistically identical (4.84 ± 0.06 and 4.82 ± 0.22, respectively), the same number of cycles equal to 1.0 x 10^6 was obtained, as shown in figure 5.25.

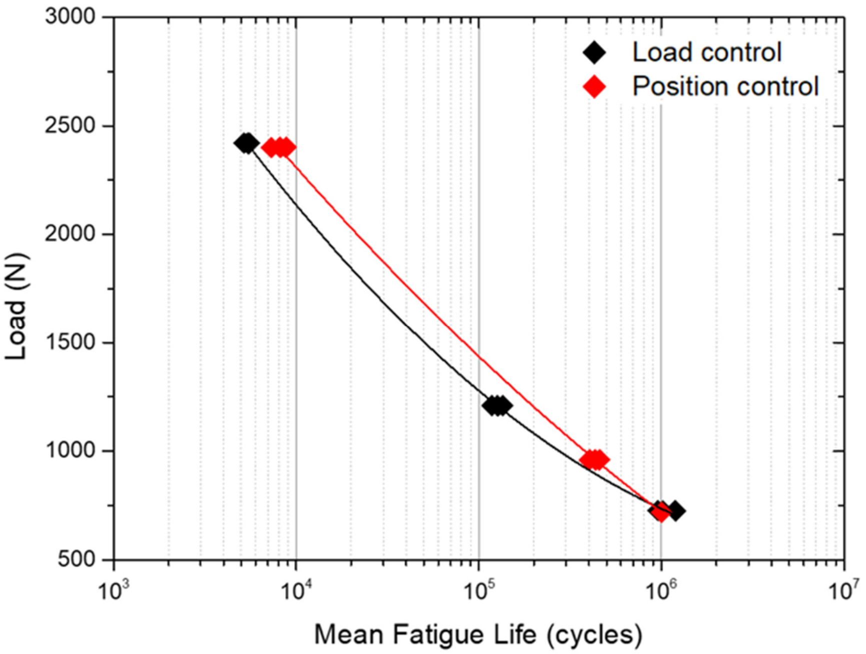

Figure 5.25 – L-N curves of samples performed with load- and position-controlled system.

5.5.3 Fracture Analysis

As shown in table 5.4, the welds analyzed in this work presented two different failure modes under cyclic loads. Under low-cycle loading (50% and 25% of the maximum LSS) the pull-out failure mode was observed, as shown in figure 5.26 (a) and 5.26 (b), whereas under high-cycle loading (15% and 12.5% of the maximum LSS) the failure mode through the top plate, named eyebrow, was noticed, as shown in figure 5.26 (c) and 5.26 (d). As already mentioned, at 10% of the maximum LSS the samples did not fail (figure 5.26 (e)).

In agreement with the literature review presented in section 3.2.3, the pull-out failure mode under low-cycle loading conditions was reported by Effertz et al. [45] and Brzostek et al. [57] in their studies with similar Refill FSSW joints of aluminum alloys. This kind of failure was observed under high-cycle loading conditions by Plaine et al. [56] in their report of dissimilar aluminum and titanium Refill FSSW joints. Considering the eyebrow failure mode of samples tested under high-cycle loading conditions, the same behavior was reported by Effertz et al. [45] and Brzostek et al. [57]. While Plaine et al. [56] reported the eyebrow failure mode for samples tested under low-cycle loading conditions. Lage et al. [48] also observed the eyebrow failure mode in most welds tested under different load levels.

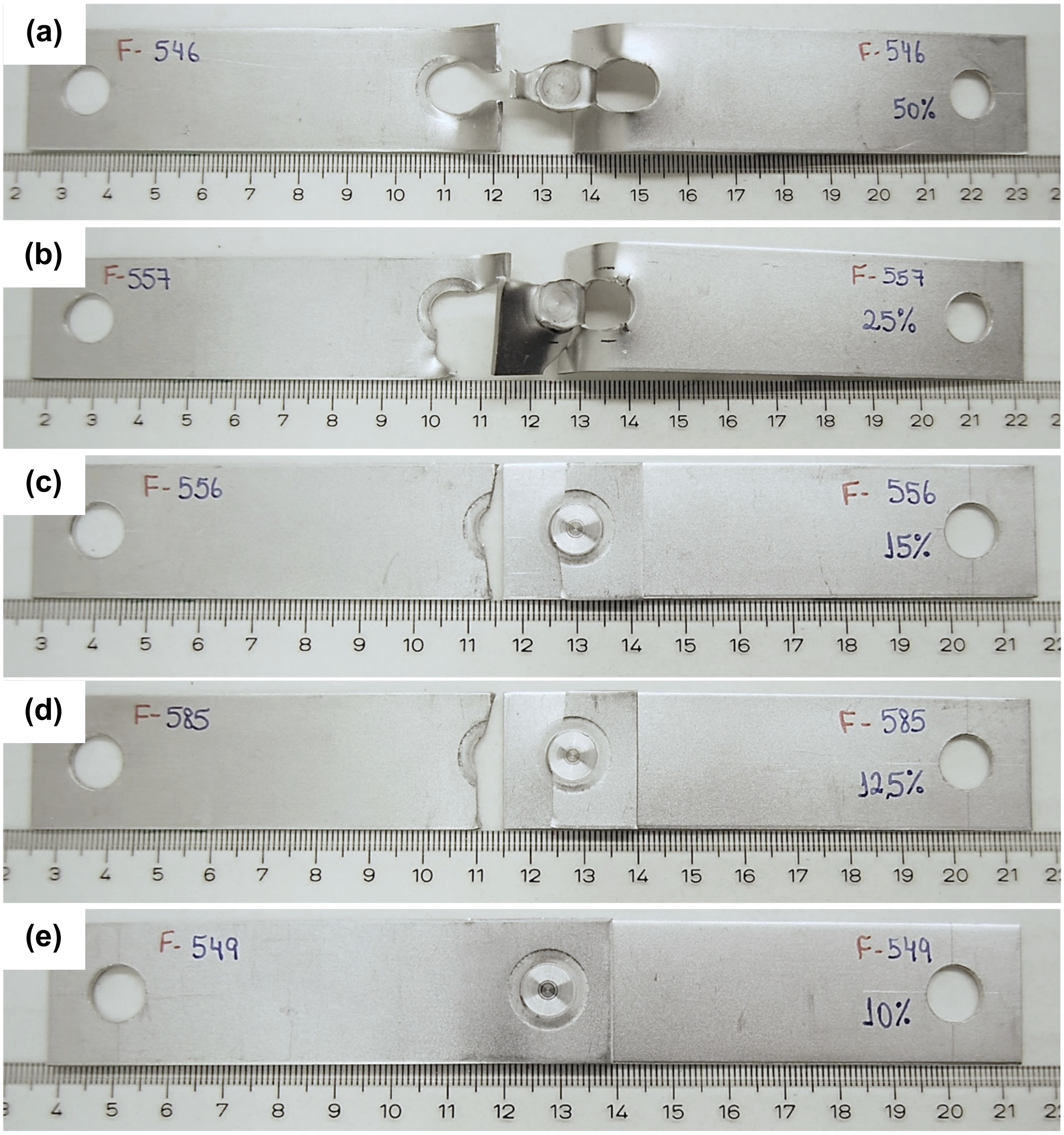
(a)
F- 546
F-546
50%
(b)
F-557
F-557
25%
(c)
F- 556
F- 556
15%
(d)
F-585
F- 585
12,5%
(e)
F- 549
F-549
10%

Figure 5.26 – Failure modes identified during fatigue tests at the different loads level percentages: (a) pull-out at 50%, (b) pull-out at 25%, (c) eyebrow at 15%, (d) eyebrow at 12.5%, and no fracture at 10%.

An overview of the fracture modes, pull-out, and eyebrow, are shown in figure 5.27 (a) and 5.27 (b), respectively. These surfaces correspond to the top plate separated from the nugget. The arrows in figure 5.27 indicate the nucleation and crack propagation. To clarify the details of the fracture, the SEM analysis were performed in selected regions (a) and (b) from the eyebrow fracture, shown in figure 5.28, and (A) to (F) from both fracture modes, shown in figure 5.29 and 5.30.

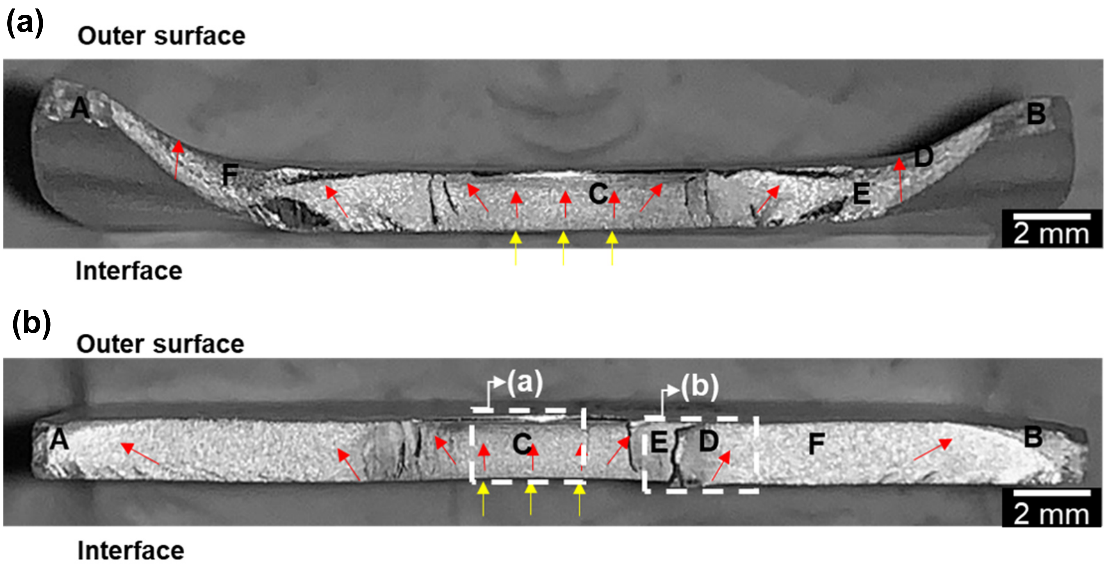

Figure 5.27 – Macrograph of the (a) pull-out and (b) eyebrow fatigue fracture surfaces indicating cracks nucleation site (yellow arrows) and crack propagation directions (red arrows).

Figure 5.28 (a) shows the presence of some steps near the top and bottom plate interface, indicated by the yellow arrows at the bottom of the figure. The presence of these steps reveals the existence of multiple sites of nucleation of fatigue cracks due to regions subject to tensile stresses on the weld periphery. After the crack is nucleated, it propagates in the thickness of the plate, in a region close to the SZ and TMAZ interface. Figure 5.28 (b) corresponds to the transition from crack propagation around the weld periphery to the plate width. Crack propagation also occurs from the plate interface, in the hook region and transition from the welded and non-welded region, to the outer surface of the top plate.

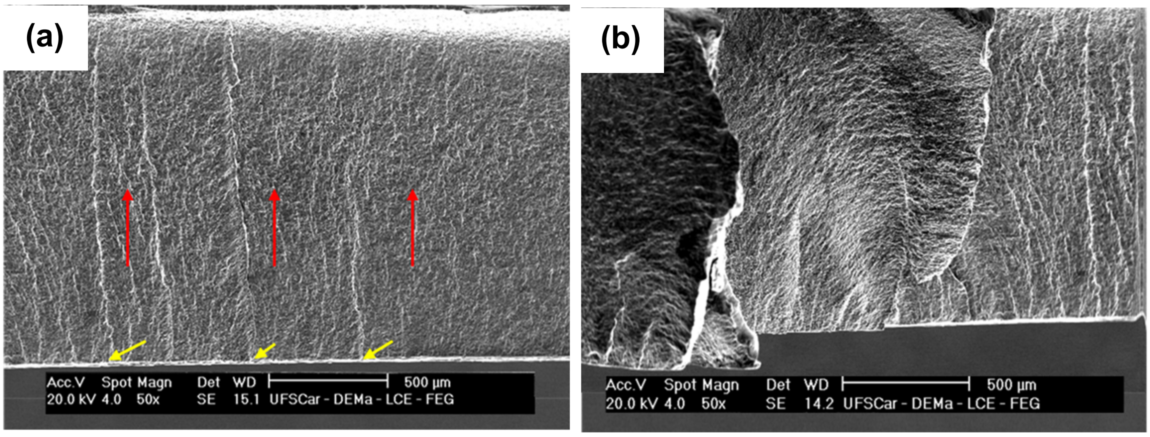
(a)
Acc.V Spot Magn Det WD 500 µm
20.0 kV 4.0 50x SE 15.1 UFSCar - DEMa - LCE - FEG
(b)
Acc.V Spot Magn Det WD 500 µm
20.0 kV 4.0 50x SE 14.2 UFSCar - DEMa - LCE - FEG

Figure 5.28 – SEM fatigue fracture surfaces: (a) presence of steps at the interface between the plates (fatigue crack nucleation points – yellow arrows and direction of crack propagation – red arrows) and (b) transition region between the weld periphery and the plate width.

The selected regions (A) to (F) of the pull-out failure mode (figure 5.27 (a)) are presented in figure 5.29. In the center of the welded area, figure 5.29 (C), fatigue striation was observed, indicating cracks propagation in the thickness direction (from the interface to the outer surface), as previously mentioned. Figure 5.29 (E) shows signs of cleavage, and figure 5.29 (D) and (F) illustrate the presence of dimples. In the plastically deformed region that remains unchanged until the crack propagation reaches the final fracture area are observed the presence of dimples, as shown in figure 5.29 (A) and signs of cleavage, as shown in figure 5.29 (B), indicating ductile fracture in this region.

On the other hand, figure 5.30 presents the selected regions (A) to (F) of the eyebrow failure mode (figure 5.27 (b)). Figure 5.30 (C) corresponding to the weld center area illustrates fatigue striations, which are also observed in the region corresponding to the transition between the weld periphery and the plate width (figure 5.30 (D) and (E)), with different crack propagation direction. The fractured region in the base material (plate width) also shows fatigue striation, as shown in figure 5.40 (F). Finally, in the final fracture region is possible to observe the presence of dimples (figure 5.30 (A) and (B)), indicating ductile fracture in this area.

The mechanisms and characteristics of the pull-out and eyebrow failure modes observed in this work are similar to previous works observations and explanations [45, 48, 56, 57].

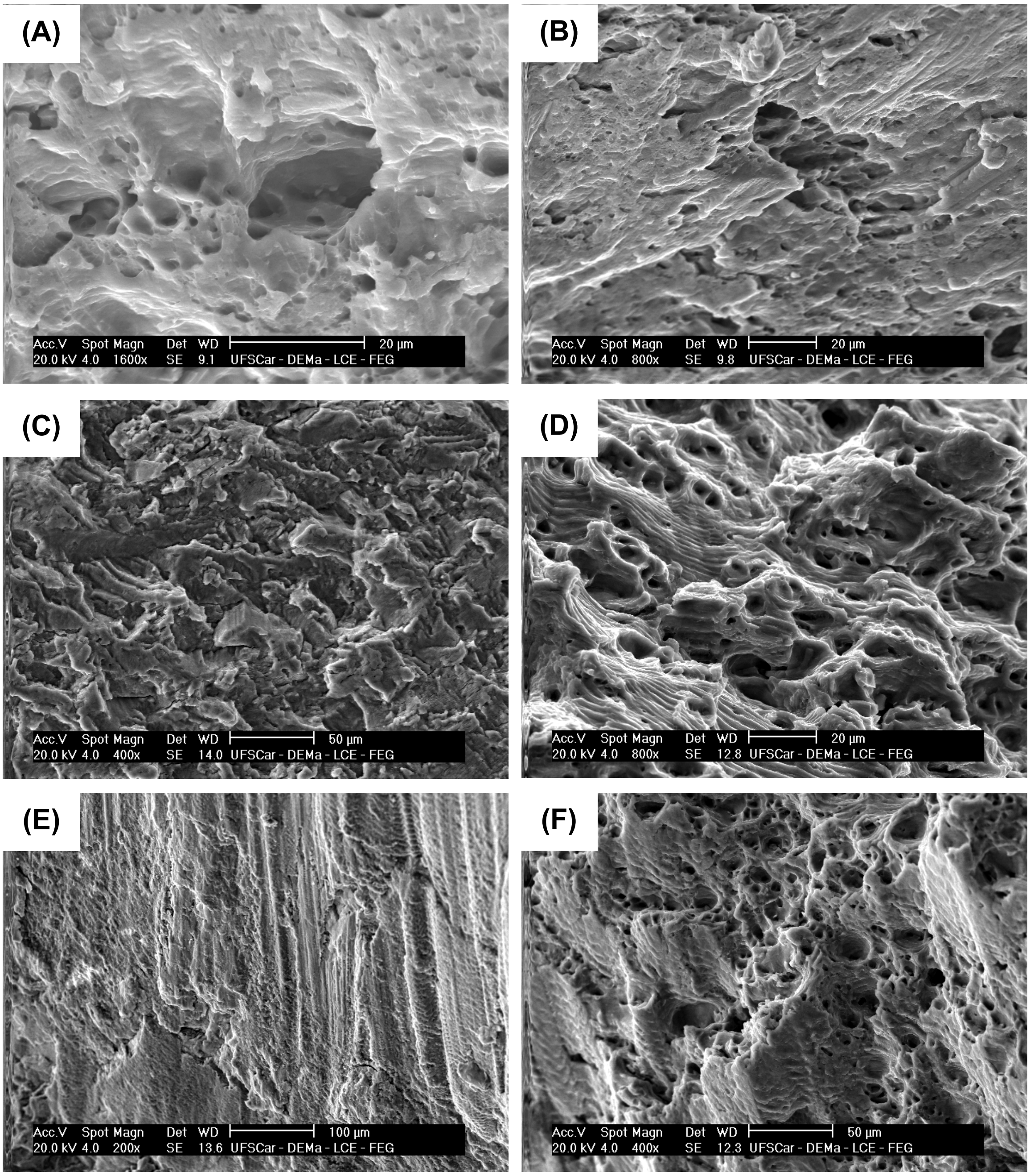
(A)
Acc.V Spot Magn Det WD 20 µm
20.0 kV 4.0 1600x SE 9.1 UFSCar - DEMa - LCE - FEG
(B)
Acc.V Spot Magn Det WD 20 µm
20.0 kV 4.0 800x SE 9.8 UFSCar - DEMa - LCE - FEG
(C)
Acc.V Spot Magn Det WD 50 µm
20.0 kV 4.0 400x SE 14.0 UFSCar - DEMa - LCE - FEG
(D)
Acc.V Spot Magn Det WD 20 µm
20.0 kV 4.0 800x SE 12.8 UFSCar - DEMa - LCE - FEG
(E)
Acc.V Spot Magn Det WD 100 µm
20.0 kV 4.0 200x SE 13.6 UFSCar - DEMa - LCE - FEG
(F)
Acc.V Spot Magn Det WD 50 µm
20.0 kV 4.0 400x SE 12.3 UFSCar - DEMa - LCE - FEG

Figure 5.29 – Fracture surface investigation of the pull-out failure mode for low-cycle loading condition: (A) dimples and (B) cleavage and dimples indicating ductile fracture in the final fracture area; (C) fatigue striations in the center area; (D) dimples, (E) cleavage and (F) dimples in the deformed region.

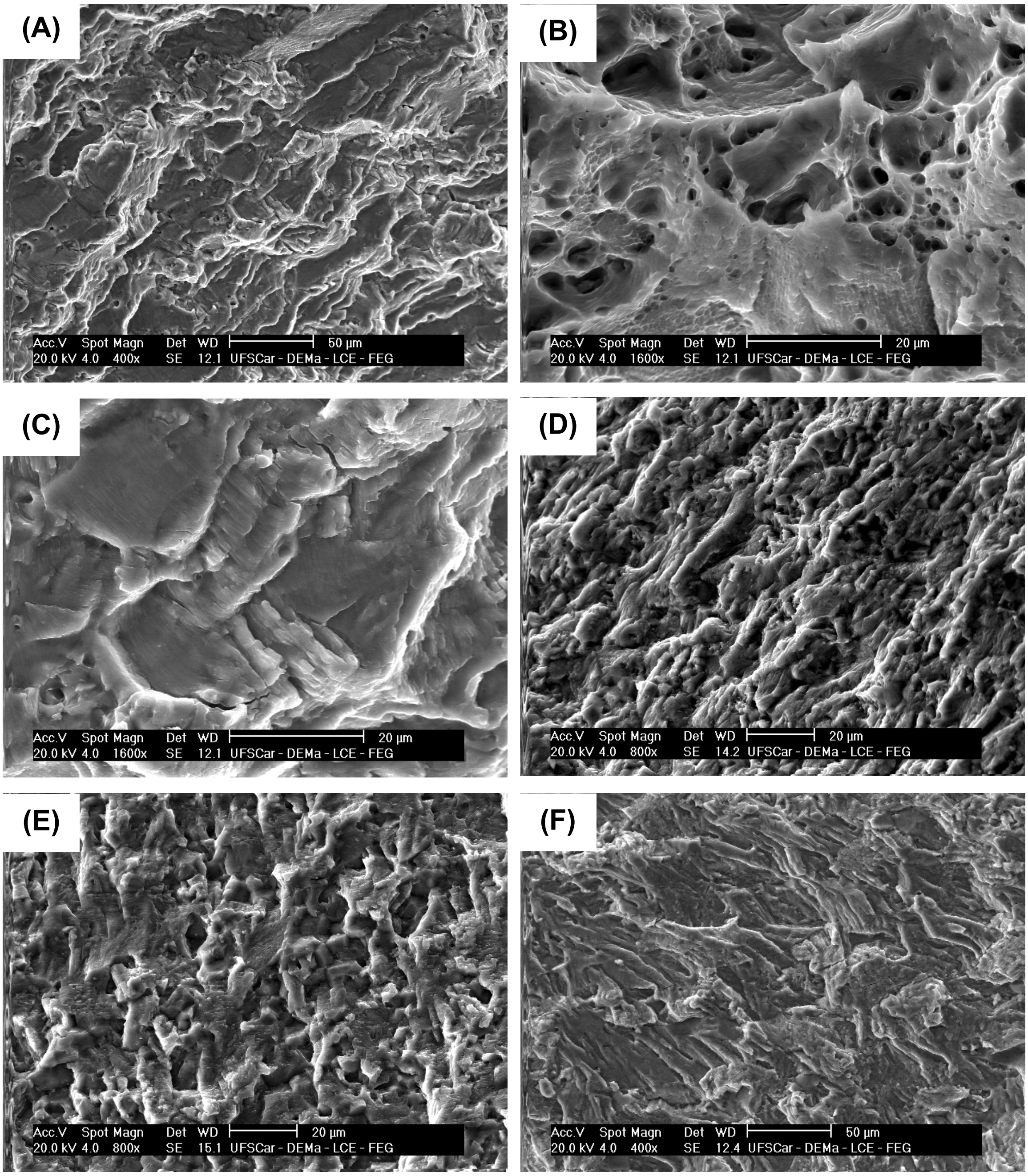
(A)
Acc.V Spot Magn Det WD 50 µm
20.0 kV 4.0 400x SE 12.1 UFSCar - DEMa - LCE - FEG
(B)
Acc.V Spot Magn Det WD 20 µm
20.0 kV 4.0 1600x SE 12.1 UFSCar - DEMa - LCE - FEG
(C)
Acc.V Spot Magn Det WD 20 µm
20.0 kV 4.0 1600x SE 12.1 UFSCar - DEMa - LCE - FEG
(D)
Acc.V Spot Magn Det WD 20 µm
20.0 kV 4.0 800x SE 14.2 UFSCar - DEMa - LCE - FEG
(E)
Acc.V Spot Magn Det WD 20 µm
20.0 kV 4.0 800x SE 15.1 UFSCar - DEMa - LCE - FEG
(F)
Acc.V Spot Magn Det WD 50 µm
20.0 kV 4.0 400x SE 12.4 UFSCar - DEMa - LCE - FEG

Figure 5.30 – Fracture surface investigation of the eyebrow failure mode for high-cycle loading condition: (A) and (B) dimples indicating ductile fracture in the final fracture area; (C) fatigue striations in the center area; (D) and (E) fatigue striations in the transition region between the weld periphery and the plate width, and (F) fatigue striations in the base material.

Therefore, the cracks propagation during the high-cycle loading condition led to the formation of fatigue striation through all fracture surface, except in the final regions of the fracture. In this region occurred plastic deformation and ductile fracture, indicating that the fatigue crack did not become unstable before the complete fracture [48]. However, during the low-cycle loading condition, the formation of fatigue striation was observed only in the welded region while in the base material (plate width) occurred plastic deformation until the final fracture region, indicating instability of the fatigue crack behavior.

6 CONCLUSIONS

Considering the main objectives of this work, the following conclusions were drawn for the Refill FSSW of AA6016-T4 joints:

- The use of the statistical design of experiments Box-Behnken and analysis of variance was satisfactory in the optimization of the process parameters and the analysis of the influence of the process parameters in the mechanical resistance of the AA6016-T4 welds produced in this work with the load-controlled Refill FSSW.
- The combination of process parameters defined as an optimized condition, which maximized joint shear strength was: RS = 1000 rpm, RF = 9 KN, PD = 1.6 mm and PF = 10 kN, resulting in an LSS equal to 4.84 ± 0.06 kN. The LSS is above the minimum shear value according to AWS D17.2 Specification for Resistance Welding for Aerospace Applications, important in terms of automotive industry application. The most influential process parameters in the static mechanical resistance were the RS and RF.
- The load and position control, in combination with the anti-sticking coated tool and thread tool, respectively, directly influences the microstructure differences observed in the samples of the AA6016-T4 alloy produced by the two systems. These microstructure differences are related to the presence of a center discontinuity, a non-homogeneous grain structure in the top center region, and a hook tip flat in the welds produced by the load-controlled process. While in the welds produced by the position-controlled process a sound center region whit uniform grain structure and hook tip pointing up was observed.
- The LSS obtained for the load- and position-controlled system were 4.84 ± 0.06 and 4.82 ± 0.22, respectively. These results are statistically identical and above to the minimum shear value according to AWS D17.2 Specification for Resistance Welding for Aerospace Applications. It is possible to affirm that the microstructure differences did not influence the static mechanical properties (LSS) of the weld produced by the two Refill FSSW process variants.

- The pull-out failure mode was observed after lap shear tests in the welds produced by both position- and load-controlled process. This fracture mode was associated with the circumferential crack around the spot weld in a region characterized by a drastic change of hardness, more specifically in the TMAZ, as observed in the hardness profile and map.
- Bake hardening treatment increases around 20-30 $HV_{0.2}$ the total hardness profile of the top plate, and improved the shear strength of the AA6016-T4 welds produced by Refill FSSW process with load control and anti-sticking coated tool. The failure mode has not changed.
- Hardness profiles combined with DSC analysis confirmed that precipitates dissolution takes place in the SZ and whereas precipitates coarsening occurs in the HAZ in the welds produced with the optimized process parameters set.
- Fatigue tests were performed for the optimized condition obtained through Box-Behnken design with a lap shear strength of 4.84 kN. L-N curves for the optimized welds were drawn. Fatigue life values (higher than 5.0×10^6) were found at 10% of the maximum shear load levels obtained in static tests in agreement to previous works. Two failure modes were observed. For low-cycle loading conditions, the pull-out failure mode was observed, whereas for high-cycle loading conditions the eyebrow was seen. The fatigue cracks propagation during the high-cycle loading condition led to the formation of fatigue striation through all fracture surfaces, except in the final regions of the fracture in which plastic deformation and ductile fracture occurred. This indicates that the fatigue crack did not become unstable before the complete fracture. Under low-cycle loading conditions, the formation of fatigue striation was observed only in the welded region, while in the base material (plate width), plastic deformation occurred until the final fracture region, indicating instability of the fatigue crack behavior.

7 SUGGESTIONS FOR FUTURE WORKS

Although a satisfactory evaluation of Refill FSSW welds of AA6016-T4 for automotive applications was successfully achieved, additional analysis is proposed to have a more comprehensive investigation and further develop the topic in question, as suggested below:

- Evaluating the effect of bake hardening treatment on the static mechanical properties of AA6016-T4 joints performed by Refill FSSW process with position control and thread tool.
- Evaluating the effect of bake hardening treatment on the dynamic mechanical properties of joints performed by a conventional position-controlled Refill FSSW with thread tool and with a load-controlled Refill FSSW process whit anti-sticking coated tool;
- Evaluating the mechanical resistance of the welds produced with the optimized process parameters defined in the present work under other types of loads, such as coach-peel and cross-tension tests;
- Further investigation of precipitation state of the AA6016-T4 alloy by transmission electron microscopy (TEM) and correlation with DSC analysis and hardness measurements;
- Optimizing the process parameters of the load-controlled Refill FSSW to achieve maximum LSS and short welding time (1 s, for instance).
- Study of the lifetime of the welding tools used in the load-controlled Refill FSSW and position-controlled Refill FSSW processes.

8 REFERENCES

[1] MILLER, W.S., ZHUANG, L., BOTTEMA, J., WITTERBROOD, A.J., DE SMET, P., HASZLER, A., VIREGGE, A. **Recent Development in Aluminium Alloys for the Automotive Industry.** Materials Science and Engineering, 37-49 (2000)

[2] DOSHI, S.J., V GOHIL, A., MEHTA, N., VAGHASIYA, S. **Challenges in Fusion Welding of Al Alloy for Body in White**. Materials Today Proceedings. 5, 6370–6375 (2018). doi:10.1016/j.matpr.2017.12.247

[3] AMBROZIAK, A., KORZENIOWSKI, M. **Using Resistance Spot Welding for Joining Aluminium Elements in Automotive Industry.** Archives of Civil and Mechanical Engineering. 10, 5–13 (2012). doi:10.1016/s1644-9665(12)60126-5

[4] BRISKHAM, P., BLUNDELL, N., HAN, L., HEWITT, R., YOUNG, K., BOOMER, D. **Comparison of Self-Pierce Riveting, Resistance Spot Welding and Spot Friction Joining for Aluminium Automotive Sheet.** SAE Technical Paper Series 1, (2010). doi:10.4271/2006-01-0774

[5] HAGHSHENAS, M., GERLICH, A.P. **Joining of Automotive Sheet Materials by Friction-Based Welding Methods: A Review.** Engineering Science Technology an International Journal 21, 130–148 (2018). doi:10.1016/j.jestch.2018.02.008

[6] CAMPANELLI, L.C., ALCÂNTARA, N.G., DOS SANTOS, J.F. **Soldagem por Ponto no Estado Sólido de Ligas Leves.** Sold. e Inspeção 16, 301–307 (2011)

[7] RZASINSKI, R., KOCHANSKI, L. **Joining Methods in Car Body Construction.** IOP Conference Series: Material Science Engineering. 400, 168–171 (2018). doi:10.1088/1757-899X/400/2/022051

[8] BRÜNGER, E., ENGLER, O., HIRSCH, J. **Al-Mg-Si Sheet Alloys for Autobody Applications.** “Virtual Fabrication of Aluminium Products" Wiley-VCH 2006 (ISBN: 3-527-31363-X) (2006)

[9] GOULD, J.E. **Joining Aluminum Sheet in the Automotive Industry – A 30 Year History.** Welding Journal 91, 12 (2012)

[10] Summary Report. Ducker Worldwide Report. **Aluminum Content in North American Light Vehicles 2016 to 2028**. 1–46 (2017)

[11] The Aluminium Automotive Manual. **Applications - Car body: Body structures**. 1–84 (2013)

[12] MUKHOPADHYAY, P. **Alloy Designation, Processing, and Use of AA6XXX Series Aluminium Alloys.** ISRN Metallurgy 2012, 1–15 (2012). doi:10.5402/2012/165082

[13] DAVIS, J.R. **Aluminum and Aluminum Alloys**. Alloying: Understanding the basics. ASM International, 351-416 (2001). doi:10.1361/autb2001p351

[14] DE HAAN, R., ZHUANG, L., DE SMET, P., BOTTEMA, J., MILLER, W.S. **Differential Scanning Calorimetry Study on AA6016 Alloy**. Aluminum Alloys, Vol 2, Belgium (2001)

[15] OSTEN, J., MILKEREIT, B., SCHICK, C., KESSLER, O. **Dissolution and Precipitation Behaviour During Continuous Heating of Al-Mg-Si Alloys in a Wide Range of Heating Rates.** Materials 8, 2830–2848 (2015). doi:10.3390/ma8052830

[16] MOONS, T., RATCHEV, P., DE SMET, P., VERLINDEN, B., VAN HOUTTE, P. **A Comparative Study of Two Al-Mg-Si Alloys for Automotive Applications.** Scripta Materialia 35, 939–945 (1996). doi:10.1016/1359-6462(96)00244-8

[17] LIANG, Z. **Clustering and precipitation in Al-Mg-Si alloys.** 2012. Dissertation. Helmholtz Zentrum Berlin. doi:10.5442/d0032

[18] The Aluminium Automotive Manual. **Materials: Alloy constitution.** 1-40 (2002)

[19] ZUIKO, I., KAIBYSHEV, R. **Aging Behavior of an Al–Cu–Mg Alloy**. J. Alloys Compd. 759, 108–119 (2018). doi:10.1016/j.jallcom.2018.05.053

[20] DESCHAMPS, A., MARTIN, G., DENDIEVEL, R., VAN LANDEGHEM, H.P. **Lighter Structures for Transports: The role of Innovation in Metallurgy.** Comptes Rendus Phys. 18, 445–452 (2017). doi:10.1016/j.crhy.2017.09.006

[21] MIMICA, R. **Hardness Versus Time Dependency During Artificial Aging of AlMgSi0.5 Aluminum Alloy.** JEL Klasif. 5, 261–270 (2015)

[22] GALVÃO, I., LEITÃO, C., LOUREIRO, A., RODRIGUES, D. **Friction Stir Welding of Very Thin Plates.** Soldagem e Inspeção. 17, 02–10 (2012). doi:10.1590/s0104-92242012000100002

[23] HIRTH, S.M., MARSHALL, G.J., COURT, S.A., LLOYD, D.J. **Effects of Si on the Aging Behaviour and Formability of Aluminium Alloys Based on AA6016.** Materials Science and Engineering, 319–321, 452–456 (2001). doi:10.1016/S0921-5093(01)00969-8

[24] MALLICK, P.K. **Joining for Lightweight Vehicles.** Materials, Design and Manufacturing for Lightweight Vehicles, 275–308 (2010). doi:10.1533/9781845697822.2.275

[25] PENTEADO, K.M. **Otimização da Solda de Pontos por Resistência Elétrica na Liga de Alumínio 5052-H32 através do Projeto e Análise de Experimentos (DOE).** 2011. Masters thesis. Federal University of Itajubá, Minas Gerais.

[26] THOMAS, W.M., NICHOLAS E.D., NEEDHAM, J.C., MURCH, M.G., TEMPLE-SMITH, P., DAWES, C.J. **Friction Welding.** United States Patent US 5,460,317 (1995)

[27] THOMAS, W.M.U., NICHOLAS, E.D. **Friction Stir Welding for the Transportation Industries.** Materials & Design, vol 18, 269–273 (1997)

[28] IWASHITA, T. **Method and Apparatus for Joining.** United States Patent US 6,601,751 B2 (2003)

[29] SHILLING, C. DOS SANTOS, J. **Method and Device for Joining at Least two Adjoining Work Pieces by Friction Welding.** United States Patent US 6,722,556 B2 (2004)

[30] CAMPANELLI, L.C., SUHUDDIN, U.F.H., ANTONIALLI, A.I.S., DOS SANTOS, J.F., ALCÂNTARA, N.G., BOLFARINI, C. **Metallurgy and Mechanical Performance of AZ31 Magnesium Alloy Friction Spot Welds.** Journal of Materials Processing Technology 213, 515–521 (2013). doi:10.1016/j.jmatprotec.2012.11.002

[31] SHEN, J., SUHUDDIN, U.F.H., CARDILLO, M.E.B., DOS SANTOS, J.F. **Eutectic Structures in Friction Spot Welding Joint of Aluminum Alloy to Copper.** Applied Physics Letters 104, 191901 (2014). doi:10.1063/1.4876238

[32] GOUSHEGIR, S.M., DOS SANTOS, J.F., AMANCIO-FILHO, S.T. **Influence of Process Parameters on Mechanical Performance and Bonding Area of AA2024/Carbon-Fiber-Reinforced Poly(Phenylene Sulfide) Friction Spot Single Lap Joints.** Materials & Design, vol 83, 431–442 (2015). doi:10.1016/j.matdes.2015.06.044

[33] PLAINE, A.H., GONZALEZ, A.R., SUHUDDIN, U.F.H., DOS SANTOS, J.F., ALCÂNTARA, N.G. **Process Parameter Optimization in Friction Spot Welding of AA5754 and Ti6Al4V Dissimilar Joints Using Response Surface Methodology.** International Journal of Advanced Manufacturing Technology, vol 85, 1575–1583 (2016). doi:10.1007/s00170-015-8055-5

[34] ROSENDO, T., PARRA, B., TIER, M.A.D., DA SILVA, A.A.M., DOS SANTOS, J.F., STROHAECKER, T.R., ALCÂNTARA, N.G. **Mechanical and Microstructural Investigation of Friction Spot Welded AA6181-T4 Aluminium Alloy.** Materials & Design, vol 32, 1094–1100 (2011). doi:10.1016/j.matdes.2010.11.017

[35] UEMATSU, Y., TOKAJI, K., TOZAKI, Y., KURITA, T., MURATA, S. **Effect of Re-filling Probe Hole on Tensile Failure and Fatigue Behaviour of Friction Stir Spot Welded Joints in Al-Mg-Si Alloy.** Internation Journal of Fatigue. vol 30, 1956–1966 (2008). doi:10.1016/j.ijfatigue.2008.01.006

[36] ZHOU, L., LUO, L.Y., WANG, R., ZHANG, J.B., HUANG, Y.X., SONG, X.G. **Process Parameter Optimization in Refill Friction Spot Welding of 6061 Aluminum Alloys Using Response Surface Methodology.** Journal of Materials Engineering Performance, vol 27, 4050–4058 (2018). doi:10.1007/s11665-018-3472-x

[37] SANTANA, L.M., SUHUDDIN, U.F.H., ÖLSCHER, M.H., STROHAECKER, T.R., DOS SANTOS, J.F. **Process Optimization and Microstructure Analysis in Refill Friction Stir Spot Welding of 3-mm-thick Al-Mg-Si Aluminum Alloy.** International Journal of Advanced Manufacturing Technology. vol 92, 4213–4220 (2017). doi:10.1007/s00170-017-0432-9

[38] Kawasaki Heavy Industries. Manual – Refill FSJ Specific Function.

[39] CAO, J.Y., WANG, M., KONG, L., ZHAO, H.X., CHAI, P. **Microstructure, Texture and Mechanical Properties During Refill Friction Stir Spot Welding of 6061-T6 Alloy.** Materials Characterization, vol 128, 54–62 (2017). doi:10.1016/j.matchar.2017.03.023

[40] DE CASTRO, C.C., PLAINE, A.H., DIAS, G.P., DE ALCÂNTARA, N.G., DOS SANTOS, J.F. **Investigation of Geometrical Features on Mechanical Properties of AA2198 Refill Friction Stir Spot Welds.** Journal of Manufacturing Process. vol 36, 330–339 (2018). doi:10.1016/j.jmapro.2018.10.027

[41] PIETA, G., DOS SANTOS, J., STROHAECKER, T.R., & CLARKE, T. (2014). **Optimization of Friction Spot Welding Process Parameters for AA2198-T8 Sheets.** Materials and Manufacturing Processes, 29(8), 934–940. doi:10.1080/10426914.2013.811727

[42] DE CASTRO, C.C., PLAINE, A.H., DE ALCÂNTARA, N.G., DOS SANTOS, J.F. **Taguchi approach for the optimization of refill friction stir spot welding parameters for AA2198-T8 aluminum alloy.** International Journal of Advanced Manufacturing Technology, vol 99, 1927–1936 (2018). doi:10.1007/s00170-018-2609-2

[43] SHEN, Z., YANG, X., YANG, S., ZHANG, Z., YIN, Y. **Microstructure and Mechanical Properties of Friction Spot Welded 6061-T4 Aluminum Alloy.** Materials & Design, vol 54, 766–778 (2014). doi:10.1016/j.matdes.2013.08.021

[44] BADARINARAYAN, H., SHI, Y., LI, X., OKAMOTO, K. **Effect of Tool Geometry on Hook Formation and Static Strength of Friction Stir Spot Welded Aluminum 5754-O Sheets.** International Journal of Machine Tools Manufacturing, vol 49, 814–823 (2009). doi:10.1016/j.ijmachtools.2009.06.001

[45] EFFERTZ, P.S., INFANTE, V., QUINTINO, L., SUHUDDIN, U., HANKE, S., DOS SANTOS, J.F. **Fatigue Life Assessment of Friction Spot Welded 7050-T76 Aluminium Alloy Using Weibull Distribution.** International Journal of Fatigue, vol 87, 381–390 (2016). doi:10.1016/j.ijfatigue.2016.02.030

[46] REIMANN, M., GOEBEL, J., DOS SANTOS, J.F. **Microstructure Evolution and Mechanical Properties of Keyhole Repair Welds in AA 2219-T851 Using Refill Friction Stir Spot Welding.** Journal of Materials Engineering Perform, vol 27, 5220–5226 (2018). doi:10.1007/s11665-018-3519-z

[47] PEREIRA, A.M., FERREIRA, J.M., LOUREIRO, A., COSTA, J.D.M., BÁRTOLO, P.J.: **Effect of Process Parameters on the Strength of Resistance Spot Welds in 6082-T6 Aluminium Alloy.** Materials & Design, vol 31, 2454–2463 (2010). doi:10.1016/j.matdes.2009.11.052

[48] LAGE, S.B.M., CAMPANELLI, L.C., DE BRIBEAN GUERRA, A.P., SHEN, J., DOS SANTOS, J.F., DA SILVA, P.S.C.P., BOLFARINI, C. **A study of the parameters influencing mechanical properties and the fatigue performance of refill friction stir spot welded AlMgSc alloy.** International Journal of Advanced Manufacturing Technology. vol 100, 101–110 (2019). doi:10.1007/s00170-018-2696-0

[49] BARROS, P.A.F.D.E., CAMPANELLI, L.C., ALCÂNTARA, N.G., DOS SANTOS, J.F. **An investigation on Friction Spot Welding of AA2198-T8 Thin Sheets.** Fatigue & Fracture of Engineering Materials & Structures, 535–542 (2017). doi:10.1111/ffe.12512

[50] CAO, J.Y., WANG, M., KONG, L., GUO, L.J. **Hook Formation and Mechanical Properties of Friction Spot Welding in Alloy 6061-T6.** Journal of Materials Processing Technology, 230, 254–262 (2016). doi:10.1016/j.jmatprotec.2015.11.026

[51] XU, Z., LI, Z., JI, S., ZHANG, L.: **Refill Friction Stir Spot Welding of 5083-O Aluminum Alloy.** Journal of Materials Science and Technology, vol 34, 878–885 (2018). doi:10.1016/j.jmst.2017.02.011

[52] TIER, M.D., ROSENDO, T.S., DOS SANTOS, J.F., HUBER, N., MAZZAFERRO, J.A., MAZZAFERRO, C.P., & STROHAECKER, T.R. **The Influence of Refill FSSW Parameters on the Microstructure and shear Strength of 5042 Aluminium Welds.** Journal of Materials Processing Technology, 213(6), 997–1005. (2013). doi:10.1016/j.jmatprotec.2012.12.009

[53] American Welding Society. **AWS D17.2/D17.2M:2013 Specification for Resistance Welding for Aerospace Applications**, 2nd Edition (2013)

[54] UEMATSU, Y., TOKAJI, K.: **Comparison of Fatigue Behaviour Between Resistance Spot and Friction Stir Spot Welded Aluminium Alloy Sheets.** Science Technology Welding and Joining, vol 14, 62–71 (2008). doi:10.1179/136217108x338908

[55] YUAN, W., MISHRA, R.S., WEBB, S., CHEN, Y.L., CARLSON, B., HERLING, D.R., GRANT, G.J. **Effect of Tool Design and Process Parameters on Properties of Al Alloy 6016 Friction Stir Spot Welds.** Journal of Materials Processing Technology, 211, 972–977 (2011). doi:10.1016/j.jmatprotec.2010.12.014

[56] PLAINE, A.H., SUHUDDIN, U.F.H., ALCÂNTARA, N.G., DOS SANTOS, J.F. **Fatigue behavior of Friction Spot Welds in Lap Shear Specimens of AA5754 and Ti6Al4V Alloys.** International Journal of Fatigue. vol 91, 149–157 (2016). doi:10.1016/j.ijfatigue.2016.06.005

[57] BRZOSTEK, R.C., SUHUDDIN, U.F.H., SANTOS, J.F. Fatigue Assessment of Refill Friction Stir Spot Weld in AA2024-T3 Similar Joints, Fatigue and Fracture Engineering Materials and Structures 41, 1208–1223 (2018). doi:10.1111/ffe.12764.

[58] FU, M., MALLICK, P.K. **Fatigue of Self-Piercing Riveted Joints in Aluminum Alloy 6111.** International Journal of Fatigue. vol 25, 183–189 (2003). doi:10.1016/S0142-1123(02)00115-9

[59] HUANG, L., GUO, H., SHI, Y., HUANG, S., SU, X. **Fatigue Behavior and Modeling of Self-Piercing Riveted Joints in Aluminum Alloy 6111.** International Journal of Fatigue. vol 100, 274–284 (2017). doi:10.1016/j.ijfatigue.2017.03.006

[60] KRAUSE, A. R., CHERNENKOFF, R. A. **A Comparative Study of the Fatigue Behavior of Spot Welded and Mechanically Fastened Aluminum Joints.** SAE Technical Paper Series (1995). doi:10.4271/950710

[61] BOOTH, G. S., OLIVIER, C. A., WESTGATE, S. A., LIEBRECHT, F., & BRAUNLING, S. **Self-Piercing Riveted Joints and Resistance Spot Welded Joints in Steel and Aluminium.** SAE Technical Paper Series (2000). doi:10.4271/2000-01-2681

[62] ASM Metals Handbook - vol. 2: **Properties and Selection: Nonferrous Alloys and Special-Purpose Materials.** Technology. 2, 3470 (2001). doi:10.1016/S0026-0576(03)90166-8

[63] BOLDSAIKHAN, E., FUKADA, S., FUJIMOTO, M., KAMIMUKI, K., OKADA, H.: **Refill Friction Stir Spot Welding of Surface-treated Aerospace Aluminum Alloys with Faying-surface Sealant.** Journal of Manufacturing Process 42, 113-120 (2019). doi:10.1016/j.jmapro.2019.04.027

[64] ASTM American Society Testing Materials. **ASTM E112-13 Standard Test Methods for Determining Average Grain Size** (2013)

[65] SILVA, B.H., ZEPON, G., BOLFARINI, C., DOS SANTOS, J.F.: **Refill Friction Stir Spot Welding of AA6082-T6 Alloy: Hook Defect Formation and its Influence on the Mechanical Properties and Fracture Behavior.** Materials Science & Engineering A. (2019). doi:10.1016/j.msea.2019.138724

[66] RODRIGUES, D.M., LOUREIRO, A., LEITAO, C., LEAL, R.M., CHAPARRO, B.M., VILAÇA, P.: **Influence of friction stir welding parameters on the microstructural and mechanical properties of AA 6016-T4 thin welds.** Materials and Design. 30, 1913–1921 (2009). doi:10.1016/j.matdes.2008.09.016

[67] REIMANN, M., GARTNER, T., SUHUDDIN, U., GÖBEL, J., DOS SANTOS, J.F.: **Keyhole closure using friction spot welding in aluminum alloy 6061 – T6.** Journal of Materials Processing Technology. 237, 12–18 (2016). doi:10.1016/j.jmatprotec.2016.05.013

[68] DE CASTRO, C.C. 2019. **Refill Friction Stir Spot Welding: Evaluation of the Welding of AA2198-T8 Sheets and Preliminary Tool Wear Investigation.** Masters thesis. Federal University of São Carlos, São Carlos.

[69] PEROVIC, A., PEROVIC, D.D., WEATHERLY, G.C., LLOYD, D.J.: **Precipitation in Aluminum Alloys AA6111 And AA6016.** Scripta Materialia, Vol. 41, No. 7, pp. 703–708 (1999).

[70] SLÁMOVÁ, M., JANECEK, M., CIESLAR, M., SÍMA, V. **Effect of Quenching Temperature on Age Hardening of AA6016 Sheets.** Materials Science Forum Vols. 567-568 - 333-336 (2008).

[71] HONG, L., GANG, Z., CHUN-MING, L., LIANG, Z.: **Effects of Different Tempers on Precipitation Hardening of 6000 series Aluminium Alloys.** Transactions of Nonferrous Metals Society of China 17, 122-127 (2007).

[72] LAM, P.V.T. 2016. **Intergranular Corrosion of Extruded AlMgSi (Cu, Zn) Alloys.** Master thesis. Department of Materials Science and Engineering - Norwegian University of Science and Technology, Trondheim.

[73] CHUA, Q., LIA, W.Y., YANGA, X.W., SHENB, J.J., VAIRISA, A., FENGA, W.Y., WANG W.B. **Microstructure and Mechanical Optimization of Probeless Friction Stir Spot Welded Joint of an Al-Li alloy.** Journal of Materials Science & Technology 34 1739–1746 (2018). https://doi.org/10.1016/j.jmst.2018.03.009

[74] BIROL, Y. **Pre-aging to Improve Bake Hardening in a Twin-roll Cast Al–Mg–Si Alloy.** Materials Science and Engineering A 391, 175–180 (2005). doi:10.1016/j.msea.2004.08.069

[75] SCHIFFMANN, R., HAUG, J., BANHART, J. **Evolution of Precipitates during Age-hardening of AW 6016 Alloy.** Proceedings of the 9th International Conference on Aluminium Alloys. Institute of Materials Engineering Australasia Ltd. 604-609 (2004).

APPENDIX A

Table A – Shear strength

Sample	RS (rpm)	PD (mm)	Force (kN)		Welding time (s)	LSS (kN)	Fracture
			Plunge	Retract			
126	1800	1.6	10	8	2.844	3.73	PO
127	1800	1.6	10	8	2.842	3.92	PO
128	2100	1.6	10	7	2.854	1.62	PO
129	1800	1.8	10	7	2.926	1.58	PO
130	2100	1.6	10	9	3.55	2.92	PO
131	1500	1.6	10	7	2.846	2.93	PO
132	1500	1.8	10	8	2.904	3.71	PO
134	1800	1.4	10	9	3.49	3.91	PO
135	2100	1.8	10	8	2.912	3.52	PO
136	1800	1.4	10	7	2.72	2.9	PO
137	1800	1.8	10	9	3.552	3.23	PO
138	1500	1.6	10	9	3.55	3.89	PO
139	1800	1.6	10	8	2.834	4.25	PO
140	1500	1.4	10	8	2.736	3.41	PO
141	2100	1.4	10	8	2.702	4.02	PO

Table B – Shear strength

Sample	RS (rpm)	PD (mm)	Force (kN)		Welding time (s)	LSS (kN)	Fracture
			Plunge	Retract			
126	1800	1.6	10	8	2.844	3.73	PO
127	1800	1.6	10	8	2.842	3.92	PO
128	2100	1.6	10	7	2.854	1.62	PO
129	1800	1.8	10	7	2.926	1.58	PO
130	2100	1.6	10	9	3.55	2.92	PO
131	1500	1.6	10	7	2.846	2.93	PO
132	1500	1.8	10	8	2.904	3.71	PO
134	1800	1.4	10	9	3.49	3.91	PO
135	2100	1.8	10	8	2.912	3.52	PO
136	1800	1.4	10	7	2.72	2.9	PO
137	1800	1.8	10	9	3.552	3.23	PO
138	1500	1.6	10	9	3.55	3.89	PO
139	1800	1.6	10	8	2.834	4.25	PO
140	1500	1.4	10	8	2.736	3.41	PO
141	2100	1.4	10	8	2.702	4.02	PO
142	1800	1.4	10	8.25	2.712	4.32	PO

(continue)

143	1800	1.2	10	8.25	2.574	4.16	PO
144	1500	1.6	10	9	3.05	3.93	PO
145	1800	1.4	10	9	2.71	3.76	PO
146	1800	1.4	10	9	2.716	4.21	PO
147	1800	1.4	10	8.5	2.71	4.29	PO
148	1800	1.4	10	8.25	2.7	4.16	PO
149	1800	1.4	10	8	2.708	4.16	PO
150	1800	1.4	10	7	2.786	1.45	PO
153	1800	1.2	10	7	2.746	1.58	PO
154	1500	1.2	10	8	2.568	4.06	PO
155	2100	1.2	10	8	2.57	4.02	PO
156	1800	1.2	10	9	2.576	4.31	PO
157	1800	1.4	10	8.25	2.706	4.22	PO
158	1800	1.4	10	7	2.752	1.66	PO
159	1800	1.4	10	7	2.714	1.73	PO
160	1800	1.4	10	8.5	2.714	4.01	PO
161	1800	1.4	10	8.5	2.7	4.14	PO
162	1800	1.4	10	8	2.704	3.98	PO
163	1800	1.4	10	8	2.706	3.88	PO
226	1000	1.6	10	9	2.802	4.78	PO
227	1000	1.4	10	8	2.726	3.39	PO
229	1000	1.8	10	8	2.804	4.63	PO
230	1500	1.4	10	8.5	2.726	4.74	PO
355	1000	1.6	10	9	2.996	4.89	PO
356	1000	1.6	10	9	3.092	4.85	PO
357	1000	1.6	10	10	3.112	4.65	PO
358	1000	1.6	10	10	3.226	4.66	PO
359	1000	1.6	10	10	3.284	4.63	PO
518	1000	1.6	10	8	3.36	4.33	PO
519	1000	1.6	10	8	2.84	4.02	PO
520	1000	1.6	10	8	3.424	3.99	PO
521	750	1.6	10	9	3.346	4.73	PO
522	750	1.6	10	9	3.312	4.74	PO
523	750	1.6	10	9	3.37	4.77	PO
533	1000	1.4	10	9	3.194	4.46	PO
534	1000	1.4	10	9	2.746	4.78	PO
535	1000	1.4	10	9	2.75	4.8	PO